

Annexes

Annexe A

***Article « New results on the helium stars
in the galactic center using BEAR
spectro-imagery »***

New results on the helium stars in the galactic center using BEAR spectro-imagery

T. Paumard¹, J. P. Maillard^{1,*}, M. Morris², and F. Rigaut^{3,*}

¹ Institut d'Astrophysique de Paris (CNRS), 98b Bd. Arago, 75014 Paris, France

² University of California, Los Angeles, Div. of Astronomy, Dept. of Physics and Astronomy, Los Angeles, CA 90095-1562, USA

³ Gemini North Headquarter, Hilo, HI 96720, USA

Received 22 June 2000 / Accepted 17 October 2000

Abstract. Integral field spectroscopy of the central parsec of the Galactic Center was obtained at 2.06 μm using BEAR, an imaging Fourier Transform Spectrometer, at a spectral resolution of 74 km s^{-1} . Sixteen stars were confirmed as “helium stars” by detecting the He I 2.058 μm line in emission, providing a homogeneous set of fully resolved line profiles. These observations allow us to discard some of the earlier detections of such stars in the central cluster and to add three new stars. The sources detected in the BEAR data were compared with adaptive optics images in the K band to determine whether the emission was due to single stars. Two sub-classes of almost equal number are clearly identified from the width of their line profiles, and from the brightness of their continuum. The first class is characterized by very broad line profiles ($FWHM \simeq 1000 \text{ km s}^{-1}$) and by their relative faintness. The other, brighter in K by an average factor of ~ 9 , has a much narrower emission component of width $\simeq 200 \text{ km s}^{-1}$. Most of the emission lines show a P Cygni profile. From these results, we propose that the latter group is formed of stars in or near the LBV phase, and the other one of stars at the WR stage. The division into two groups is also shown by their spatial distribution, with the narrow-line stars in a compact central cluster (IRS 16) and the other group distributed at the periphery of the central cluster of hot stars. In the same data cube, streamers of interstellar helium gas are also detected. The helium emission traces the densest parts of the SgrA West Mini-Spiral. Several helium stars have a radial velocity comparable to the velocity of the interstellar gas in which they are embedded. In the final discussion, all these findings are examined to present a possible scenario for the formation of very massive stars in the exceptional conditions of the vicinity of the central Black Hole.

Key words. instrumentation: spectrograph – techniques: radial velocities – infrared: stars – galaxy: center – stars: early-type – stars: wolf-rayet

1. Introduction

The very inner region of the Galactic Center (GC) is the focus of many studies as it offers the unique opportunity to study star formation and the extreme gas kinematics peculiar to the vicinity of a $2.5 \cdot 10^6 M_{\odot}$ black hole (Genzel et al. 1997; Ghez et al. 1998). The presence of an unusually broad 2.058 μm neutral helium line in emission was among the early known peculiarities of the central infrared source, originally called IRS 16 (Hall et al. 1982). Continuously improved spatial resolution has made it possible to tie this emission to individual stars and to suggest that this

emission is explained by the presence of massive, young, hot stars (Najarro et al. 1997a). However, even if the formation of high mass stars was favored in the GC (Morris 1993), the prediction of evolving starbursts cannot fully explain the large abundance of massive, emission-line stars which are normally very rare and short-lived (Lutz 1998). Therefore, more spectroscopic observations are warranted to better understand the unique conditions in the central parsec of the Milky Way which can lead to the formation of numerous helium emission-line stars. An exact census and a precise determination of the physical properties of these stars is also important since they should significantly contribute to the ionization of the central parsec.

In this paper, we present new data obtained with an original type of integral field spectrometer, an imaging Fourier Transform Spectrometer called BEAR, on the 3.6-m Canada-France-Hawaii Telescope. The use of this instrument represents an effort to make a significant step

Send offprint requests to: J. P. Maillard,
 e-mail: maillard@iap.fr

* Visiting Astronomer, Canada-France-Hawaii Telescope, operated by the National Research Council of Canada, le Centre National de la Recherche Scientifique de France and the University of Hawaii, USA.

in associating the best possible spatial resolution and a high spectral resolution in the near infrared. The spatial resolution is not limited by a slit width, as with a standard grating spectrometer. It corresponds to the common seeing conditions at the CFH Telescope on Mauna Kea at $2 \mu\text{m}$ ($\simeq 0.6''$). The spectral resolution is provided by the FTS. To complete the star detection, an adaptive optics (AO) image of the same field in the K band was utilized. The processing of the BEAR data cube is described in Sect. 3. All the new results obtained from this study are presented in Sect. 4, including the display of the He I $2.058 \mu\text{m}$ line profiles of all the detected stars and, for the first time, the mapping of flows of interstellar helium. A detailed review of the detected stars follows in Sect. 5. Finally, a discussion of the nature of the He I stars, of the link between these stars and the helium flows, and of a possible star formation scenario are presented in Sect. 6.

2. Observations

The 3-D data were obtained in July 25, 1997 during a run with the BEAR Imaging FTS at the $f/35$ infrared focus of the 3.6-m CFH Telescope. For a detailed description of the properties of this type of instrument, we refer the reader to Simons et al. (1994), Maillard (1995), and to an updated review in Maillard (2000). Briefly, the BEAR instrument results from the coupling of the CFHT step-scan high resolution facility FTS (Maillard & Michel 1982) with a 256×256 HgCdTe facility camera. The field of view is circular with a $24''$ diameter, which corresponds to 0.93 pc at an assumed distance of 8 kpc for the GC (Reid 1993). The plate scale on the detector is $0.35''/\text{pixel}$. The raw data consist of a cube of 300 planes with an integration time of 10 s per image, an image being taken at each stepping of the interferometer. In the camera, a narrow-band filter (bandpass $4806\text{--}4906 \text{ cm}^{-1}$) isolates the He I $2.058 \mu\text{m}$ line. Observation of the GC from Mauna Kea is not possible at low airmass (at 42° above horizon at its highest). Therefore, the scan was acquired with an airmass less than 1.8 to preserve the image quality. The maximum path difference which was reached corresponds to a limit of resolution ($FWHM$) of 1.2 cm^{-1} , i.e., 74 km s^{-1} . Much higher spectral resolution can be obtained in this mode with the instrument (Maillard 2000). This value represents a compromise between the resolution needed to resolve the narrowest features of the line profiles and the detection depth. In any case, this resolution is at least 4 times better than in most of the previous spectral observations (Allen et al. 1990; Geballe et al. 1991; Krabbe et al. 1991; Krabbe et al. 1995; Blum et al. 1995b; Libonate et al. 1995; Tamblyn et al. 1996; Genzel et al. 1996; Najjarro et al. 1997a, to quote the most important contributions to this study). A data cube on an A0 calibration star (HD 18881, $m_K = 7.14$ from Elias et al. 1982) was obtained on the same night, at exactly the same spectral resolution. This procedure was important for the precise correction of telluric absorptions since the $2.058 \mu\text{m}$ line is in the middle of a strong CO_2 band.

High spatial resolution images of the inner region of the GC in the K band were obtained with the CFHT Adaptive Optics Bonnette (Lai et al. 1997) equipped with the 1024×1024 HgCdTe KIR camera (Doyon et al. 1998) on 1998, 26 June. The total integration time is equal to 480 s from the acquisition of 4 times 10 exposures of 12 s each to cover a total field of $\simeq 40'' \times 40''$, just a little bigger than the direct field of the camera ($35'' \times 35''$). The reference star for guiding was a $m_K = 14.5$ star located $24''$ from SgrA*. The data processing included the filtering of star halos and the assemblage of the individual images to build the total field, which contains the entire BEAR field. The $FWHM$ of the point-spread function (psf) in the final image varies from $0.13''$ to $0.20''$, depending on the distance to the guiding star. A slight elongation can be seen on the most distant images. Nonetheless, the image quality is roughly 4 times better than the seeing-limited BEAR images.

3. Processing of BEAR data

The processing of the BEAR data included two major operations. The first part is the standard processing for any BEAR data cube, from the raw data which are interferograms to the spectral cube. A second part has had to be developed specifically to cancel the atmospheric OH emission, extract the stars from a very crowded field, and to separate, in the spectra, the stellar contribution from the background emission. All these steps are briefly described below.

3.1. Cube reduction

The cube reduction, made with a package called *bearprocess* (Maillard 2000), consists of the usual operations of flat-fielding of the images of the raw cube, sky subtraction, correction for bad pixels, and registration of each frame relative to the first one to correct for turbulent motions and flexure drifts. All the interferograms are extracted from this corrected cube, and the corresponding spectra are computed by FFT, leading in this case to a 384-plane cube, this number being determined as the sum of powers of two, just larger than the initial 300 planes. The same operations have been made on the reference star data cube to yield in the end a single spectrum. From the division of the GC spectral cube by this reference spectrum, a new cube was produced, corrected for the instrumental and atmospheric transmission. In order to fully reconstruct the line profiles, and to apply the instrumental phase correction through the field, an oversampled cube of 1153 frames was computed which contains only the useful part of the spectrum after division, between 4827.19 cm^{-1} ($2.0716 \mu\text{m}$) and 4889.74 cm^{-1} ($2.0451 \mu\text{m}$). In this cube, the separation between frames corresponds to a mean velocity resolution of 3.35 km s^{-1} , i.e., an oversampling by a factor of 12 from the initial cube.

3.2. OH correction

The CFHT-FTS is based on a design with dual input, dual output (Maillard & Michel 1982). For observations of isolated objects the source is centered in one entrance aperture, while the other one is open on the sky $53''$ West. This makes an automatic correction of the sky emission possible, in particular for OH. In the case of an extended field such as the GC, a single aperture must be open. Therefore, the OH emission strongly contaminates the raw data cube. The problem is particularly serious since a strong OH line falls at $2.0563 \mu\text{m}$, within a typical linewidth of the stellar He I line. This OH line is not resolved and thus appears as an extended sinc function, the natural instrumental line-shape of an FTS. In the useful part of the spectrum, a second OH line, four times fainter, at $2.0499 \mu\text{m}$, falls in the continuum. In addition, the OH line intensities do not appear to be perfectly uniform over the entire field.

We applied a method intended to allow the best removal of these lines, secondary maxima included. First, the spectrum of the atmospheric emission (S_{sky}) to be used as template was extracted by averaging the emission over about 100 pixels from small areas of the field devoid of sources. Then, for each pixel spectrum S of the data cube, the following expression was generated, integrated in the wavenumber σ over the full spectral range:

$$E(\mu) = \int \left(\frac{d^2 (S - \mu S_{\text{sky}})}{d\sigma^2} \right)^2 d\sigma.$$

The final corrected spectrum is $S - \mu_m S_{\text{sky}}$ where μ_m corresponds to the value of μ for which $E(\mu)$ is minimum. A new cube cleaned of OH emission was created according to this procedure, to which all the subsequent operations were applied.

3.3. Extraction of stellar spectra

An image of the field of view was generated by co-adding most of the frames of this cube, with the exception of about 100 frames at each extremity, where division by the reference spectrum creates excessive noise. An automatic 2-D local maximum search was run on this image in order to detect the stars. With this procedure a total of 90 individual stars was identified within the circular field of the instrument. By using the photometry of Ott et al. (1999) for the faintest stars which are in common we determined a limiting magnitude of $m_K \simeq 13$ for the stellar flux integrated in a 3×3 pixels aperture (or $\simeq 1'' \times 1''$). For almost the same field as us (a square field of $20'' \times 20''$ centered on SgrA*) 218 stars brighter than $m_K = 13$ are reported by Ott et al. (1999) from deconvolved images integrated over a $0.25''$ diameter aperture. Obviously, the main limitation comes from the seeing-limited imagery with BEAR in a very crowded field.

A facility program called *cubeview* (Maillard 2000), specially developed to inspect any BEAR data cube, was used to extract the 90 stellar spectra from the cube, by integration over a 3×3 pixels aperture, centered on

the brightest pixel of each detected star image. The final spectra resulted from a smoothing operation (boxcar function) to improve the S/N ratio. This operation was justified since the spectral resolution was much narrower than the broad stellar line profiles (74 km s^{-1} against $\sim 1000 \text{ km s}^{-1}$). To search all spectra for the presence of the He I $2.058 \mu\text{m}$ line in emission, a 3σ -detection criterion was applied to each smoothed spectrum, with the noise estimated in the continuum. From the same cube a “line cube” was generated. This was done by estimating a linear continuum in each spectrum, extracted pixel-by-pixel over the entire field, and by subtracting it from the original spectrum. Thus, the helium emission was all that remained. Using *cubeview* to inspect the cube images within the helium emission range revealed the stars being source of a He I emission as bright spots. Note that with spectro-imaging data the equivalent of an ideal square filter can be applied, isolating only the emission component without continuum, thus giving the maximum contrast to these stars, more accurately than could be done by imaging through a narrow-band filter. A few other stars with helium emission, for which the automatic detection had failed, were found by this method. Finally, the spectra of all the stars with helium emission were extracted from both cubes, in order to obtain two spectra for each star: the total spectrum, and the spectrum of the emission line only.

3.4. Separation of stars and gas

A co-added image was created with *cubeview* from all the frames of the line cube containing some He I emission. The resulting image clearly shows that the emission is concentrated in bright points, likely stars, but also in diffuse zones, indicative of interstellar gas lanes. Therefore, a separation of stars and gas must be conducted to obtain pure stellar line profiles and a spectral cube of the interstellar medium (ISM) emission only.

The He I line profiles detected with *cubeview* from the line cube in the gas patches exhibit a width just equal to the spectral resolution, which contrasts with the much broader profiles on most stellar points. The increase in spectral resolution provided by the BEAR spectrometer appears essential for distinguishing the ISM emission from the stellar emission. In many of the stellar profiles a narrow component is seen to be superimposed on a broad component. In these cases an inspection of the data in the vicinity of the star confirms the presence of extended ISM emission along the line of sight. Hence, the stellar profile can be cleaned of the ISM emission contribution by a local interpolation on the profile. In other cases, a line with width equal to the spectral resolution appears on top of a stellar continuum. This typical linewidth avoids confusion with an emission of stellar origin. However, in a few cases the emission line on top of a stellar continuum appears relatively narrow, about twice as wide as a typical ISM line. Only the absence of ISM emission in the

neighborhood of such a star gives confidence in the stellar nature of the emission. The ISM emission can also mimic a stellar profile. Indeed, inspection of the cube indicates that, in some locations, the ISM emission shows several velocity components, which can merge into a broader line. In these cases a global inspection of the images confirms that the profile is due to ISM emission only. Finally, after all this careful selection, a fit to the stellar emission at all the confirmed He I star positions in the line cube was subtracted from the spectra, generating a spectral cube of the ISM emission.

3.5. Fitting of the 2.058 μm emission line profiles

In the end, 16 stars from the 90 stars isolated in the ~ 1 -pc field centered on SgrA* exhibit the 2.058 μm He I line in emission, which can be attributed only to the underlying star. A homogeneous set of fully resolved line profiles is obtained. This signature justifies them being called “helium stars”. Actually, this designation is not a true stellar classification. They are simply stars showing the 2.058 μm helium line in emission. In the following the term “helium star” or “He I star” will therefore be adopted in this context. From the stellar positions, the correlation with previously identified stars was made from photometric surveys, e.g., Blum et al. (1996a), Eckart & Genzel (1997), and Ott et al. (1999). Three new helium stars not present in prior lists were first noted: He I N1, He I N2 and He I N3. One of them, He I N1, coincides with ID 180, a source already identified in the photometric survey of Ott et al. (1999). This identification was adopted.

In order to derive the radial velocities of all these stars, simple analytical models were used which take into account the P Cygni profile evident in most profiles. The 2.058 μm He I line has the advantage of not being blended with the emission lines of other atomic species which are likely to be present in the spectrum of these stars (Najarro et al. 1997a). Depending on the profile shape, we used three types of fitting models (a, b, c). In each case, the model yields the *FWHM* of the emission component, and the velocity domain of the full profile, *FWZI* (full width at zero intensity). The center of *FWZI* defines the radial velocity (V_R) of the star. *FWZI* is also indicative of the terminal outflow velocity of the expanding envelope.

- a) For the few profiles with no detectable absorption component, a fitting by a Gaussian profile was used. In this case the *FWZI* is in fact estimated at one hundredth of the maximum intensity above the baseline;
- b) For the P Cygni profiles for which the absorption component has a width comparable to that of the emission component, a two-Gaussian fitting was applied. *FWZI* is limited with the same criterion as above on the emission side, and at one hundredth of the central depth below the baseline on the absorption side;
- c) For the stars with a P Cygni profile but showing a very broad emission component, a two-component fitting was used with a profile described in Morris (1985)

for the emission component, and a Gaussian profile for the absorption component. For the determination of *FWZI*, the boundary of the profile on the red side is given by the emission fit. The Gaussian profile is limited as above on the absorption side.

3.6. Calibration of line profiles

For flux calibration, the stellar spectra must be extracted from the cube which includes the continuum. However, the intensity in these spectra is contaminated by the nearby stars present in the 3×3 pixel BEAR box centered on each helium star. Corrections of this contamination were applied with the help of the AO image. In order to do this, the star positions and the peak intensities in the AO image were all determined with an automatic procedure. Then, at each star position, the BEAR psf was placed, which is a Lorentzian profile obtained from the calibration star data cube with the corresponding intensity. The result is an image at the BEAR spatial resolution. This reconstructed image was superimposed upon the image obtained by co-adding the frames of the BEAR cube with only the stellar continuum, by looking for the best match of the star patterns between the two images. By this process we determined the appropriate offsets and rotation between the two images. With these registration parameters, the BEAR box for each He I star, centered on the bright pixel determined from the line cube was projected on the corresponding area of the original AO image. From this superposition, in the case of multiple images, the most likely identification of the helium star can be asserted, and then the contamination by the neighboring stars within the square aperture estimated. The absolute star positions could be measured at the precision of the pixel size in the AO image (0.035" pixel). They were determined first as offsets with respect to IRS 16NE, because this star from the AO image is a relatively isolated, bright star. Its position was taken from Ott et al. (1999), but in that paper, all the positions are given as offsets relative to the brightest local source, IRS 7, which is unusable in the AO image because its image is saturated. In order to present the final offsets of all the sources with respect to SgrA*, the position of IRS 7 relative to SgrA* was taken from Menten et al. (1997) and used to derive the IRS 16NE position relative to SgrA*.

4. Presentation of results

4.1. Two classes of He I stars

By inspecting the shapes of the full set of He I line profiles, two classes of stars can be clearly distinguished. Indeed, 7 stars show a narrow emission line with a mean *FWHM* of $225 \pm 75 \text{ km s}^{-1}$, and 9 stars a very broad emission line with a mean *FWHM* of 1025 km s^{-1} , all the values being within $\pm 400 \text{ km s}^{-1}$ of this average. The *FWZI* associated with the latter group varies from $\sim 1700 \text{ km s}^{-1}$ to $\sim 3000 \text{ km s}^{-1}$. The stars of each group are gathered

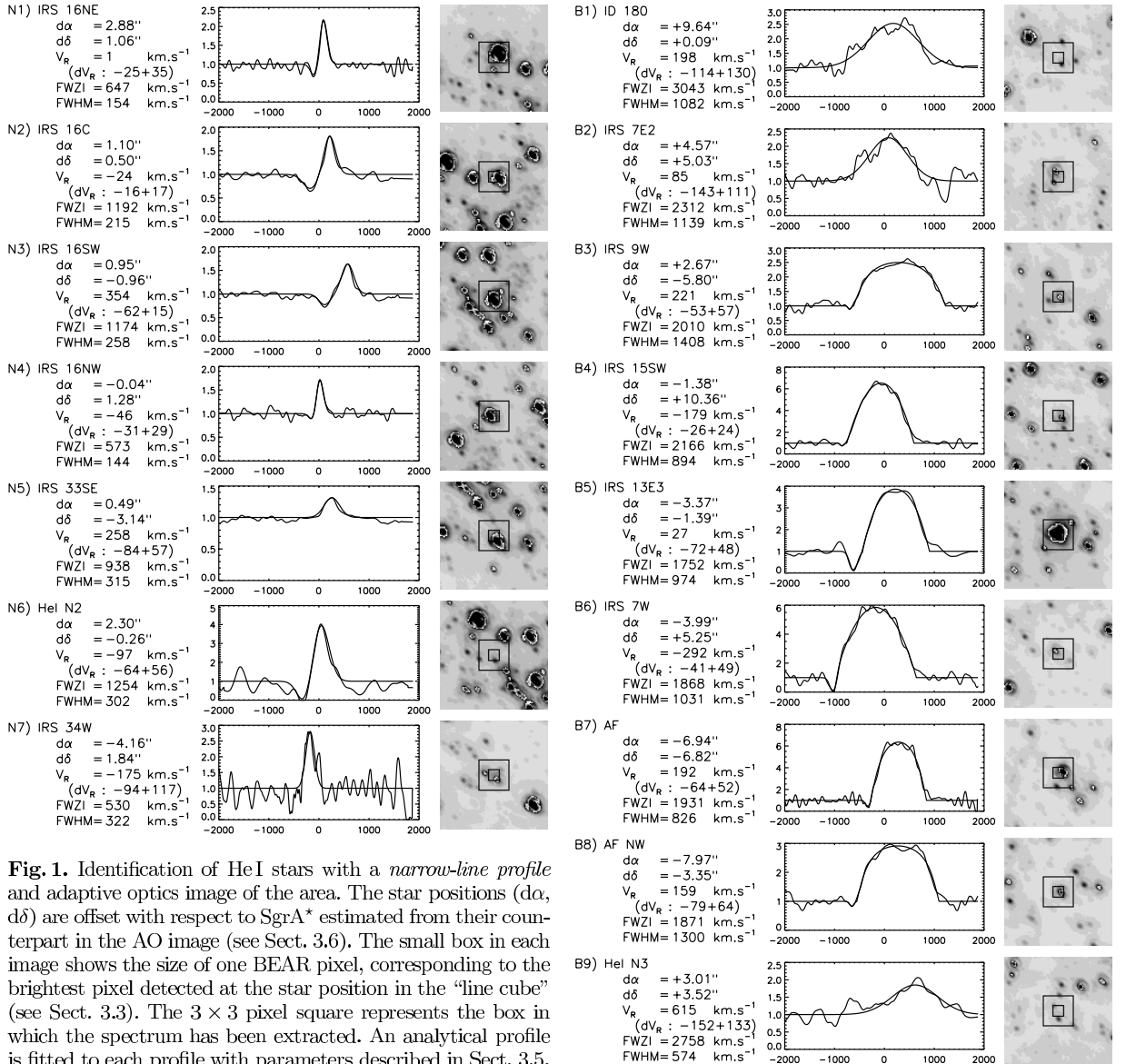


Fig. 1. Identification of He I stars with a *narrow-line profile* and adaptive optics image of the area. The star positions ($d\alpha$, $d\delta$) are offset with respect to SgrA* estimated from their counterpart in the AO image (see Sect. 3.6). The small box in each image shows the size of one BEAR pixel, corresponding to the brightest pixel detected at the star position in the “line cube” (see Sect. 3.3). The 3×3 pixel square represents the box in which the spectrum has been extracted. An analytical profile is fitted to each profile with parameters described in Sect. 3.5, given in the left column. V_r is the radial velocity with dV_r the $1\text{-}\sigma$ error bar (see Sect. 4.3). The vertical scale in each spectrum is given in multiples of the intensity of the neighboring continuum, for which the calibrated value is given in Table 1

Fig. 2. Identification of He I stars with a *broad-line profile* and adaptive optics image of the area. The projected boxes have the same meaning as in Fig. 1

in Figs. 1 and 2 respectively, with the parameters of the fitting of the line profiles, the star names, and the star positions as offsets from SgrA*. These positions are given in arcsecs at the precision of the position of their counterpart measured in the AO image (Sect. 3.6).

Note that most of these profiles are of the common P Cygni variety, with the standard absorption on the blue side. This absorption is generally shallow for the very broad emission lines, since the emission almost fills the absorption width, and is deeper for the narrow emission lines. For the broad-line profiles (Fig. 2) a flat top is seen

for AF, which was already known (Najarro et al. 1994), but also for AF NW, IRS 7W, IRS 13E and presumably ID 180. All these various types of profile are encountered in models of P Cygni profiles (Castor & Lamers 1979).

Table 1 presents the continuum flux level for each star measured at $2.06 \mu\text{m}$, at wavelengths just outside of the emission profile, estimated by the procedure described in Sect. 3.6. No extinction correction has been applied. As these stars are located at the same distance, a comparison of flux is possible without correction. From an examination of Table 1, it appears that with this distinction of

Table 1. Continuum Φ of the He I stars at $2.06 \mu\text{m}$

Narrow-line stars ^a			Broad-line stars ^b		
ID	Name	Φ^c	ID	Name	Φ^c
N1	IRS 16NE	25.93	B1	ID 180	0.59
N2	IRS 16C	13.23	B2	IRS 7E2	0.77
N3	IRS 16SW	10.87	B3	IRS 9W	1.55
N4	IRS 16NW	9.41	B4	IRS 15SW	1.02
N5	IRS 33SE	8.52	B5	IRS 13E3	2.26
			B6	IRS 7W	0.98
N6	HeI N2	(0.76)	B7	AF	3.88
N7	IRS 34W	(1.76)	B8	AF NW	1.84
			B9	HeI N3	0.58
mean*		13.59	mean		1.50

^a See Fig. 1.^b See Fig. 2.^c $10^{-14} \text{ W m}^{-2} \mu\text{m}^{-1}$.

* Mean intensity estimated without N6 and N7 (see text).

two families of line profile is associated another clear difference which had not been noticed before, namely the level of continuum. The continuum of the stars having a narrow profile is bright and with a comparable intensity, except for IRS 34W and HeI N2, which have a definitely weaker continuum. The continuum of the broad-line stars is fainter by a factor 9.0 on average ($\simeq 2.4 \text{ mag}$) than that of the narrow-profile stars. The AF star and IRS 13E3 appear to be the brightest objects of this group, though their continuum intensity is weaker by more than a factor 3 than the mean value of the narrow-line category. We return to these particular cases below.

The K -band AO image gives the opportunity of estimating the K magnitude, without extinction correction, of the He I stars. The photometric calibration was made by looking in the Ott et al. (1999) survey for a bright star common to our list, which is sufficiently isolated, and for which the photometry indicates a low index of variability. IRS 16NE was chosen as reference star, from which the K magnitude of all the other stars was deduced. With the same presentation as Table 1, the results are reported in Table 2. The mean difference of K magnitude between the two classes is equal to 2.18. That corresponds to a ratio of 7.45 against 9.0 measured near $2 \mu\text{m}$. This difference is due to the fact that, in the flux reported in Table 1, the correction of the contribution of neighboring stars (Sect. 3.6) can be made only by assuming the same spectral distribution in the K band for these stars and the He I star, which is an approximation. For example, IRS 13E3, which was the second brightest star among its group from Table 1, is not so prominent in K . Only AF remains 1 mag above the average value. However, the general trend observed at $2 \mu\text{m}$ is largely confirmed. Note that IRS 16SW is found 0.2 magnitude brighter than the mean value reported by Ott et al. (1999), which is well within the range of

Table 2. K magnitude of the He I stars

Narrow-line stars			Broad-line stars		
ID	Name	m_K	ID	Name	m_K
N1	IRS 16NE	8.76 ^a	B1	ID 180	12.12
N2	IRS 16C	9.41	B2	IRS 7E2	11.93
N3	IRS 16SW	9.38	B3	IRS 9W	11.62
N4	IRS 16NW	9.80	B4	IRS 15SW	11.21
N5	IRS 33SE	9.75	B5	IRS 13E3	11.73
			B6	IRS 7W	11.85
N6	HeI N2	(12.47)	B7	AF	10.56
N7	IRS 34W	(11.56)	B8	AF NW	11.52
			B9	HeI N3	12.47
mean*		9.35	mean		11.53

^a From Ott et al. (1999).

* Mean magnitude estimated without N6 and N7 (see text).

periodic variation reported for this star. The source ID 180 is found to be $\sim 0.6 \text{ mag}$ brighter than in Ott et al. (1999), while AF has exactly the same magnitude.

4.2. Comparison with previous lists of He I stars

The recent papers dedicated to surveying the helium stars in the central region of the GC are those of Krabbe et al. (1995), Tambllyn et al. (1996), Blum et al. (1996a) and Eckart & Genzel (1997). Blum et al. (1996a) present the most complete compilation of identified stars with their spectral type, reflecting both their own work and that of others. In this list, for the first time, the helium stars are identified under two denominations: HeI and WC9. The latter is a sub-type of Wolf-Rayet stars (WR) which in addition to the HeI $2.058 \mu\text{m}$ line in emission have the C III and the C IV lines in their K -band spectrum. A comparison of the list of stars that we identify as genuine HeI stars with the list of Blum et al. (1996a) shows that several of their stars are missing. A few candidates were just at the edge of our field and cannot be confirmed. But it turns out that, in the other cases, the detected emission line can be interpreted as due to the ISM emission and not to the star, or to the background contamination from a nearby HeI star. Following primarily the list of helium stars reported in Blum et al. (1996a), either as HeI or as WC9 stars, then in Eckart & Genzel (1997), and at last in Tambllyn et al. (1996), all the stars absent from our list are worth a special comment:

- **IRS 1W:** We confirm that IRS 1W, which is in the list of Krabbe et al. (1995) but not in Blum et al. (1996a), where it is given as a red star, is indeed not a HeI star. Blum et al. (1995b) had already shown a spectrum of IRS 1W with no intrinsic HeI $2.058 \mu\text{m}$ emission line and Libonate et al. (1995) had also cast doubt on the notion that IRS 1W was a compact HeI emission-line star. That is a case where the line present in the raw spectrum at the star position is very narrow. The study of the vicinity clearly shows that this emission belongs to an ISM gas lane. From the slope of the

- continuum spectrum, polarization measurements, and a broadened image profile at high spatial resolution, Ott et al. (1999) suggest that IRS 1W is embedded in a hot dust shell. However, a maximum of the ISM emission coincides with its position;
- **BSD WC9**: Blum et al. (1995a) have presented the K -band spectrum of this source as an example of a genuine WC9-type star. The same source is named Blum-WC9 by Tamblyn et al. (1996). A nearby source ($0.6''$ W and $0.4''$ S) is listed as BSD WC9B, which is supposed to be of same type. These two sources fall at the edge of our field, and therefore cannot be considered in our list;
 - **IRS 6E**: This source is also reported as a WC9 star. There is a rather broad ($\simeq 270 \text{ km s}^{-1}$) emission feature but with two maxima in the spectrum toward IRS 6E. The helium streamers are complex in its vicinity. The star lies just between the Bar and the mini-cavity. We interpret these two peaks as two velocity components of the ISM emission;
 - **IRS 29N**: We do not confirm a helium star at the IRS 29N position, which is listed as a WC9 star by Blum et al. and in Eckart & Genzel (1997). Separated by $0.5''$, IRS 29S is identified as an MIII star by Krabbe et al. (1995). There is no ISM helium emission there. This source is located in the neighborhood of the bright helium stars in the IRS 16 cluster, so the reported detection can probably be explained as contamination in the Krabbe et al. data by the nearby helium stars;
 - **MPE-1.0-3.5**: This source is listed as a WC9 star. In Ott et al. (1999) a star (ID 77, $m_K = 11.6$) coincides within $0.2''$, so it is probably the same source. In our data this star does not show any He I $2.058 \mu\text{m}$ emission feature. Since it is close to the bright source IRS 16NW, it was reported as a helium star probably for the same reason as the previous source;
 - **IRS 15NE**: This star falls at the edge of the field and cannot be included in our list;
 - **MPE+1.6-6.8**: A local maximum of the ISM emission is seen at the star position, but no stellar emission, which would reveal itself by a much larger width. This relatively bright star in K (10.56 from Ott et al. 1999) might be another embedded star like IRS 1W;
 - **IRS 16CC**: No He I stellar profile is found exactly at the position of this star;
 - **OSU He1**: The helium line observed on the line of sight to this star is narrow and comes from the He I Mini-Spiral;
 - **IRS 16SE**: This source appears in a star list restricted to the very inner region studied by Eckart & Genzel (1997), who mention 3 He I stars, IRS 16SE1, IRS 16SE2 and a nameless source located $0.91''$ East and $1.99''$ North of SgrA*. All these sources lie in the proximity of strong He I stars and in the Mini-Spiral. We do not confirm them as He I stars.

Tamblyn et al. (1996) used an attractive method to find He I star candidates by associating an image taken

through a narrow-band filter centered on the $2.058 \mu\text{m}$ line. However, their contrast was not sufficient to detect the ISM emission and they wrongly claimed that “the majority of the He I emission is from point sources”. In their list, they report 5 supposed new identifications they named GCHe1 to GCHe5. By inspecting the 5 positions we find that GCHe2 (or TAM HeI in Blum et al. 1996a) is in fact IRS 9W, which is confirmed as a He I star, GCHe3 is IRS 33SE and GCHe4 likely AF NW. Regarding GCHe1, Tamblyn et al. (1996) indicate a position not more precisely than $1.1''$ NE of AF. This region is at the very edge of our field. The current data do not allow us to confirm the presence of a helium star there. GCHe5 is identical in position to MPE-1.0-3.5, which has been rejected.

In conclusion, 6 out of 20 early-type stars listed in Blum et al. (1996a) as helium stars (noted He I or WC9) are not reported in our list. Three stars were excluded from our compilation, because they lie at the edge of the clear field: BSD WC9, BSD WC9B and IRS 15NE. Thus, 11 stars are in common. Of the 21 helium stars of Krabbe et al. (1995) we retain 13 sources. With 3 new stars which are added, the total number of helium stars in the central cluster remains roughly unchanged, but certainly not increased. However, this revision can modify some of the conclusions on this peculiar population.

4.3. Examination of the stellar radial velocities

With the radial velocities of all the helium stars reported by Eckart & Genzel (1997), considered as the most recent estimations, and in Krabbe et al. (1995) when the value was missing from Eckart & Genzel (1997), we have constructed a plot to compare to our estimations (Fig. 3). The error bars of each measurement are given, which put each star symbol at the center of an error box. In our work the error bars of V_R reported in Figs. 1 and 2 were estimated by shifting each best-fit profile in velocity, so that the maximum error in the obs.-calc. curve was within $\pm 1\sigma$ of the noise. We can notice that our error bars are generally smaller than those reported earlier. However, the diagonal line does not cross the error box for 3 stars: N2, N5 and B2, i.e., IRS 16C, IRS 33SE and IRS 7E2. For either N2, which has a particularly narrow error bar because the emission is strong, or N5, the stellar profile has been corrected for the ISM emission. That may explain the observed discrepancy if in Eckart & Genzel’s work this correction was not done. We return to the case of N5 in Sect. 5.1. No correction for ISM emission has had to be made for B2. The low contrast of the emission line explains a wider error bar. However, the difference of reported V_R has no obvious explanation, unless IRS 7E2 is another spectroscopic binary, which gave two different radial velocities when observed at two different epochs (difference of $\simeq 200 \text{ km s}^{-1}$). Further observations are needed to assess this plausible hypothesis.

4.4. Location and kinematics of the He I stars

From the offsets given in Figs. 1 and 2, a map of the He I stars centered on SgrA* is presented in Fig. 4. The two classes of stars are distinguished by different symbols. Another property becomes apparent on this map. The narrow-line stars are grouped into a central compact cluster, in the IRS 16 region. Actually, 4 of them are designated as being components of IRS 16. The new star He I N2 is in the middle of them. The most external sources are IRS 33SE and IRS 34W, located just a few arcseconds South and West, respectively of the IRS 16 cluster. On the contrary, the broad-line stars are randomly distributed at the periphery of the field, beyond an inner radius of $\simeq 0.3$ pc from SgrA*. Thus, the two or three emission-line stars missing because located at the edge of the observed field (Sect. 4.2) should also belong to the broad-line group.

In Fig. 5 are placed all the radial velocities (V_R) reported in Figs. 1 and 2, with their error bars, as a function of the dec.-offset of the sources from SgrA*. This plot is constructed with the same axes as a comparable diagram in Genzel et al. (1996) for the early-type stars. According to these authors all the stars with a positive velocity are concentrated in the upper left quadrant while the stars with a negative velocity are in the lower right quadrant. They conclude that this diagram shows the signature of a coherent retrograde motion of all early-type stars – a population of stars which contains mostly the He I stars – around an approximately East-West axis of rotation through SgrA*. From our equivalent diagram (Fig. 5) with the velocities of the 16 confirmed He I stars, we note that stars are present in all 4 quadrants, with, however, a trend to be mostly distributed along a diagonal through the opposite upper left and lower right quadrants, which is consistent with a revised version of the same diagram by Genzel et al. (2000).

4.5. Absorption line stars

From the systematic inspection of the 90 stellar spectra extracted from the data cube, it appears that some stars might present a broad absorption feature at the position of the He I 2.058 μm line. Tamblyn et al. (1996), and more completely Hanson et al. (1996) have observed all types of OB stars in the K band. They show that giant and supergiant O-type stars, roughly from O5 to O9 may have the He I 2.058 μm line in weak absorption. The search for such stars was conducted with the same method as the one applied to the emission line stars. Similarly, a smoothing of the raw spectra was made since the absorptions are broad (FWZI between ~ 900 and 1500 km s^{-1}) and shallow. The more noticeable detections correspond to the sources: IRS 7SE, IRS 14SW, MPE-1.1-2.2 and IRS 3. From the photometric survey of Ott et al. (1999), these stars are relatively bright (m_K between 10 and 11.3) with a low index of variability. Note that IRS 14SW and IRS 3 are indicated as cool stars in Blum et al. (1996a),

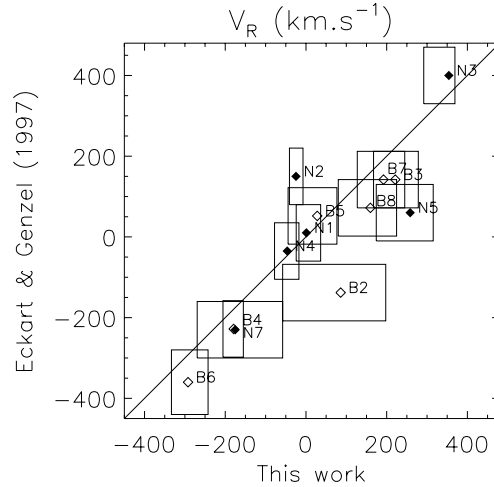


Fig. 3. Comparison of the estimated radial velocities V_R with their error boxes for the stars in common between our work and Eckart & Genzel (1997). When not available in that paper, the values are from Krabbe et al. (1995). The narrow-line stars are represented by a filled diamond, the broad-line stars by an open diamond. See Figs. 1 and 2 for the star identifications

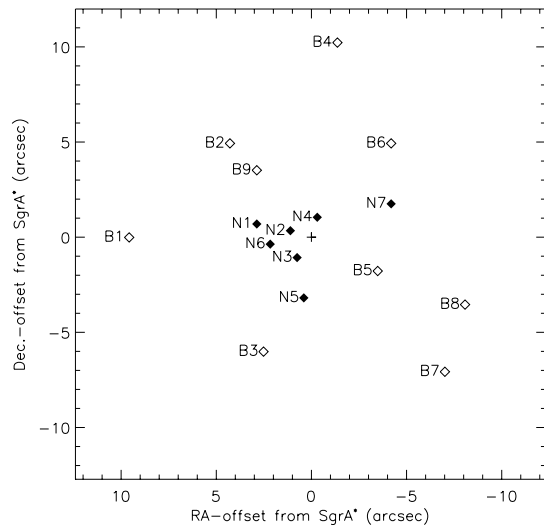


Fig. 4. Spatial distribution of helium stars from the offsets reported in Figs. 1 and 2, with respect to SgrA* marked by a cross. The symbols have the same meaning as in Fig. 3

with the latter characterized as “embedded” by Eckart & Genzel (1997). Hence, this absorption can be of an origin other than photospheric helium. However, IRS 7SE and MPE-1.1-2.2 remain as potential OB star candidates. Observations over a wider spectral range are necessary to confirm the spectral nature of these two sources, which deserve further attention as possible indicators of the presence of O-type stars in the central cluster.

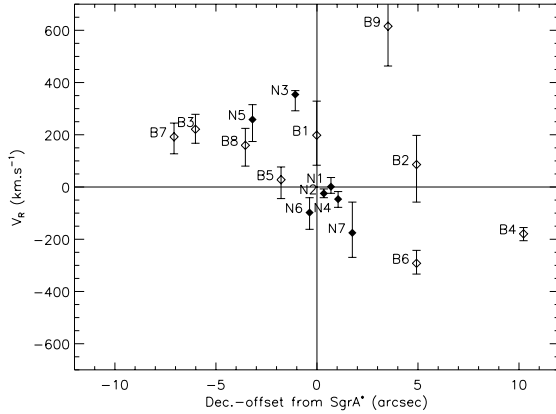


Fig. 5. Radial velocities with their error bar of the helium stars as a function of the dec.-offset from SgrA* (see Figs. 1 and 2). Filled and open diamonds have the same meaning as in Figs. 3 and 4

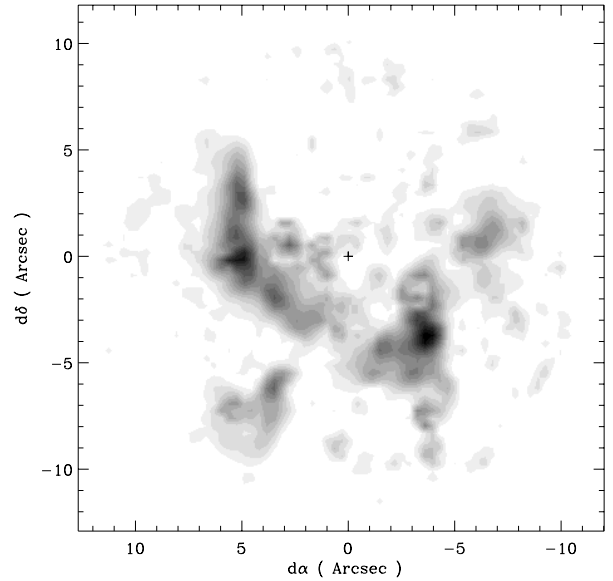


Fig. 6. Image of the helium streamers in the 2.058 μm line. The emissions of stellar origin have been subtracted as much as possible. Small residuals remain. The position of SgrA* is marked by a cross at the center of the field

4.6. Helium streamers

An image of the interstellar helium emission is shown in Fig. 6. It was constructed by putting at each pixel the peak value of the corresponding spectrum in the ISM cube. The emission appears clearly distributed in coherent gas lanes. By comparing with the interstellar emission previously mapped in Ne^+ at 12.8 μm by Lacy et al. (1991) and in $\text{Br}\gamma$ (Morris & Maillard 2000 and references therein) we see that this emission emanates from the Mini-Spiral, particularly prominent the Northern arm and the Bar. The mini-cavity can be also recognized. The Eastern arm is weak, except in an elongated feature at its western tip, at $d\alpha = -1.5''$, $d\delta = -2.5''$, showing a very distinct and extreme redshifted velocity. This component appears clearly in the integrated ISM velocity profile shown in Fig. 7, where it forms a separated maximum at $+275 \text{ km s}^{-1}$. The same peak of velocity is observed in the $\text{Br}\gamma$ data (Morris & Maillard 2000) at the same position on the hydrogen streamers. The full range of velocity covered by the He I mini-spiral is identical to the range measured in $\text{Br}\gamma$, i.e., $-400, +400 \text{ km s}^{-1}$ (Morris & Maillard 2000). However, the helium ISM emission appears simpler than the $\text{Br}\gamma$ emission, as attested by the line profile extracted at each pixel which appears always as a single and narrow emission peak, except where the main streamers are crossing. For example, three components are exceptionally observed where the Northern arm, the Bar and the feature of the Eastern arm are superimposed, at $d\alpha = 3''$, $d\delta = -6''$. We already mentioned that the linewidth of a single component is exactly equal to the current limit of resolution. We can conclude that the velocity width of the helium streamers is certainly $< 70 \text{ km s}^{-1}$, however without being much narrower, since no sinc function profile is observed.

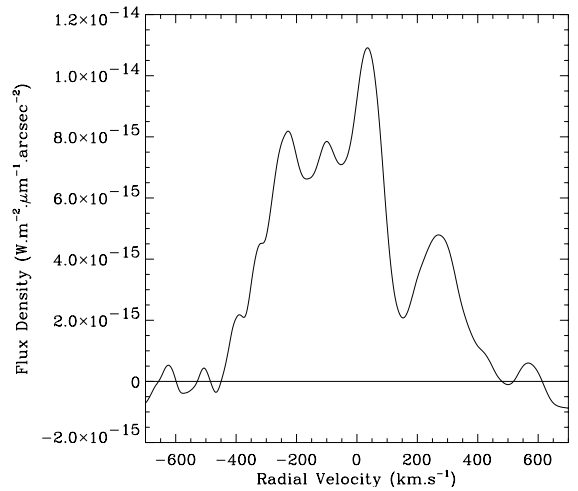


Fig. 7. Full velocity profile of the He I Mini-Spiral obtained by extracting the spectrum from the ISM cube over a mask covering most of the emission. The calibrated flux density is an average by arcsec^2 over the area of this mask

4.7. Comparison of the radial velocities of the He I stars and the local ISM

As already mentioned, for several fully resolved He I line profiles, a narrower emission line from a helium streamer is seen superimposed on the stellar profile. By comparing the V_R of these stars derived from their P Cygni profile emission (Figs. 1 and 2) with the radial velocity of the He I streamer along the same line of sight, we note that for many of them the two velocities are quite comparable

Table 3. Comparison of the radial velocities of the He I stars and the local ISM

ID	Name	V_R Star (km s ⁻¹)	V_R ISM (km s ⁻¹)
N1	IRS 16NE	+ 1 ± 30	+ 16
N2	IRS 16C	- 24 ± 17	- 84
N6	HeI N2	- 97 ± 60	- 58
N7	IRS 34W	- 175 ± 100	- 150
B2	IRS 7E2	+ 85 ± 130	+ 70
B3	IRS 9W	+ 221 ± 55	+ 309
B6	IRS 7W	- 292 ± 45	- 250

in amplitude, and with the same sign. The comparison is presented in Table 3 with the narrow-line stars in the upper part, and the broad-line stars in the lower part.

5. Notes on individual He I stars

In the following we discuss the peculiarities of some of the emission line profiles separated into the two classes presented in Figs. 1 and 2, and in Tables 1 and 2.

5.1. Narrow-line stars

- **[N3] IRS 16SW:** This star shows a clear P Cygni profile with a $FWHM$ of the emission component of 258 km s⁻¹. However, from all the stars of this class (Fig. 1) this one has the largest positive radial velocity of 354 km s⁻¹. Ott et al. (1999) have been able to show from photometric observations that this star is a short-period variable, and therefore is probably a massive eclipsing binary. Consequently, the radial velocity plotted in Fig. 5 is not representative of the system itself, because of the contribution of the orbital velocity which could be as high as 677 km s⁻¹ from Ott et al. (1999). This might explain the reason for which the diagonal in Fig. 3 barely crosses the error box.
- **[N5] IRS 33SE:** Its He I line profile does not show a P Cygni profile. This star lies in the helium Mini-Spiral, and the spectrum of the source before correction shows several ISM components, one of which falls where the absorption component should be. It was not possible in the correction of the stellar line profiles to recover this probable absorption component. Therefore, IRS 33SE might have a regular P Cygni profile which would imply a less positive radial velocity than displayed in Fig. 5. It would explain the discrepancy with the estimation of Eckart & Genzel (1997) noted in Sect. 4.3, and shown in Fig. 3, as long as the estimation was based on the line of an element not present in the Mini-Spiral. It cannot be from Br γ for which the ISM emission strongly affects the stellar profiles (Morris & Maillard 2000).
- **[N6] HeI N2:** A nearby star, IRS 16CC, is reported as a helium star in Blum et al. (1996a), but by combining the BEAR data and the AO image as

explained in Sect. 3.6, we find that the true helium star is in fact a fainter star, located 0.6'' South and 0.3'' East of IRS 16CC. This newly detected helium stars lies both in the wings of He I stars IRS 16NE and IRS 16C and in the Northern Arm of the ISM emission, which makes it difficult to identify. This star has the weakest m_K in the narrow-line profile group (Table 2), with a value typical of the broad-line group.

- **[N7] IRS 34W:** This identification is reported in Krabbe et al. (1995) while Blum et al. (1996a) indicate simply IRS 34. From the AO image there are effectively two stars of comparable brightness, IRS 34E and IRS 34W, 0.4'' to the South-West, within the BEAR box. The value of the continuum given in Table 1 and the magnitude in Table 2 is corrected for the contribution of IRS 34E. With the S/N ratio of the spectrum (Fig. 1) we cannot confirm a P Cygni profile for this line. This star has an m_K value comparable to that of HeI N2. These two stars form a sub-group in the narrow-line group, which is discussed in Sect. 6.1.2.

5.2. Broad-line stars

- **[B1] ID 180:** This star is another of the newly detected helium stars. It falls in coincidence with a star for which the photometry is given in Ott et al. (1999);
- **[B2] IRS 7E2:** We propose this new identification for the helium star initially indicated as IRS 7E. From the AO image (Fig. 2) there are clearly two components, not noted before, that we defined as IRS 7E1 and IRS 7E2, separated by 0.37''. IRS 7E2 is well centered within the BEAR box. The flux in Tables 1 and 2 is corrected correspondingly;
- **[B5] IRS 13E3:** This helium star was originally designated simply as IRS 13E (Krabbe et al. 1995; Blum et al. 1996a). In a later paper, IRS 13E1 is given as the helium star (Najarro et al. 1997a), whose photometry is given by Ott et al. (1999) along with the other component IRS 13E2, indicating two equally bright components ($m_K = 10.26$) separated by $\sim 0.14''$, which is the current limit of resolution of this work after deconvolution. By a local zoom of the AO image (Fig. 8), a fainter third component is seen, that we call IRS 13E3. By applying the procedure described in Sect. 3.6 the bright BEAR pixel is projected onto the AO image. The flux in the 2.058 μ m line could come from either 13E2 or 13E3. The helium source in this complex is a broad-line star, therefore with a relatively weak continuum. As the faintest component, IRS 13E3 is the most plausible candidate. The K magnitude in Table 2 corrected accordingly ($m_K = 11.73$) provides a value in agreement with the magnitude of the stars of the same group, which would not be the case with IRS 13E2. Of course, only diffraction-limited spectro-imaging can unambiguously confirm this identification. Otherwise, the line profile presented in Fig. 2 is one of those where

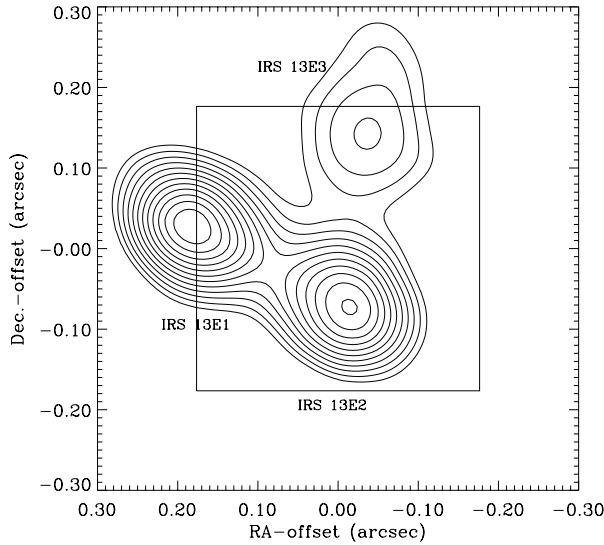


Fig. 8. Zoom of the K -band adaptive optics image in contour on the IRS 13E complex showing the 3 stellar components. The square box represents the position of the maximum intensity BEAR pixel at the IRS 13 position in the line cube, projected on the AO image. IRS 13E3 is considered to be the helium star (see Sect. 5.2)

an important correction to remove the ISM contribution, made of several components, was needed. This results in a very flat top;

- **[B7] AF:** This object has been long recognized as a helium star and has been the subject of detailed studies, in particular by Najarro et al. (1994). However, in the broad-line class of objects this star is an exception, with a continuum brighter than all the members of this group (Tables 1 and 2). The intensity of the emission relative to the continuum (Fig. 2) is comparable to the intensity of other stars of this group, but intrinsically, the line emission is the most intense of all the helium stars. From the AO image, there is a cluster of 5 sources with one dominant source. The BEAR aperture contains this source plus two of the fainter sources. From Ott et al. (1999), this star presents a strong index of variability, the origin of which is not determined. The possibility that the variability is periodic should be checked, as that might indicate a compact binary star which could explain the peculiarity of this star. At any rate, AF cannot be considered as typical for all the other He I stars, as implied by Najarro et al. (1994, 1997a);
- **[B9] HeI N3:** This is the third new helium star. Its corresponding object in the AO image was found with a K magnitude (Table 2) in agreement with the mean value found for the broad-line stars. The line shows the largest redshift among all these stars. The error bar is large since the emission is relatively weak. The S/N ratio is not high enough to show a P Cygni profile.

6. Discussion

The main results from this study of the helium emission-line stars in the central pc of the Galactic Center can be summarized as follows:

- 1) Sixteen fully resolved P Cygni emission line profiles, purely of stellar origin, are extracted;
- 2) They divide into two distinct classes, with narrow and broad-line profiles;
- 3) The stars in each group have a comparable K magnitude but the two groups show a mean difference of ~ 2 mag;
- 4) The spatial distribution of the two groups is different. The narrow-line objects are all arranged in a central cluster, while the other class are dispersed in a ring beyond a radius of $\simeq 0.3$ pc from SgrA*;
- 5) ISM emission of helium streamers which follow the Mini-Spiral is discovered. The radial velocity of these flows seen along the line of sight to a large fraction of the helium stars is comparable to the radial velocity of the underlying star.

Hence, we must examine all the observed findings to determine what they tell us about the nature and the formation of these stars.

6.1. The stellar type of the He I stars in the inner GC

The P Cygni lineshape for the helium emission of most of the stars we observed indicates that all of them are hot stars which possess an extended atmosphere in rapid expansion. However, the two different classes of line profile associated with the remarkable anti-correlation with the continuum brightness call for two different types of hot, helium-rich stars. IRS 16C and IRS 7W are typical examples of each class. The differences cannot be ascribed to orientation, such as an equatorial gaseous envelope seen edge-on or pole-on, as has been proposed to explain the two different types of emission line profiles in Be stars. Over the set of sources a continuity in the linewidths would be observed, with a double peak in some cases, while a single line is always observed, but with two radically different linewidths. These profiles are clearly suggestive in all cases of strong wind outflows. To which stellar types do these different profiles belong? Do they correspond to massive, hot stars but at two different stages of evolution?

6.1.1. The stellar types of massive, hot stars

The question of the stellar type of the He I stars has already been examined by all the authors who have previously studied this stellar population. Note that they all make the preliminary remark that the study of the early-type GC stars forces a revision of the usual stellar classification criteria, generally based on visible spectra, to find their translation in the near infrared. This has triggered various spectroscopic studies of hot stars conducted in the K band, by Hanson & Conti (1994), Blum et al. (1995b),

Tamblyn et al. (1996), Morris et al. (1996), Hanson et al. (1996), and Figer et al. (1997). It turns out that the hot stars which exhibit the HeI 2.058 μm line in emission belong to a large variety of spectral types, from normal Oe, Be stars and B supergiants (Hanson et al. 1996) to sub-types of peculiar, luminous stars which are the B[e], LBV (Luminous Blue Variables), WR stars, and intermediate types like ON, Ofpe, Ofpe/WN9, undergoing a strong mass loss. Discussion of these various stellar types are included in Libonate et al. (1995) and in Tamblyn et al. (1996) who discuss the helium stars in the GC. Tracks of evolution of massive stars, depending on the initial mass and the metallicity, have been proposed by Meynet et al. (1994). A typical sequence for massive stars, for example of $60 M_{\odot}$, is: O, Blue Supergiant, LBV and WR, as they evolve to becoming SNs. The WR stars represent the final stage of evolution of massive O stars of initial mass $\geq 40 M_{\odot}$. Two main sub-classes, the WN and the WC stars, depend on their phase of nucleosynthesis, the WC stars being the most evolved of the WR stars (Abbott & Conti 1987).

The K -band atlas of Figer et al. (1997) is devoted to the WR stars. These authors conclude that from this spectral range it is not easy to distinguish between individual sub-types, in particular for WC stars since their K spectra tend to be quite similar. Regarding the 2.058 μm line, they show that this line is present in late WN-types and otherwise, is particularly prominent in WC9 types. That is partially confirmed by Tamblyn et al. (1996), who also mention a strong 2.058 μm line with a P Cygni profile for the WN8 and the LBV members of their star sample. They also note the line in simple emission, for the few late ON-type and early B-type supergiants they observe. Hanson et al. (1996) detect the line in emission for OeV et BeV stars but with a complex profile, and otherwise in supergiant B1 stars. Finally, it seems difficult to draw very clear conclusions since all these intermediate classes, such as LBV, ON or Ofpe, represent very rare groups of stars. For example, from a review of the statistics of LBVs and related stars by Parker (1997), there are only 5 confirmed LBV stars in the Milky Way disk, including the two famous examples P Cygni itself and η Car, and only 26 more within 8 nearby galaxies, including the LMC and SMC. However, Parker notes that there are more candidates if more “liberal definitions” are applied, which means that it is not possible to generally assign a strict spectral type to these stars, in particular from a study carried out only within a limited spectral range.

The WR stars are known for extremely broad emission lines (Abbott & Conti 1987), for which the values of $\sim 1000 \text{ km s}^{-1}$ and more are typical, comparable to the $FWHM$ reported in Fig. 2. On the other hand, the line profile observed for HeI in the LBV star P Cygni is quite comparable to the 2.058 μm line profiles we call narrow-line profiles (Fig. 1). High resolution observations of the infrared emission lines of P Cygni by Najarro et al. (1997b) give lines with profiles having widths fitted by a model with a terminal velocity of 185 km s^{-1} and a T_{eff} of

18100 K. The existence of an extended helium envelope for P Cygni is given by the interferometric observations of Vakili et al. (1997) in the HeI 6678 \AA line. They estimate a photospheric radius $R_{\star} = 76 \pm 15 R_{\odot}$ and an extent of the helium envelope of $12.5 R_{\star}$.

6.1.2. The HeI stars as LBV and WR-type stars

Thus, from only the consideration of the two distinct types of HeI line profiles, the helium stars with narrow-line profiles should be most closely related to LBV-type stars, while the other group to WR-type stars, without trying to be more specific. Tamblyn et al. (1996), who had already noticed few HeI stars in the inner pc with narrower line profiles, have considered whether these sources might be LBVs. They contest this hypothesis on the basis that LBV stars are a too brief phase of stellar evolution, which explains their rarity, and that these stars are not hot enough to be efficiently detected in the 2.058 μm emission line. This conclusion is based on the observation of only two galactic LBV stars, of which effectively only one (P Cygni) shows clearly the 2.058 μm line in emission, whereas the other has a poor S/N ratio. Thus, these arguments are not very convincing.

One of the general parameters which distinguishes these two types of stars is their range of effective temperature (T_{eff}). Hence, a range of T_{eff} is reported from observations of LBVs (Crowther 1997), from 8000 K to ~ 25000 K, while for WRs the range is definitely beyond, from 30000 to ~ 90000 K (van der Hucht et al. 1991). For all these stars, the 2 μm region is far from the maximum of emission. However, although hotter, the WR stars are intrinsically dim among massive stars, because of their relatively small photosphere radii. WC stars are typically $10^5 L_{\odot}$. These can be contrasted to LBV stars, which sit near the Humphreys-Davidson limit, typically above $10^6 L_{\odot}$. This fundamental difference is attributable to the copious mass loss experienced by the most massive O stars ($M \simeq 120 M_{\odot}$) which will end their lives with a mass between 5 and $10 M_{\odot}$, when they are WR stars. Thus, this distinction between LBV and WR fits also with the observed difference in K magnitude between the two groups of HeI stars (point # 3 of the summary).

The particular cases of IRS 34W and HeI N2 must be discussed within the framework of this classification. These two stars belong to the LBV-type group from their line profile, but with an m_K typical of the other group (Table 2). The few galactic LBVs studied in detail are known to be characterized by giant eruptions which are followed by dust obscuration. From the reconstructed light curve of η Car (Humphreys et al. 1999), the maximum obscuration lasted about ~ 40 years since the last eruption. From its pre-outburst level it had undergone a 4-mag visual extinction. These two LBV-type star candidates might be in such a phase.

In conclusion, we propose that the class of narrow-line stars consists of LBVs or related stars in the 10000

to 20000 K range of T_{eff} , while the second class consists of much hotter stars (≥ 30000 K), late-type WR stars, predominantly in the WC9 stage, according to the conclusions of Figer et al. (1997) from their K -band atlas of WR stars. The latter is also in agreement with the classification properly made for one helium star (BSD WC9) by Blum et al. (1995a). However, from these considerations only, the mere distinction between luminous blue stars and LBVs is not really possible. Strictly speaking, variability should be established to identify an LBV. That is only suggested by the status of IRS 34W and HeI N2 compared to the other sources of the group. While WR stars seem the most likely for one group, only the proximity in evolution pleads in favor of LBV-related status for the other group, which is discussed in the next section, in relation to their spatial distribution (point # 4 of the summary).

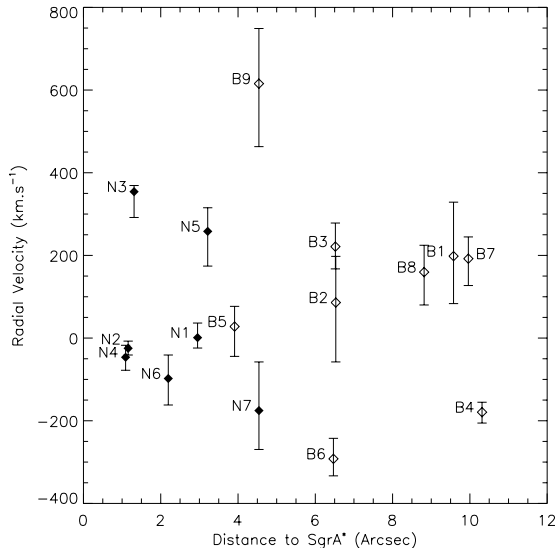


Fig. 9. Observed radial velocity of the He I stars as a function of projected distance from SgrA*. Symbols have the same meaning as in Fig. 3

6.2. Spatial distribution of the He I star and their formation

Is the above classification the result of a sequence of evolution, since LBVs are precursors of WR stars? A parameter to take into account is the initial mass of the progenitors. An important conclusion of the evolutionary tracks of Meynet et al. (1994) is that, for the most massive stars – $\geq 120 M_{\odot}$ – the LBV stage is avoided to go directly from O or Of to late WN, then WC and SN. Therefore, to be of the same age, the LBV-type stars must have originated from massive O stars in the range 40 to $120 M_{\odot}$ while the WR group should be originating from stars of

initial mass $\geq 120 M_{\odot}$, which thus reached directly the WR stage where they are currently observed.

The placing in Fig. 9 of the radial velocities as a function of the projected distance of the sources from SgrA* is another way of showing the two groups clearly distributed in two concentric volumes around SgrA*, with approximately equal velocity distribution. If we adhere to the coeval formation scenario, then the difference of spatial distribution of the two types of He I stars, presented in Figs. 4 and 9, must be explained in this context, and we ask if that should be the signature of the star formation process.

6.2.1. The WR-type star ring

Figures 4 and 9 suggest that there are no orbits of WR stars in planes perpendicular to the plane of the sky, since we do not see any of them projected close to SgrA*. Also, we measure radial velocities for these stars between -300 km s^{-1} and $+600 \text{ km s}^{-1}$ (Fig. 9). So, the orbits cannot be in the plane of the sky either, or all the V_{R} s would be close to 0. Thus, in agreement with Genzel et al. (2000), we can conclude that the orbits of these stars reside roughly in a disk inclined by 40° off the plane of the sky, with quasi-circular orbits, which fits with their distribution in a ring of ~ 0.2 pc radial width, centered on SgrA*. The sign of the radial velocities (Fig. 5) is consistent with the orbits described in a general clockwise sense, as derived from proper motions studies (Genzel et al. 2000). However, these authors note that “the fit of the best Keplerian disk model to the He I star velocities is poor”.

6.2.2. The LBV-type star cluster

The stars with narrow-line profiles are grouped in a cluster close to SgrA*. If circular orbits are also assumed for these stars the orbital radii must be small in order for them to appear as a cluster in projection. For the closest He I stars to SgrA* (N2, N3 and N4 in Fig. 9, within a radius of 0.06 pc) the orbital velocity should be of the order of 600 km s^{-1} . The largest measured radial velocity is 354 km s^{-1} for N3, so pure Keplerian motions are possible for these stars. With such velocities on a small orbital radius, a proper motion becomes detectable within a few years, as reported by Ghez et al. (1998) and Genzel et al. (2000). Then, for star N2 (IRS 16C) for which a V_{R} of only -24 km s^{-1} is measured (Fig. 9) the modulus of the projected proper motion velocity is 480 km s^{-1} from the measurements of Genzel et al. (2000). With the correction for projection an orbital velocity consistent with circularity is possible. At least, from the observations, very elongated orbits are excluded.

6.2.3. Tentative conclusions

The massive, hot stars are concentrated in the central pc around SgrA*. To remain concentrated in that position

requires that their orbits are dominated by the gravitational field of the central Black Hole. From the conclusions of Genzel et al. (2000), the overall rotation of the He I cluster is a remnant of the original angular momentum pattern in the interstellar cloud from which these stars formed. Indeed, they may have formed together in a gaseous disk orbiting the central black hole, less than ~ 5 Myr ago from the life-time of WR stars. However, our observations imply that the stars differentiated according to their distance from the central Black Hole, into two star groups, distinguished by their initial mass, with more massive stars forming at a larger distance. This could be obtained, actually, if the initial disk was formed of two separate rings, one with a mean radius of ~ 0.04 pc, the other one of ~ 0.3 pc. If in addition, the SgrA* cluster (Genzel et al. 1997; Ghez et al. 1998) is considered, it continues the trend toward smaller masses located inward. These stars form a separate third group of main sequence, early-type stars (Genzel et al. 2000). Then, all these early-type stars may have formed in the same star formation event from a gaseous disk around the central mass, but with annular structures, probably caused by tidal forces, which remain to be explained.

6.3. The link between He I streamers and He I stars

As very hot stars and with helium dominating their chemical composition, WR stars are sources of a strong ionizing flux (Schmutz et al. 1992), thus implying the presence of a hard UV field in the inner pc. This is consistent with the presence of the helium Mini-Spiral (Fig. 6) we detect in emission in the near infrared, since hard ionizing photons are required to excite this line in the ISM. However, this UV field cannot penetrate very deep into the flows, because it will be blocked by the dust. Therefore, the helium streamers should delineate the inner regions of the gaseous Mini-Spiral. That is likely the reason for which the helium emission map (Fig. 6) appears simpler than in Br γ (Morris & Maillard 2000), and why the linewidth is relatively narrow (< 70 km s $^{-1}$). However, as mentioned in Sect. 4.6, the same main emission structures are seen in He I and in Br γ , as well as in Ne $^+$ (Lacy et al. 1991). The ISM helium data cube indicates that the gas is distributed in several flows. But these gaseous orbits do not follow the early-type star distribution which has been described above. This implies that the overall kinematics of the gas and these stars are different. However, we noticed a similarity of radial velocity (point # 5 of the summary) between the He I stars and the He I streamers, along the same line of sight (Table 3). This suggests that the kinematics of the streamers, within a radius of ~ 0.5 pc from SgrA*, become mainly dominated by the gravitational field of the central Black Hole. At further distances reached by the Mini-Spiral, the field is more complex, with the contribution of all the other stars, which are essentially late-type stars. From the photometric survey of the central 5 parsecs of the Galaxy by Blum et al. (1996a) it can be estimated that $\sim 80\%$ of the known stellar population is

comprised of stars identified as late-type giants and supergiants (e.g. IRS 7) by their CO absorption (Blum et al. 1996b). These K, M and AGB stars which correspond to a mass range of $2-8 M_{\odot}$ (except for the few supergiants) are likely much older ($\sim 10^8-3 \cdot 10^9$ yr) than the current helium stars. They must have been produced in a totally different star formation event. They are stars with important mass loss, but not of helium-enriched material. Hence, this suggests that the observed concentration of He I stars should be the major source of enhancement of the helium abundance in the inner GC. From the average mass loss rate reported for LBV and WR stars, and with the presence of around 20 of such stars, the total mass loss rate, only from all these stars in the central pc, could be estimated at $\sim 2 \cdot 10^{-3} M_{\odot}/\text{yr}$. The dynamical time for the gas in the streamers of SgrA West is about 10^4 yr, so on this time scale, $\sim 20 M_{\odot}$ of He-enriched stellar material might be mingling with the infalling matter in the streamers. The observed similarity of velocity, in amplitude and sign, of the He I stars and of the flows suggests a close link in the formation of both. The helium-rich Mini-Spiral might be the precursor of the disk in which will form the next, massive, hot star generation.

7. Conclusions and perspectives

New results on the population of He I stars in the inner region of the Galactic Center have been obtained with the firm indication of two classes of massive hot stars, which suggest a formation in a disk of gas around SgrA*. This analysis is based on a single line, the He I 2.058 μm line. Of course, while that is not sufficient to establish a complete spectral classification, one can nonetheless consider that this study represents a necessary initial selection test, since it has been shown that several stars in previous studies were wrongly considered as He I stars. By consequence, it illustrates also the risk of false detections in the search for emission-line stars toward the inner Galaxy simply by using narrow-band photometry centered on the He I 2.058 μm line, or other near-infrared emission lines. The importance of high spectral resolution combined with high spatial resolution is paramount for distinguishing stellar and interstellar emission. Similar data obtained with BEAR already exists on Br γ (Morris & Maillard 2000). With the same effort for separating the stellar and the interstellar component, the Br γ line profile for the 16 confirmed He I stars should be retrieved, making another test on this stellar population. The next goal is a larger spectral coverage to complete the spectral criteria. That has already been done by several previous works, but always at medium resolution and with slit spectrometers, for which the source confusion is not easily controlled. Only a slitless technique like that employed by BEAR makes this control possible. Also, similar studies on other critical lines must be conducted. However, the next major step, instead of spectro-imaging at seeing-limited resolution as we have presented, and tried to improve by combining with AO imaging, will be infrared spectro-imaging at the

diffraction-limited spatial resolution of a large telescope. That is the only way to detect more sources in order to remove all the identification ambiguities. As illustrated here, this should be combined with a spectral resolution of at least 5000, which is not an easy goal.

Finally, it would be important to conduct similar studies in other stellar clusters like the “Arches” and “Quintuplet” clusters (Figer et al. 1999a, 1999b) where the identification of LBV stars has also been proposed, notably the Pistol star (Figer et al. 1999c), to determine comparatively the conditions of evolution of young compact clusters at Galactocentric distances well beyond the central pc of the Milky Way.

Acknowledgements. We would like to thank warmly Doug Simons (now at Gemini) who participated actively in the early development of BEAR and designed the camera Redeye, which is used on the instrument. He was part of the observing run when the data were acquired, and of a preliminary run the year before. We are also grateful to the CFHT staff for the technical support of BEAR and of the data acquisition program which is associated.

References

- Abbott, D. C., & Conti, P. S. 1987, *ARA&A*, 25, 113
- Allen, D. A., Hyland, A. R., & Hillier, D. J. 1990, *MNRAS*, 244, 706
- Blum, R. D., Sellgren, K., & DePoy, D. L. 1995a, *ApJ*, 440, L17
- Blum, R. D., DePoy, D. L., & Sellgren, K. 1995b, *ApJ*, 441, 603
- Blum, R. D., Sellgren, K., & DePoy, D. L. 1996a, *ApJ*, 470, 864
- Blum, R. D., Sellgren, K., & DePoy, D. L. 1996b, *AJ*, 112, 1988
- Castor, J. I., & Lamers, H. J. G. L. M. 1979, *ApJS*, 39, 481
- Crowther, P. A. 1997, in *Luminous Blue Variables: Massive Stars in Transition*, ed. A. Nota, & H. Lamers, *ASP Conf. Ser.*, 120, 51
- Doyon, R., Nadeau, D., Vallée, P., et al. 1998, in *Infrared Astronomical Instrumentation*, ed. A. M. Fowler, *Proc. SPIE*, 3354, 760
- Elias, J. H., Frogel, J. A., Mathews, K., & Neugebauer, G. 1992, *AJ*, 87, 1029
- Eckart, A., & Genzel, R. 1997, *MNRAS*, 284, 576
- Figer, D. F., McLean, I. S., & Najarro, F. 1997, *ApJ*, 486, 420
- Figer, D. F., McLean, I. S., & Morris, M. 1999a, *ApJ*, 514, 202
- Figer, D. F., Kim, S. S., Morris, M., et al. 1999b, *ApJ*, 525, 750
- Figer, D. F., Morris, M., Geballe, T. R., et al. 1999c, *ApJ*, 525, 759
- Geballe, T. R., Krisciunas, K., Bailey, J. A., & Wade, R. 1991, *ApJ*, 370, L73
- Genzel, R., Thatte, N., Krabbe, A., Kroker, H., & Tacconi-Garman, L. E. 1996, *ApJ*, 472, 153
- Genzel, R., Eckart, A., Ott, T., & Eisenhauer, F. 1997, *MNRAS*, 291, 219
- Genzel, R., Pichon, C., Eckart, A., Gerhard, O. E., & Ott, T. 2000, *MNRAS*, 317, 348
- Ghez, A. M., Klein, B. L., Morris, M., & Becklin, E. E. 1998, *ApJ*, 509, 678
- Hall, D. N. B., Kleinman, S. G., & Scoville, N. Z. 1982, *ApJ*, 260, L53
- Hanson, M. M., & Conti, P. S. 1994, *ApJ*, 423, L139
- Hanson, M. M., Conti, P. S., & Rieke, M. J. 1996, *ApJS*, 107, 281
- Humphreys, R. M., Davidson, K., & Smith, N. 1999, *PASP*, 111, 1124
- van der Hucht, K. A. 1991, in *Wolf-Rayet Stars and Interrelations with Other Massive Stars in Galaxies*, *IAU Symp.* 143, ed. K. A. van der Hucht, & B. Hidayat, 19
- Krabbe, A., Genzel, R., Drapatz, S., & Totaciuc, V. 1991, *ApJ*, 382, L19
- Krabbe, A., Genzel, R., Eckart, A., et al. 1995, *ApJ*, 447, L95
- Lacy, J. H., Achtermann, J. M., & Serabyn, E. 1991, *ApJ*, 380, L71
- Lai, O., Véran, J. P., Rigaut, F., et al. 1997, in *Optical Telescopes of Today and Tomorrow*, ed. A. L. Ardeberg, *Proc. SPIE*, 2871, 859
- Libonate, S., Pipher, J. L., Forrest, W. J., & Ashby, M. L. N. 1995, *ApJ*, 439, 202
- Lutz, D. 1998, in *The Universe as seen by ISO*, ed. P. Cox, & M. F. Kessler, *ESA Pub.*, SP-427, 623
- Maillard, J. P., & Michel, G. 1982, in *Instrumentation for Astronomy with Large Telescopes*, *IAU Coll. No.* 92, ed. C. M. Humphries (D. Reidel, Pub.), 213
- Maillard, J. P. 1995, in *Tridimensional Optical Spectroscopic Methods in Astrophysics*, *IAU Col.* 149, ed. G. Comte, & M. Marcelin, *ASP Conf. Ser.*, 71, 316
- Maillard, J. P. 2000, in *Imaging the Universe in 3 Dimensions*, ed. E. van Breughel, & J. Bland-Hawthorn, *ASP Conf. Ser.*, 195, 185, available at <http://www.aao.gov.au/local/www/jbh/3D/>
- Menten, K. M., Reid, M. J., Eckart, A., & Genzel, G. 1997, *ApJ*, 475, L111
- Meynet, G., Maeder, A., Schaller, D., & Charbonnel, C. 1994, *A&AS*, 103, 97
- Morris, M. 1985, in *Mass Loss from Red Giants*, ed. M. Morris, & B. Zuckerman (Dordrecht: Reidel), 124
- Morris, M. 1993, *ApJ*, 408, 496
- Morris, M., & Maillard, J. P. 2000, in *Imaging the Universe in 3 Dimensions*, ed. E. van Breughel, & J. Bland-Hawthorn, *ASP Conf. Ser.*, 195, 196, available at <http://www.aao.gov.au/local/www/jbh/3D/>
- Morris, P. W., Eenens, P. R. J., Hanson, M. M., Conti, P. S., & Blum, R. D. 1996, *ApJ*, 470, 597
- Najarro, F., Hillier, D. J., et al. 1994, *A&A*, 285, 573
- Najarro, F., Krabbe, A., Genzel, R., et al. 1997a, *A&A*, 325, 700
- Najarro, F., Hillier, D. J., Lamers, H. J. G. L. M., et al. 1997b, in *Luminous Blue Variables: Massive Stars in Transition*, ed. A. Nota, & H. Lamers, *ASP Conf. Ser.*, 120, 105
- Ott, T., Eckart, A., & Genzel, R. 1999, *ApJ*, 523, 248
- Parker, J. W. 1997, in *Luminous Blue Variables: Massive Stars in Transition*, ed. A. Nota, & H. Lamers, *ASP Conf. Ser.*, 120, 368
- Reid, M. J. 1993, *ARA&A*, 31, 345
- Schmutz, W., Leitherer, C., & Gruenwald, R. 1992, *PASP*, 104, 1164
- Simons, D. A., Clark, C. C., Smith, S., et al. 1994, in *Instrumentation in Astronomy VIII*, *Proc. SPIE*, 2198, 185
- Tamblyn, P., Rieke, G. H., Close, L. M., et al. 1996, *ApJ*, 456, 206

Annexe B

Article « *New results on the Galactic Center Helium stars* »

Contribution pour la conférence *Galactic Center workshop 2002*, relative au travail sur les étoiles à hélium.

New results on the Galactic Center Helium stars

Thibaut Paumard¹, Jean-Pierre Maillard¹, and Susan Stolovy²

¹ Institut d'astrophysique de Paris (CNRS), 98b Bd. Arago, 75014 Paris, France

² SIRTf Science Center, CalTech, MS 220-6, Pasadena, CA 91125, USA

Received 15 November 2002, revised 30 November 2002, accepted 2 December 2002

Published online 3 December 2002

Key words infrared: stars, Galaxy: center, stars: early type, stars: Wolf-Rayet, instrumentation: spectrograph, techniques: radial velocities

PACS 04A25

The cluster of helium stars around Sgr A* has been re-observed with the BEAR spectro-imager on CFHT, in the 2.06 μm helium line, at a spectral resolution of 52 km s^{-1} and on a field of $\simeq 40''$. This new analysis confirms and completes a previous study at a spectral resolution of 74 km s^{-1} and on a smaller field of $24''$, corresponding to the central parsec (Paumard *et al.* 2001). Nineteen stars are confirmed as helium stars. These observations led to a clear differentiation between two groups of hot stars based on their emission linewidth, their magnitude and their positions relative to Sgr A*. The first class of 6 members is characterized by narrow-line profiles ($\text{FWHM} \simeq 200 \text{ km s}^{-1}$) and by their brightness. The other, fainter in K by an average of 2 mag, has a much broader emission component of width $\simeq 1,000 \text{ km s}^{-1}$. Several of the emission lines show a P Cygni profile. From these results, we propose that the narrow-line group is formed of stars in the LBV phase, while the broad-line group is formed of stars in or near the WR phase. The division into two groups is also shown by their spatial distribution, with the narrow-line stars in a compact central cluster (IRS 16) and the other group distributed at the periphery of the central cluster of hot stars. HST-NICMOS data in Pa α (1.87 μm) of the same field reveal a similar association. The identification of the Pa α counterpart to the He I stars provides an additional element to characterize the two groups. Bright Pa α emitters are found generally associated with the narrow-line class stars while the weak Pa α emitters are generally associated with the broad-line stars. A few particular cases are discussed. This confirms the different status of evolution of the two groups of massive, hot stars in the central cluster. As a by-product, about 20 additional candidate emission stars are detected in the central, high-resolution $19''$ field from the NICMOS data.

1 Findings from BEAR 97 He I 2.06 μm observation

With the BEAR spectro-imager, an imaging FTS (Maillard 2000) the central pc of the Galaxy was observed in 1997 at a spatial resolution of $0.5''$ and spectral resolution of 74 km s^{-1} in the He I 2.058 μm domain, covering a field of $24''$. The observation provided a homogeneous set of fully resolved line profiles. The spectro-imaging data were associated with Adaptive Optics data from CFHT in the K band (Lai *et al.* 1997) to check the possible confusion of sources. That particular study of the helium emission-line stars in the central parsec of the Galactic Center was published in Paumard *et al.* (2001). The main results can be summarized as follows:

1. 16 fully resolved P Cygni emission line profiles, cleaned of ISM emission, of purely stellar origin, were extracted.
2. they were found to divide into two distinct classes, with narrow ($\text{FWHM} \simeq 200 \text{ km s}^{-1}$) and broad-line profiles ($\text{FWHM} \simeq 1,000 \text{ km s}^{-1}$).
3. a difference in K of ~ 2 mag between the two classes was measured.
4. the spatial distribution of the two groups is different, with the narrow-line objects arranged in a central cluster, and the other class dispersed in a ring beyond a radius of $\simeq 0.3 \text{ pc}$ from Sgr A*.

From these findings it was concluded that the group of narrow-line stars can be considered as formed of stars in the LBV phase, and the other one of stars at the WR stage.

2 Observations

New BEAR data in He I $2.06\ \mu\text{m}$ were obtained in June 2000 at higher spectral resolution ($52\ \text{km s}^{-1}$). The field, composed of three overlapping circular sub-fields, was wider, and the signal-to-noise ratio higher by a factor of $\simeq 1.6$.

$\text{Pa}\alpha$ HST/NICMOS observations were taken in 1998 of the central parsec with Camera 1 (Stolovy *et al.* 1999) and of the central 4 pc with Cameras 2 and 3 (Scoville *et al.* 2003). Dithered Images were taken in filters F187N centered on the $1.87\ \mu\text{m}$ $\text{Pa}\alpha$ line and in F190N for the nearby continuum. By subtracting a suitably scaled F190N mosaic image from the F187N mosaic, a map of the stellar and interstellar $\text{Pa}\alpha$ emission can be obtained. Figure 3 shows the central region of the composite Camera 2 and Camera 3 $\text{Pa}\alpha$ image, for which the central $19'' \times 19''$ has a spatial resolution of $0.''18$.

3 He I stars and $\text{Pa}\alpha$ emission

With the new BEAR data, almost all the stars mentioned in Paumard *et al.* (2001) are confirmed, except the star numbered “N6”. The $\text{Pa}\alpha$ data show a bright, very small ISM feature and no stellar counterpart to this point-like He I emission. Four new broad-line stars are added. Two were out of the previously studied field, and the better signal-to-noise ratio is responsible for the other two new detections. The star “B5” was associated with IRS 13E. Maillard *et al.* (2003) have shown that there was indeed two emission line stars in the IRS 13E complex, namely IRS 13E2 and IRS 13E4. The broad line clearly detected in He I belongs to E2 only from Fabry-Perot imaging associated with adaptive optics by Clénet *et al.* (2003). The line profiles and locations of the 19 stars are shown in Fig. 1 and Fig. 2a. Fig. 2b clearly confirms that the narrow-line stars are generally much brighter in K than the broad-line stars. For B11, the signal-to-noise ratio is just sufficient to claim a detection, but not to derive reliable line parameters.

Fig. 3a shows that the He I stars are associated with the $\text{Pa}\alpha$ emission stars. The narrow-line stars (circles) are coincident with bright $\text{Pa}\alpha$ emitters (mean intensity $\simeq 2 \cdot 10^{-20}\ \text{W cm}^{-2}$ without taking into account IRS 34W, Table 1), whereas the broad-line stars correspond to fainter $\text{Pa}\alpha$ emitters (mean intensity $\simeq 0.97 \cdot 10^{-20}\ \text{W cm}^{-2}$). Other $\text{Pa}\alpha$ emitters are present, which may be also associated with He I emission, but too faint to have been detected with BEAR. A source extraction with the StarFinder procedure (Diolaiti *et al.* 2000) gives 52 point-like emission features in the high-resolution $19''$ central field, of which 43 are emission line stars with a high degree of certainty. The 9 other need further observation to rule out the possibility that these point sources are compact ISM features or incomplete continuum subtraction of stars. However, this result (Fig. 3b) is generally consistent with an independent analysis made by Scoville *et al.* (2003).

Table 1 Physical properties of the helium stars: K magnitude, full width at zero intensity (FWZI) of the $2.06\ \mu\text{m}$ He I line (km s^{-1}), $\text{Pa}\alpha$ line flux in units of $10^{-20}\ \text{W cm}^{-2}$, calibrated from $\text{Pa}\alpha$ emission in AF (Najarro *et al.* 1994). ID 180 is from the photometric list of Ott *et al.* (1999), He I N3 is from Paumard *et al.* (2001).

ID	Name	m_K	FWZI_{HeI}	$\phi_{\text{Pa}\alpha}$
N1	IRS 16NE	8.8	210	3.46
N2	IRS 16C	9.6	490	2.14
N3	IRS 16SW	9.4	520	2.09
N4	IRS 16NW	9.9	470	1.15
N5	IRS 33SE	9.9	460	1.12
N7	IRS 34W	11.8	500	0.14

ID	Name	m_K	FWZI_{HeI}	$\phi_{\text{Pa}\alpha}$
B1	ID 180	12.4	1,400	0.40
B2	IRS 7E2	12.2	1,500	0.28
B3	IRS 9W	11.8	1,900	0.83
B4	IRS 15SW	11.5	1,400	0.76
B5	IRS 13E2	11.0	1,300	2.27
B6	IRS 7W	12.0	1,600	0.44
B7	AF	10.6	1,200	4.40
B8	AFNW	11.5	1,800	1.05
B9	HeIN3	12.7	1,600	0.14
B10	BSD WC9	10.6	2,000	0.37
B11	IRS 29N	9.9	1,100	0.07
B12	IRS 15NE	11.2	1,500	0.37
B13	IRS 16SE2	11.8	940	1.15

4 Discussion

The central cluster of helium stars is confirmed with a total of 19 members currently identified. The various conclusions on the characteristics of these stars from the first paper, reviewed in the Introduction are confirmed: division into two groups from their linewidths (Fig. 1 and Fig. 2b), from their brightness and from their location (Fig. 2a). The difference of brightness (Fig. 2b) presents few exceptions which were already noticed in the first paper. One of the narrow-line stars (N7, IRS 34W) is weak and one of the broad-line stars (B11, IRS 29N) is brighter than the average of the other stars of the same group. From a long-term photometric study (Ott *et al.* 1999) IRS 34W is indicated as a variable star. It was weak at the time of our observations (Ott *et al.*, private communication).

It was proposed in Paumard *et al.* (2001) that the group of bright, helium stars was made of LBV-type stars. The high intensity of Pa α (Table 1), the variability of IRS 34W confirm that these stars are hot, mass-losing stars, still rich in hydrogen. On the contrary, the weakness of the Pa α emission combined with the very broad helium line are consistent with the other group being more evolved stars. A few sources are exceptions – IRS 13E2, AF, IRS 16SE2 – showing a broad-line He I profile, but strong Pa α emission. This apparent anomaly could certainly be due to the fact that the Pa α filter is not perfectly adapted to distinguish between rich and poor hydrogen emitters. Since the Pa α line is blended with another significant helium line, He I(4-3) at 1.869 μm , the intensity detected by the F187N can remain strong even if the hydrogen emission is intrinsically weak. Already mentioned, the weakness of the K magnitude of IRS 34W (Table 1) is due to the star being in a phase of enhanced intrinsic extinction. Naturally, the measured Pa α intensity is extremely weak, a factor 14 lower than the mean intensity. However, all these elements confirm the different status of evolution of the two groups of massive, hot stars in the central cluster. Assuming that all these stars were formed in the same star formation event, the differences in evolutionary state would come from the differences in their initial mass.

The Pa α data can help to address the question of whether the identification of emission line stars in the central region is complete or not. Possibly, about twenty new stars, associated with weak Pa α emission are detected in the central parsec (Fig. 3b). With only this indication, it cannot be concluded that they are more WR candidates. A deep, spectroscopic analysis using adaptive optics in the K band is needed. Besides more WRs, some of them could be Be stars, or could belong to the old star population as symbiotic or Mira-type stars in a phase of emission. At any rate, these data represent a new element in the census of spectral type in the central parsecs to better constrain the peculiar star formation conditions in this region of the Milky Way.

References

- Clénet, Y., *et al.*, 2003, *these proceedings*
 Diolaiti E., Bendinelli, O., Bonaccini, D., Close, L., Currie, D., & Parmeggiani, G., 2000, A&AS, 147, 335
 Lai, O., Véran, J.P., Rigaut, F., Rouan, D., Gigan, P., Lacombe, F., Lena, P., Arsenault, R., Salmon, D.A., Thomas, J., Crampton, D., Fletcher, J.M., Stilburn, J.R., Boyer, C., & Jagourel, P., 1997, In: *Optical Telescopes of Today and Tomorrow*, A.L. Ardeberg (ed), Proc. SPIE 2871, 859
 Maillard, J.P., 2000, In: *Imaging the Universe in 3 Dimensions*, E. van Breughel & J. Bland-Hawthorn (eds), ASP Conf. Serie 195, 185
 Maillard, J.P., Paumard, T., Stolovy, S.R., & Rigaut, F. 2003, *these proceedings*
 Najarro, F., Hillier, D.J., Kudritzki, R.P., Krabbe, A., Genzel, R., Lutz, D., Drapatz, S., & Geballe, T.R. 1994, A&A, 285, 573
 Ott, T., Eckart, A., & Genzel, R. 1999, ApJ, 523, 248
 Paumard, T., Maillard, J.P., Morris, M., & Rigaut, F. 2001, A&A, 366,466
 Scoville, N.Z., Stolovy, S.R., Rieke, M., Christopher, M., & Yusef-Zadeh, F. 2003, ApJ, *submitted*
 Stolovy, S.R., McCarthy, D.W., Melia, F., Rieke, G., Rieke, M.J., & Yusef-Zadeh, F., 1999, in *The Central Parsecs of the Galaxy*, ed. H. Falcke, A. Cotera, W.J. Duschl, F. Melia, M.J. Rieke, ASP Conf. Ser., 186, 39

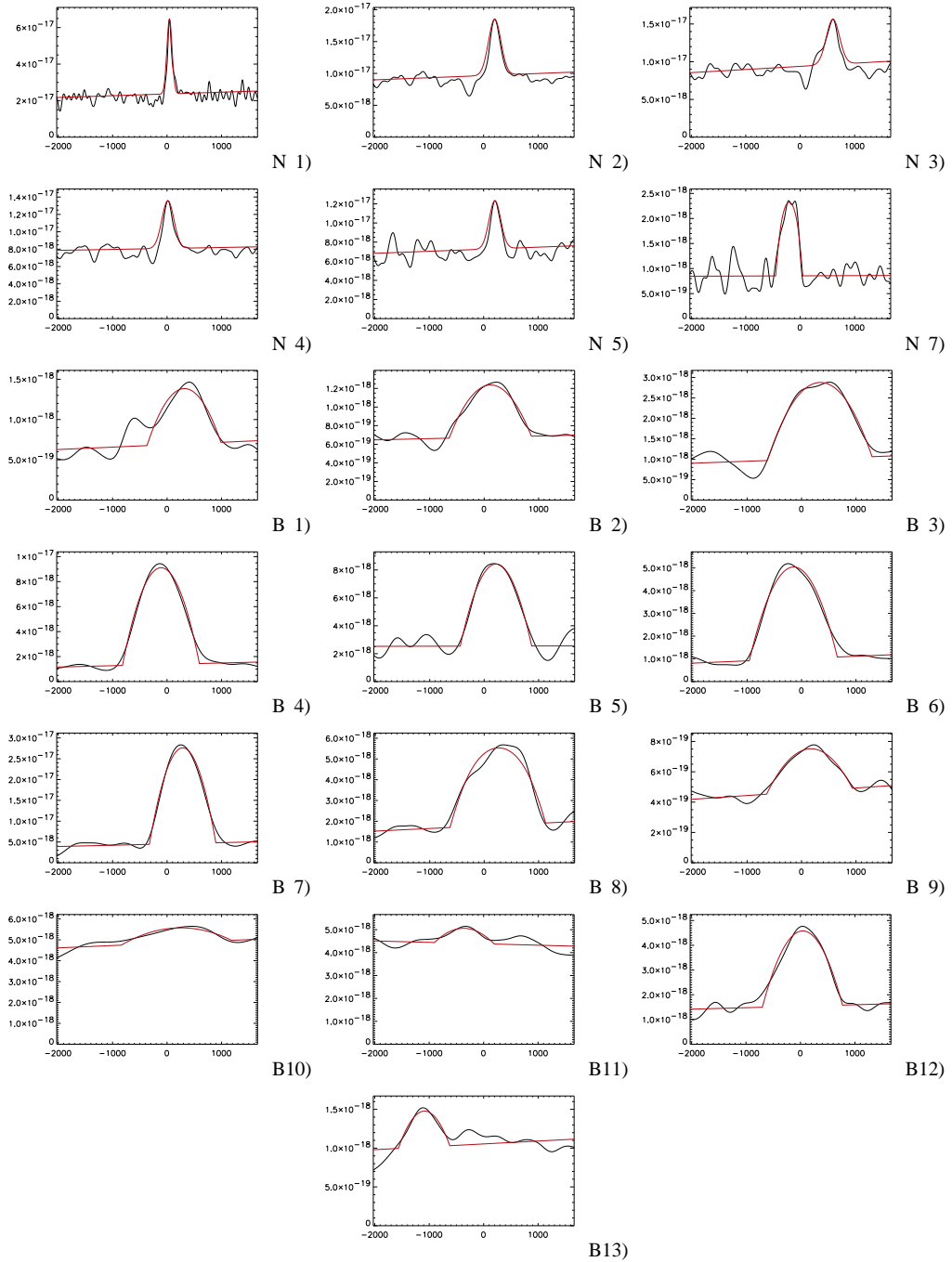


Fig. 1 Upper row, the $2.06\ \mu\text{m}$ He I narrow-line profiles; three lower rows, the broad-line profiles, all on the same velocity range of $-2,000$ to $+2,000\ \text{km s}^{-1}$. The intensities are in $\text{W m}^{-2}\ \text{cm}^{-1}$ (Continuum: a few 10^{-17} for N1–N5, a few 10^{-19} or 10^{-18} for the other stars). Simple line models are overplotted allowing to determine the full width at zero intensity.

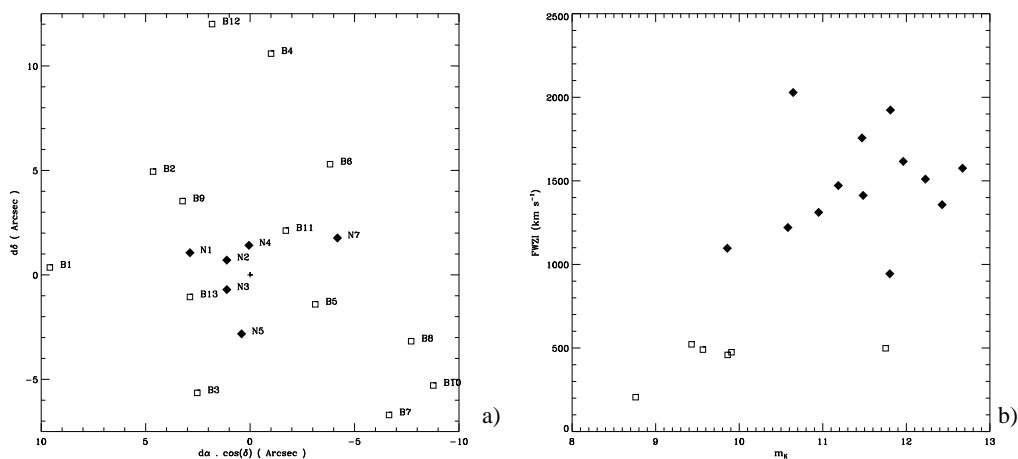


Fig. 2 a) Positioning of the helium stars, b) full width at zero intensity (FWZI) against K magnitude plot. The empty squares represent the broad-line stars, while the filled diamonds represent the narrow-line stars. On plot b), two regions can be seen: all the narrow-line stars, except IRS 34W – that is variable (see text) –, are grouped with a K magnitude brighter than 10, and all the broad-line stars, except one, have a K magnitude fainter than 10.5 (mean value $\simeq 12$).

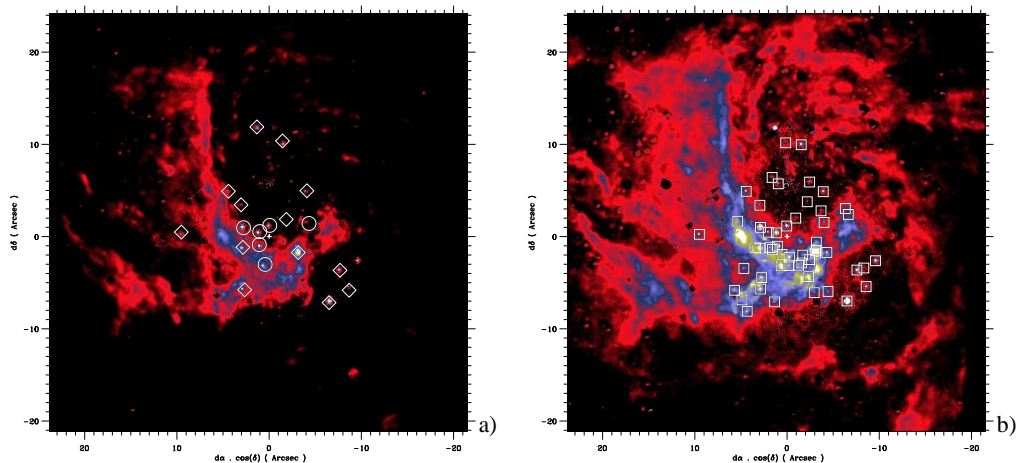


Fig. 3 a) $\text{Pa}\alpha$ map of the central 2 pc, with the inner $19''$ comprised of the high resolution Camera 2 data. Diamonds indicate the locations of the broad-line stars while the narrow-line stars are indicated by circles. All of these stars show emission in this $\text{Pa}\alpha$ filter. b) All emission line star candidates, in the central region, marked by square boxes. The intensity scale is stretched to show fainter emission.

Annexe C

Article « *The nature of the Galactic Center source IRS 13 revealed by high spatial resolution in the infrared* »

The nature of the Galactic Center source IRS 13 revealed by high spatial resolution in the infrared * **

J.P. Maillard¹, T. Paumard¹, S.R. Stolovy², and F. Rigaut³

¹ Institut d'Astrophysique de Paris (CNRS), 98b Blvd Arago, 75014 Paris, France

² SIRTf Science Center, CalTech, MS 220-6, Pasadena, CA 91125, USA

³ Gemini North Headquarter, Hilo, HI 96720, USA

Received 2003-07-30 / Accepted ??

Abstract. High spatial resolution, near-infrared observations of the bright Galactic Center source known historically as IRS 13, are presented. These observations include ground-based adaptive optics (AO) images in the H, Kp and L bands, HST-NICMOS observations in filters between 1.1 and 2.2 μm , and spectro-imaging data in the He I 2.06 μm , the Br γ and the He II 2.19 μm line. Analysis of all these data provides a completely new picture of the main component, IRS 13E, which appears as a complex of seven individual stars within a projected diameter of $\sim 0.5''$ (0.02 pc). The main sources, 13E1, 13E2, 13E3 which is detected as a binary, and 13E4, are all of different type. The star 13E1 is a luminous, blue object, with no detected emission line. 13E2 and 13E4 are two hot, high-mass, emission line stars, 13E2 being in the WR stage and 13E4 a giant O-type star. In contrast, 13E3A and B are extremely red objects. All these sources have a common westward proper motion (Ott *et al.* 2003). Two other sources, which become detectable only after deconvolution of the AO images in the H and Kp bands, are also present. One, that we call 13E5, is a red source similar to 13E3A and B, while the other one, 13E6, is probably a main sequence O star. The very red sources are proposed as other examples of dusty WR stars, like IRS 21 (Tanner *et al.* 2002). A diffuse halo around the cluster, seen prominently in the L band and in the lines of the ionized gas, is interpreted as a local accumulation of gas and dust by the expansion of the Mini-cavity, and by the excitation of the gas by the UV field of the IRS 13E sources. Considering this exceptional concentration of massive, hot stars, IRS 13E is proposed as the remaining core of a young star cluster, which would have been disrupted in the vicinity of SgrA*, and from which the helium stars, and maybe the other hot stars in the central parsec may originate. The detection of a discrete X-ray emission (Baganoff *et al.* 2003) at the IRS 13 position (within the positional accuracy) is examined in this context.

Key words. instrumentation: adaptive optics – instrumentation: NICMOS – infrared: stars – X-ray: source – Galaxy: Center – stars: Wolf-Rayet

1. Introduction

In the early images of the central region of the GC recorded in the near infrared, at the best seeing-limited resolution, several bright point sources dominate the $\sim 20'' \times 20''$ field centered on SgrA*. With the radical improvement of angular resolution through multiple short exposures with shift-and-add (SHARP camera, Eckart *et*

al. 1995) or speckle techniques (Ghez *et al.* 1999), with the images from the NICMOS cameras on board HST (Stolovy *et al.* 1999), to the advent of adaptive optics correctors behind large telescopes as NAOS (Ott *et al.* 2003), a more complex vision of this crowded field has emerged. At a spatial resolution in the best case of 0.05'' (Ghez *et al.* 1999) new, faint stellar sources appear and the early-identified sources are often resolved into several components. Therefore, the observed spectra, generally made at a resolution limited at best by a slit not less than 1'' wide, are actually composites of emission from stellar objects of different spectral type as well as from emission lines from the surrounding interstellar medium (ISM). The stellar type identified from these spectra can be wrong if attributed to a single source, which can erroneously look unusual. This care led to the paper on the revised identifications of the central cluster of He I stars by

Send offprint requests to: J.P. Maillard

* This paper is based on observations obtained with the Adaptive Optics System Hokupa'a/Quirc, developed and operated by the University of Hawaii Adaptive Optics Group, with support from the National Science Foundation,

** on observations obtained with the Canada-France-Hawaii Telescope, operated by the National Research Council of Canada, le Centre National de la Recherche Scientifique de France and the University of Hawaii

Correspondence to: maillard@iap.fr

Paumard *et al.* (2001) made from slitless spectro-imaging, with BEAR an imaging Fourier Transform Spectrometer (Maillard 2000). This instrument makes it possible to obtain near-infrared spectroscopy at the seeing-limited resolution of Mauna Kea (i.e. $\simeq 0.5''$), which represents a significant improvement. However, this resolution is not sufficient for such a crowded field. Therefore, the data were compared to adaptive optics (AO) images in the K band of the same field, with a spatial resolution of $\sim 0.15''$, in order to check whether the emission sources at the angular resolution of seeing were single stars or not.

Among the sources studied in this paper the object historically named IRS 13, located approximately $3.6''$ southwest of SgrA*, is a typical example. In early works a bright spot is reported there at all near-infrared wavelengths, in J, H, K (Rieke *et al.* 1989) and L (Allen & Sanders 1986). However, from a discussion on the sources of energy at the Galactic Center, Rieke *et al.* (1989) note “there are separate luminosity sources in the core of the $10 \mu\text{m}$ sources 1, 9 and 13”, because, particularly for IRS 13, the energy distribution from 1 to $5 \mu\text{m}$ presents a sudden, steep increase beyond $3 \mu\text{m}$. A first work at subarcsecond resolution, by lunar occultation in the K band (Simon *et al.* 1990) indicates that IRS 13 resolves into a pair of sources, separated by $\sim 1.2''$, which were henceforth designated as IRS 13E and 13W. The former was reported as the brightest source in K with K_{mag} equal to 9.4 and 13W one magnitude fainter. In the photometric survey of Ott *et al.* (1999) from SHARP imaging data (Eckart *et al.* 1995), at a limit of resolution of $\sim 0.15''$ after deconvolution, two equally bright components of 13E ($K_{mag} = 10.26$) are reported, IRS 13E1 and 13E2, with a separation of $0.2''$. Paumard *et al.* (2001) published the first AO map of IRS 13E in the K band, extracted from a larger image of the central region obtained with the CFHT-AO system (Lai *et al.* 1997). We noted that a fainter third source, we called IRS 13E3, was also present, forming a kind of equilateral triangle with 13E1 and 13E2. In parallel, Clénet *et al.* (2001) published a complete photometric analysis of the same data. For IRS 13E they reported three components in the K band, they noted 13E1, 13E2 and 13N. From the given offset coordinates the source called 13N in this paper is not exactly coincident with the source we had previously called 13E3 (Paumard *et al.* 2001).

In the meantime, spectroscopic works on the stellar population of the central parsec were conducted. Several spectra of IRS 13 (Blum *et al.* 1995, Libonate *et al.* 1995, Tamblyn *et al.* 1996), and specifically of IRS 13E (Genzel *et al.* 1996), and of IRS 13W (Krabbe *et al.* 1995) have been published. They cover mostly the K band, i.e. all or part of the $1.95 - 2.45 \mu\text{m}$ range, and one the $1.57 - 1.75 \mu\text{m}$ region in the H band (Libonate *et al.* 1995). From these spectra IRS 13W is unambiguously a cool star with the strong vib-rot CO signatures at $2.3 \mu\text{m}$ (Krabbe *et al.* 1995). Emission lines were detected in IRS 13E, typical of a luminous, hot star: strong He I 2.058, $2.112 \mu\text{m}$, Br γ line and other Brackett lines up to Br12, plus weaker lines of [Fe II], [Fe III], and a weak emission

at $2.19 \mu\text{m}$ attributed to He II. From these spectral characteristics Libonate *et al.* (1995) concluded “the IRS 13 spectrum bears a strong resemblance to the low-resolution K-band spectra of P Cygni (an LBV) and the AF source”. However, from the extraction of the He I $2.058 \mu\text{m}$ line profile at high spectral resolution from the BEAR data, Paumard *et al.* (2001) concluded that one of the three sources identified as forming IRS 13E instead of a LBV-type star should be a helium star at the WR stage. The main argument was the width of the observed emission line profile (FWHM $\simeq 974 \text{ km s}^{-1}$), making the source belong to the class of broad-line stars including 8 other stars with comparable linewidth in the central cluster of helium stars. The next step was to try to identify which one of the 3 sources at IRS 13E was the helium star. It was measured from the other broad-line stars that they are also characteristically weaker, in average by $\simeq 2.4$ mag, in the K band than the other helium sources with narrow emission line. With IRS 13E3 the fainter source in K and a K_{mag} equal to the magnitude measured for the other broad-line stars we concluded that IRS 13E3 and should be the helium emitter of WR-type. IRS 13E1 and IRS 13E2 were too bright and should be of a different type, without being able to precise their stellar type. Actually, we will show in this paper that the final solution is more complex.

In the centimetric domain, Zhao and Goss (1998) presented the detection of IRS 13 at 7 and 13 mm with the VLA, at a resolution of $0.06''$, which they reported to be the brightest radio continuum source after SgrA* at the Galactic Center. They resolved the source into two components, one with no significant proper motion while the other one is moving south at a rate $6.2 \pm 1.1 \text{ mas yr}^{-1}$. They called the two compact H II regions IRS 13E and IRS 13W, which was improper, since these denominations had been already given to infrared sources at IRS 13 as reminded above, with which they are not coincident. However, this detection is another element which makes IRS 13 special.

The detection of a bright, discrete X-ray emission source (Baganoff *et al.* 2003, Munro *et al.* 2003) at the IRS 13 position within the positional accuracy – source CXOGC J174539.7-290029 – among the brightest sources within the central parsec besides SgrA*, is a last element contributing to make this source an object of interest. This coincidence already triggered the interest of Coker *et al.* (2002) who presented the first Chandra X-ray spectrum of IRS 13 and deduced that it was consistent with a highly absorbed X-ray binary system. They concluded that IRS 13E2 was a compact post-LBV binary whose colliding winds were the source of the X-ray emission.

As a conclusion, the origin of the brightness of IRS 13 from X-ray to cm-wave is a matter of debate. As one of the brightest objects at all wavelengths in the vicinity of SgrA* it deserves a special attention. We examined all the high-angular resolution images in the near infrared currently available. This analysis made it possible to build a precise and completely new picture of IRS 13 which is pre-

sented in this paper. We will show that the peculiar spectral energy distribution (SED) previously reported is well explained by the nature of the individual sources which compose IRS 13. This structure has direct consequences for the interpretation of the X-ray source, as well as possible implications for the origin of the exceptional population of massive stars in the central parsec of the Galaxy to which this complex belongs.

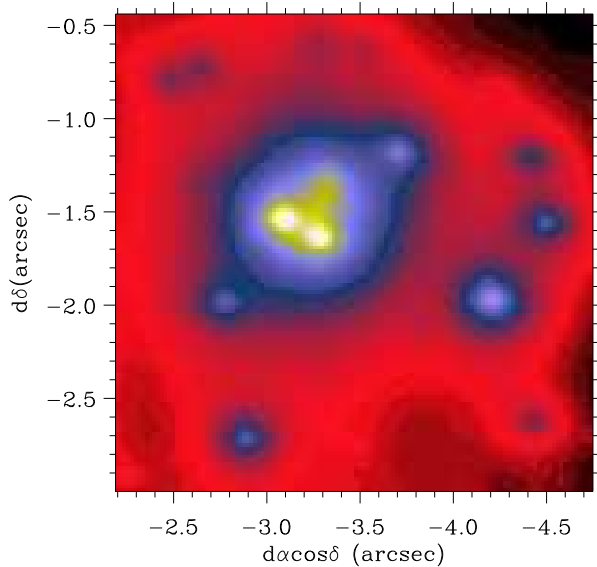


Fig. 1. Field of $2.5'' \times 2.5''$ ($0.1 \text{ pc} \times 0.1 \text{ pc}$) around IRS 13E from the Gemini AO image in the Kp band. IRS 13E is the central, compact group of stars and IRS 13W the brightest source $\sim 1''$ southwest of IRS 13E. The coordinates are in arcsec offset from SgrA*.

2. High-angular resolution images of IRS 13 and data reduction

Ground-based AO data from several telescopes and space-based NICMOS data, all containing IRS 13 in their field, have been gathered. The origins and the bandpasses of each data file are displayed in Table 1.

2.1. Adaptive Optics data

We have analyzed data from three different AO systems: PUEO/CFHT (Lai *et al.* 1997), Hokupa'a/Gemini North (Graves *et al.* 1998), and Adonis/ESO 3.6-m telescope (Beuzit *et al.* 1997). The CFHT data, in the K band, were obtained on 26 June, 1998. They were already presented and analyzed in detail in Paumard *et al.* (2001). The total field covers $40'' \times 40''$ centered on SgrA*. The FWHM of the Point Spread Function (PSF) varies from $0.13''$ to

$0.20''$ in the field since PUEO has a visible wavefront sensor, requiring to use a V $\simeq 14$ star $20''$ to the north-east of the field center. The L-band data were obtained with the ADONIS visible wavefront sensor in 2000, from 20 to 22 May, on the ESO 3.6-m telescope. These data are described in Clénet *et al.* (2001). The final L band image we used has a FWHM of $0.291''$ and covers a field of $\simeq 13'' \times 13''$ centered on SgrA*. The Gemini North data were part of the AO demonstration run conducted by F. Rigaut on the Galactic Center in July 2000. The data were obtained with the Hokupa'a AO system and the QUIRC camera (Graves *et al.* 1998) in the Kp and the H band (Table 1) respectively 3 and 6 July in field 1, centered on SgrA*. The field coverage of each image is $20'' \times 20''$. For the H image the FWHM of the PSF varies from $0.115''$ to $0.19''$ and for the Kp image from $0.12''$ to $0.18''$. In the vicinity of IRS 13 the measured FWHM is respectively $0.180''$ and $0.172''$. The portion of the AO images in the Kp filter analyzed in the paper is shown in Fig. 1.

2.2. NICMOS data

Six filters, coded F110M, F145M, F160W, F187N, F190N, and F222M were used in observing the stars in the inner parsec of the Galactic Center with the NICMOS cameras on board HST, as part of three independent Galactic Center programs (7214, 7225, and 7842). These data were taken between Aug. 1997 and Aug. 1998. The filter properties (central wavelength, bandwidth, zero-magnitude flux, pixel size) and the data processing of the raw data are described in Rieke (1999) and Stolovy *et al.* (1999). Although each program covered a larger region, we extracted a small portion of $\simeq 4'' \times 4''$ centered on IRS 13E of the image from each filter. All these diffraction-limited images were particularly useful to derive the SED of the stellar components of IRS 13 and its environment.

Apart from wide (W) or medium (M) bandpass filters, F187N is a 1% narrow-band filter centered on the Pa α line. By subtraction of F190N, a comparable narrow-band filter in the nearby continuum, the distribution of the ionized gas in the inner parsec was obtained (Stolovy *et al.* 1999). In this map are also positive stellar residual emission which must come from Pa α emission in the atmosphere of the hot stars. We used a best-fit scale factor between F187N and F190N in order to minimize both positive and negative stellar residuals of the stars in the central parsec. Negative residuals can arise in stars with Pa α absorption and/or in stars with local excess extinction along the line of sight. For this paper, we identify emission line stars as those with very significant F187N/F190N ratios (exceeding 1.2). The resulting Pa α image was essential in determining which of the individual stars in the IRS 13 complex was an emission line star.

2.3. Data reduction

The initial processing of each dataset is not described here. It can be found in the papers cited with the presentation of

Table 1. Instruments, filters, bandpasses and year of data acquisition of the high-resolution images of the IRS 13 field

Filter	Instrument / Telescope	λ /FWHM (μm)	year
F110M	NICMOS/HST	1.10/0.200	97-98
F145M	NICMOS/HST	1.45/0.197	97-98
F160W	NICMOS/HST	1.60/0.400	97-98
H	Hokupa'a+Quirc/Gemini N	1.65/0.296	2000
Pa α	NICMOS/HST	1.87/0.019	97-98
F190N	NICMOS/HST	1.90/0.017	97-98
Kp	Hokupa'a+Quirc/Gemini N	2.12/0.410	2000
K	PUEO+KIR/CFHT	2.20/0.340	1998
F222M	NICMOS/HST	2.22/0.143	97-98
L	ADONIS+COMIC/3.6m ESO	3.48/0.590	2000

each of them. Below are listed the main operations which were performed subsequently to the initial data reduction.

2.3.1. Calibration

All the NICMOS data were calibrated in μJy as described by M. Rieke (1999). The calibration of the sources in the L band was based on the calibration of IRS 13W made by Clénet *et al.* (2001), a prominent, isolated source. Remained the Gemini data in the H and the Kp filters which had been processed but were not calibrated. In order to minimize photometric uncertainties between data from various origin we calibrated the Gemini AO data by linear interpolation from the NICMOS data. Based on few bright, isolated stars, we used for each Gemini filter the two closest NICMOS filters, at shorter and longer central wavelength. Taking into account the filter bandpasses, interpolation was made between the F160W and F190N photometry for the H band, F190N and F222M for the Kp band.

2.3.2. Star detection

To perform the extraction of the individual stars in the IRS 13 field from the AO and NICMOS data, *StarFinder*, an IDL procedure (Diolaiti *et al.* 2000) specially written for AO data, was first used. The preliminary operation consists of building a good PSF by averaging several isolated and bright enough stars in each image. By adjusting the PSF to the local peaks in the field the exact peak positions are retrieved with the photometry of the corresponding stars. The procedure makes also possible to artificially subtract out one or several stars in the field to see more clearly the remaining sources (see Sect 3.7).

2.3.3. Deconvolution

The image residuals left by applying the *StarFinder* procedure led us to suspect that more sources might be present in the IRS 13 complex, which could not be detected because being too close for the resolution. To pos-

sibly improve the star detection we applied a new deconvolution code called MCS (Magain *et al.* 1998). Contrary to the *StarFinder* procedure, the MCS program uses an analytical PSF (a Moffat-type function). The final PSF is chosen prior to deconvolution, with a width compatible with the original image sampling. Thus, the final PSF can be narrower than the observed one without violating the Shannon sampling theorem. The contribution of a diffuse background is also matched to the image with an adjustable smoothing. The sampling was high enough for the Gemini AO images, in the H and the Kp bands, to provide a substantial gain in resolution. Because of the sampling of the L-band image a more limited gain was obtained for this image, which was useful anyway. For the H and the Kp images the width of the synthetic PSF is equal to $0.040''$ and to $0.192''$ for the L-band image, i.e. a gain in resolution respectively of a factor 4.5 in H, 4.3 in Kp and 1.5 in L. However, this method applied to the IRS 13 images demanded many trials to reach a stable and plausible solution because of the presence of a non uniform background in which the sources are embedded. The convergence was helped by the comparison between the solutions for the H and Kp filters. The two filters are almost adjacent which makes pertinent the detection in both filters, even for very red or very blue objects. This code was not applied to the CFHT K-band nor to the NICMOS images, which PSF both show significant secondary rings, because these are not correctly handled by this code, written for seeing-limited images.

2.3.4. Proper motions

Determination of proper motions would be very useful to conclude whether the members of the IRS 13 complex were bounded or not. Two AO images were at our disposal, taken exactly two years apart, respectively on CFHT (July 1998) and Gemini (July 2000). Deriving meaningful proper motions supposes to be able to estimate star positions at a precision approaching 1 mas, i.e. one twentieth of a pixel, given that a motion of 1 mas for two years corresponds to a velocity of $\sim 20 \text{ km s}^{-1}$. With such a limited time difference and between two different AO systems, the uncertainties on the proper motions appeared comparable to the amplitude of the proper motions we could derive. Finally, we obtained from Ott *et al.* (2003), who had conducted a new analysis of ten years of SHARP data, providing more than 1000 proper motions in the central parsec, the proper motions of the main components of IRS 13 and of its nearby field.

2.4. BEAR data

Even though the BEAR spectro-imagery data are not at the spatial resolution of the NICMOS and AO data, the Br γ and $2.06 \mu\text{m}$ He I line profile at IRS 13E were used as complementary information to help determine the spectral type of the underlying stars. The IRS 13 complex

is located in a region of interstellar emission, intense in Br γ (Morris and Maillard 2000, Paumard *et al.* 2003a) as well as in the 2.06 μm helium line (Paumard *et al.* 2001). Hence, the line profiles had to be corrected to remove the ISM contribution, made here of two main velocity components (Fig. 7 - central panel), superimposed on the stellar profile. This operation was particularly delicate for the Br γ profile since the ISM emission is as intense as the stellar profile. Only the high resolution (21.3 km s $^{-1}$) made it possible to separate, with some approximation anyway, the stellar from the interstellar contribution.

Other BEAR data obtained in 2000, 10 June of the central parsec, through a narrow-band filter (4500 – 4650 cm $^{-1}$) centered on the 4568.1 cm $^{-1}$ (2.19 μm) He II line, have also been used. After the standard BEAR data processing and subtraction of the continuum, the emission spectrum of IRS 13E in this range, at the initial resolution of 70 km s $^{-1}$, was extracted from the spectral cube. A smoothing function was applied to obtain the broad line profiles with a higher S/N ratio.

3. Results

From the 8 high-resolution images between 1.1 and 3.5 μm (Table 1) and the spectroscopic data available, the following results on the IRS 13 complex and its environment have been obtained:

3.1. Star detection

The final result of the star detection in the 8 filters is presented in Table 2. The stars listed are those detected both in H and Kp after deconvolution of the Gemini data. By requiring the sources to be detected in both bands, we intend to avoid contamination by deconvolution artifacts. In the other hand, a few sources, detectable only in one band can be missed.

The resulting Kp-band deconvolved image is shown on Fig. 2. Twenty sources in total are detected in this small field, which are identified on Fig. 3. Then, all these sources were searched for with *StarFinder* for the filters where the deconvolution operation could not be applied, and with the MCS code (Magain *et al.* 1998) in the L band. Empty positions in Table 2 indicate that the source is not detectable in a specific filter. An upper limit is given at some positions for the extreme filters (1.1 μm and L) where the detection is the most difficult. This limit is not uniform in the field depending on the proximity of another bright source, particularly in L.

In conclusion, the IRS 13E source is resolved into a compact cluster of at least 7 objects encircled within $\simeq 0.5''$ (Fig. 2). The two brightest sources, 13E1 and 13E2, had already been identified in Ott *et al.* (1999) and in Paumard *et al.* (2001). The one we had noted 13E3 appears double after deconvolution. Thus, we call the two components 13E3A and 13E3B. By continuity, the closest bright source north of 13E3 is called 13E4. Two other sources revealed by deconvolution are called 13E5 and

Table 2. Photometric measurements between 1.1 and 3.5 μm , in log(μJy), of the stars detected by deconvolution (MCS) of the 2.5'' \times 2.5'' IRS 13 field from the Gemini AO images, in the H and the Kp filters, and by *StarFinder* for the NICMOS filters (F). The sources are listed by order of decreasing brightness in the Kp band, except IRS 13W, which is listed first. Values preceded by < are upper limits.

ID	F110M	F145M	F160W	H	F190N	Kp	F222M	L
W	<0.56	2.58	3.28	3.20	3.96	4.27	4.36	4.89
E1	1.76	3.40	3.82	3.93	4.27	4.40	4.49	5.03
E2	1.61	3.22	3.71	3.80	4.17	4.38	4.48	5.37
E4	0.93	2.68	3.17	3.28	3.69	4.11	4.18	<4.66
5	0.78	2.66	3.20	3.30	3.72	4.04	3.93	
6	0.39	2.51	3.07	3.14	3.57	3.94	3.89	
7	1.23	2.78	3.20	3.26	3.63	3.92	3.88	
8	0.62	2.55	3.08	3.08	3.53	3.90	3.81	
E3A	<0.45		2.29	2.43	3.11	3.81		5.46
10	0.11	1.88	2.63	2.81	3.23	3.68	3.55	
E3B	<0.45			2.24		3.57		5.29
12	0.69	1.98	2.62	2.66	3.15	3.48	3.45	
13	-0.09	2.02	2.58	2.65	3.14	3.46	3.40	
14	-0.16	2.01	2.55	2.65	3.11	3.43	3.34	
15	-0.06	1.75	2.25	2.37	2.82	3.12	3.23	
16		1.57	2.18	2.36	2.71	3.11	2.92	
E5	<-0.17	1.60		1.75	2.72	3.08	3.61	5.07
18	0.56	1.87	2.27	2.30	2.74	2.99	3.02	
E6	<0.48		2.46	2.53		2.97		<4.68
20	0.86	1.42	2.01	2.11	2.57	2.88	2.89	

13E6. They are very close to the triangle made by 13E1, 13E2 and 13E4 and then, seem to belong to the cluster as well, as is examined below.

3.2. Astrometry

The positions of the sources in the 2.5'' \times 2.5'' IRS 13 field in offsets from SgrA* are given in Table 3. The astrometry was retrieved from the results of the deconvolution of the portion of the Gemini Kp-band image. The precision of the positions in the deconvolved image depends on the brightness of the sources. For the brightest sources the relative 1- σ position error is equal to 1.0 mas. From these positions the projected angular separations between the main IRS 13E components are given in Table 3.2, translated to AU, by taking a distance to the GC of 8 kpc (Reid 1993). All the sources of the small field are detected by the reprocessing of the SHARP data (Ott *et al.* 2003), except that a single source is given for E3A and E3B (#118) and E6 is not detected. The Table 3 offsets are estimated from the positions of isolated stars around IRS 13E published by Ott *et al.* (1999) which, in this paper are given relative to IRS 7, to which the offset from SgrA* is added taken from Menten *et al.* (1997). The identification of the sources is presented on Fig. 3.

We used this astrometry to examine the position of the X-ray source CXOGC J174539.7-290029 whose IRS 13

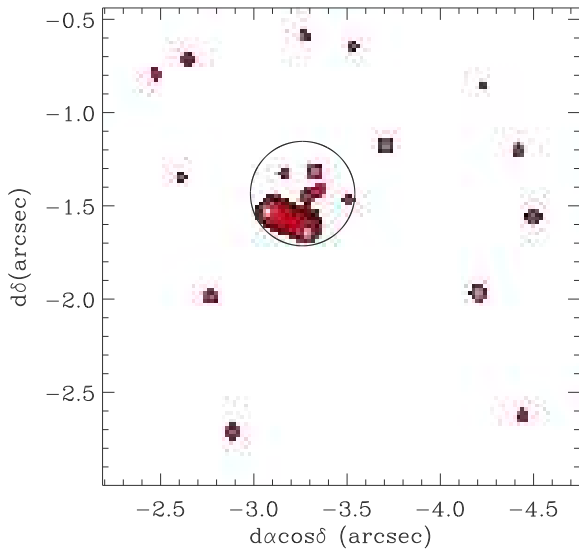


Fig. 2. Deconvolved image by the MCS code (see text) of the Fig. 1 field in the Kp filter. The circle of $0.5''$ diameter represents the original IRS 13E source. A diffuse, asymmetrical halo is detected in this band and in the H band around the two brightest sources of the complex.

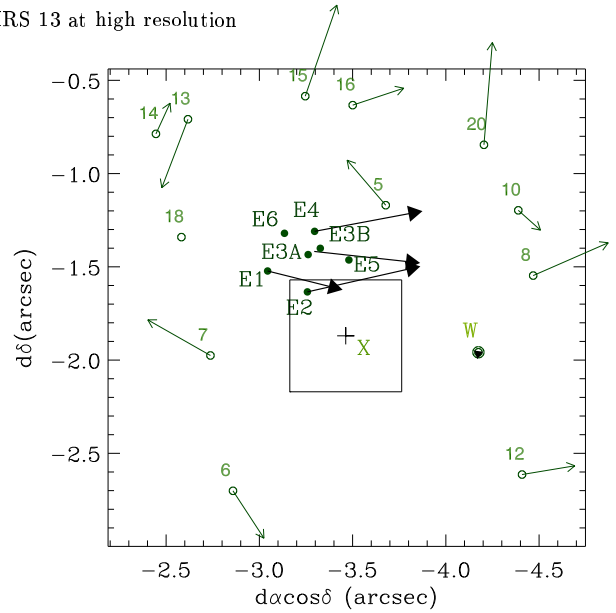


Fig. 3. The Fig. 2 field with the star identification. The vector associated with most of the stars represents the amplitude in velocity (e.g. Table 6) and the direction of proper motion measured from SHARP data by Ott *et al.* (2003). For E3A and E3B, only the barycenter proper motion is determined. The cross marked X represents the nominal position of the X-ray source at the center of an error box of $\pm 0.3''$.

is proposed as the optical counterpart by Baganoff *et al.* (2003). The position was placed on Fig. 3 by measuring the offset of the source with respect to the X-ray source at SgrA*, from the coordinates of both sources reported in Baganoff *et al.*. The resulting position falls outside the center of IRS 13E, exactly $0.29''$ southwest of the closest star, IRS 13E2. The $1-\sigma$ error reported on the coordinates of each X-ray source is of $\pm 0.2''$ in right ascension and $\pm 0.1''$ in declination. By combining the astrometric uncertainties on the two sources position we drew a minimum error box of $\pm 0.3''$ around the nominal position. IRS 13E2 falls in this box.

3.3. Photometry

Table 2 can be used to derive the standard photometry in H, K, and L bands and the color indices of all the sources identified in Fig. 3. The Kp filter, (Table 1) which is close and has a width comparable to K, was used and is referred to as K in the subsequent analysis. The results are presented in Table 5.

3.4. Proper motions

From the results communicated by Ott *et al.* (2003), the direction and amplitude of the proper motions for the main IRS 13E sources and most of the stars in the $2.5''$ field are represented in Fig. 3. Note that the five sources, 13E1, 13E2, 13E3A, 13E3B (proper motion is only given

Table 3. Offsets from SgrA* of the sources shown on Fig. 3.

ID	ID ^a	$\Delta\alpha\cos\delta('')$	$\Delta\delta('')$
W	40	-4.17	-1.96
E1	25	-3.02	-1.58
E2	27	-3.24	-1.68
E4	77	-3.26	-1.35
5	69	-3.64	-1.20
6	101	-2.90	-2.77
7	114	-2.74	-2.05
8	120	-4.45	-1.53
E3A	118	-3.24	-1.48
10	145	-4.35	-1.19
E3B	118	-3.30	-1.44
12	188	-4.44	-2.60
13	296	-2.56	-0.79
14	295	-2.39	-0.88
15	328	-3.18	-0.63
16	381	-3.44	-0.67
E5	780	-3.46	-1.50
18	902	-2.55	-1.42
E6		-3.10	-1.37
20	459	-4.15	-0.85
X		-3.46	-1.87

^a : identification number from Ott *et al.* (2003)

Table 4. Projected separation of the main IRS 13E sources

Sources	Ang. sep.	Distance (AU)
E1 – E2	0.241''	1921
E1 – E4	0.330''	2629
E2 – E4	0.327''	2607
E2 – E3A	0.200''	1594
E3A – E3B	0.073''	587

Table 5. H, K and L photometry of the IRS 13E cluster and the nearby field stars from Table 2

ID	<i>H</i>	<i>K</i>	<i>L</i>	<i>H</i> – <i>K</i>	<i>K</i> – <i>L</i>
W	14.55	11.30	8.92	3.25	2.38
E1	12.74	10.98	8.59	1.76	2.39
E2	13.05	11.03	7.73	2.02	3.30
E4	14.37	11.72		2.65	
5	14.32	11.90		2.42	
6	14.71	12.13		2.58	
7	14.41	12.18		2.23	
8	14.86	12.23		2.63	
E3A	16.48	12.47	7.50	4.01	4.97
10	15.55	12.80		2.75	
E3B	16.95	13.07	7.92	3.90	5.14
12	15.92	13.28		2.65	
13	15.95	13.35		2.60	
14	15.95	13.42		2.53	
15	16.65	14.20		2.45	
16	16.66	14.22		2.44	
E5	18.19	14.28	8.48	3.90	5.79
18	16.79	14.52		2.29	
E6	16.24	14.56		1.68	
20	17.29	14.78		2.52	

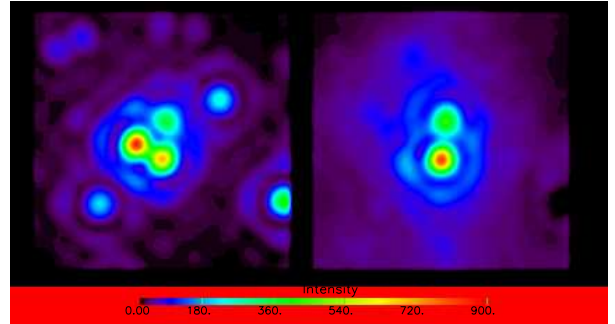
for the barycenter of 13E3A and B) and 13E4 are all moving West, with a similar velocity, while all the nearby stars have very different directions and amplitudes. The amplitude of the proper motions of the four main sources, in angular motion per year (for a GC distance of 8 kpc) and in velocity, are presented in Table 6. The *rms* uncertainty on 13E3 proper motion is the largest one, because of the difficulty of measuring accurate positions from several epochs of SHARP data for a weak source so close to much brighter sources, 13E2 and 13E4. The error becomes large for data recorded with poor seeing conditions.

Table 6. Amplitude of proper motions of the main IRS 13E sources (from Ott *et al.* 2003).

Name	mas/yr	km/s
13E1	5.50	207 ±14
13E2	8.20	310 ±19
13E3	7.54	285 ±270
13E4	7.77	294 ±32

3.5. The stellar Pa α emission line

As shown on Fig. 4, only two of the IRS 13E components, IRS 13E2 and 13E4, remain after subtraction of the F190N continuum from the F187N filter which contains Pa α . These two stars are unambiguously emission line objects, with the integrated line intensity at IRS 13E2 brighter by a factor 2.35 ± 0.1 than at IRS 13E4.

**Fig. 4.** At left, NICMOS image of IRS 13E, in the Pa α 1.87 μ m filter, and at right, difference between this image and the suitably scaled nearby continuum at 1.90 μ m. IRS 13E2 and IRS 13E4 appear as emission line stars.

3.6. The ionized gas

The interstellar, ionized gas is tracing in the central parsec the HII region called object SgrA West or commonly the Mini-spiral. The gas appears strongly enhanced in the Br γ line in the vicinity of IRS 13E, as seen in Fig. 5. This image is extracted from the detailed, kinematic analysis of the Br γ emission of the gas from the BEAR data made by Paumard *et al.* (2003a) by a multi-component analysis of the line profiles on most of the SgrA West field. Individual velocity structures have been identified. Fig. 5 is a reconstructed image of purely the interstellar gas, as it results from the summation of all the intensity maps of the detected structures. The IRS 13E complex is located just at the northern end of the western edge of a particular structure of the ionized gas called the Mini-cavity. This structure is marked by the bright, perfectly circular wall seen in this image, open toward SgrA*, and more sharply seen in the full Pa α NICMOS data (Stolovy *et al.* 1999). In this latter paper is proposed that the bubble-like feature was created by the wind from a star identified by a weak Pa α point source located very near the geometric center of the Mini-cavity. A proper motion of the edge of the Mini-cavity of $\sim 200 \text{ km s}^{-1}$ is measured by Zhao & Goss (1998). In Paumard *et al.* (2003a), it is shown that the Mini-cavity is embedded inside a non-planar velocity structure of the gas, called the Northern Arm, which is more spatially extended than the streamer classically called by this name. More precisely the Mini-cavity is located in the flow fitted by Keplerian orbits of the gas,

with SgrA* as focus, which have mainly a east-west motion. Another velocity structure is identified, stretched at 45° toward northwest (Fig. 5, called the Bar, thus roughly perpendicular to the bright edge of the Northern Arm. On the line of sight of IRS 13E these two velocity structures produce the two main components in the line profile of the ionized gas shown on Fig. 7 (central panel). The fastest component at -250 km s^{-1} is due to the motion of the gas perturbed by the Mini-cavity, the slowest component, at -39 km s^{-1} , to the Bar. On a morphological basis IRS 13E seems to belong to the bright arc (Fig. 5 of the gas shocked at the edge of the Mini-cavity. On the intensity map of the Bar, a small region centered on the IRS 13E position appears locally enhanced. Therefore, the observed brightness of the ionized gas around the position of IRS 13E is due to the addition of two contributions on the line of sight, the edge of the Mini-cavity and the gas, locally excited gas of another flow, the Bar. The source of excitation is likely the ionizing flux from the IRS 13E sources. We infer that the IRS13E complex should not be located inside the edge of the Mini-cavity, but close to or inside the Bar, which lays behind the Mini-cavity (Paumard *et al.* 2003a).

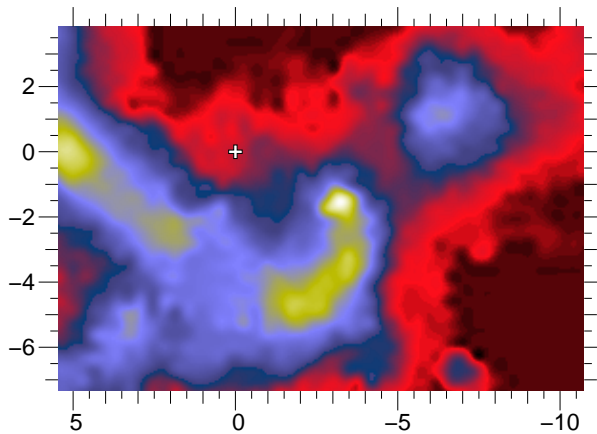


Fig. 5. Reconstructed image of a portion of SgrA West in the $\text{Br}\gamma$ emission line (see text) showing the structure of the Mini-cavity. The brightest spot in the ionized gas at the western edge of the Mini-cavity corresponds to the location of IRS 13E. The cross marks the position of SgrA*. The coordinates are δ and $\alpha\cos\delta$ in arcsec, in offset from SgrA*.

3.7. The diffuse component in the L band

The AO image in the L band shows a diffuse emission around the bright nucleus. This emission is only due to continuum emission since the strong $\text{Br}\alpha$ line from the ionized gas falls outside the filter bandpass. The deconvolution process after subtraction of the star leaves this background component shown on Fig. 6. It can be noticed that the continuum emission surrounding IRS 13E is also locally enhanced, with a spatial extent of the diffuse

emission in L comparable to that of the bright ionized gas emission traced by the $\text{Pa}\alpha$ emission described above. The origin of this emission in L will be discussed in Sect.4.6.

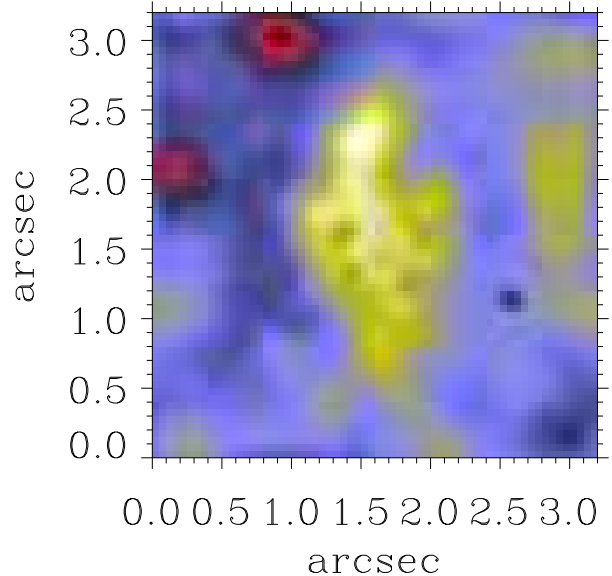


Fig. 6. Diffuse emission of the IRS 13E complex in the L band after the deconvolution operation with the MCS code.

3.8. $\text{Br}\gamma$ and $2.058\mu\text{m}$ line profiles

On Fig. 7 is presented the stellar $\text{Br}\gamma$ and the $\text{He I } 2.058 \mu\text{m}$ line profiles extracted on the same aperture size (3×3 pixels) from each BEAR data cube, at the location of the IRS 13E spot. With the spatial resolution of the BEAR data the relative contribution of the two emission line stars 13E2 and 13E4 is mixed. Remarkably, $\text{Br}\gamma$ is a much narrower line than the $\text{He I } 2.06 \mu\text{m}$ line with a FWHM of 215 km s^{-1} , compared with $\sim 900 \text{ km s}^{-1}$ for the helium line, as already measured (Paumard *et al.* 2001). The two lines should belong to two different sources, which is discussed in Sect. 4.2.

3.9. The $\text{He II } 2.189\mu\text{m}$ and the $[\text{Fe III}]$ lines

Previous spectroscopic analysis reported a tentative identification of a weak $\text{He II } 2.189 \mu\text{m}$ line (7–10) for IRS 13E (Krabbe *et al.* 1995, Najarro *et al.* 1997, Blum *et al.* 1995). This line is the most intense for this ion in the K band, and is unblended, while the 8–14 line cannot be distinguished from $\text{Br}\gamma$ of which it is separated by less than 2 cm^{-1} . The He II line can be a temperature indicator in the classification of hot stars. The BEAR emission spectrum of IRS 13E in this spectral region does not show any convincing trace of this line. Hence, contrary to Krabbe *et al.* (1995), we cannot claim that a “weak but clearly detected $2.189 \mu\text{m}$

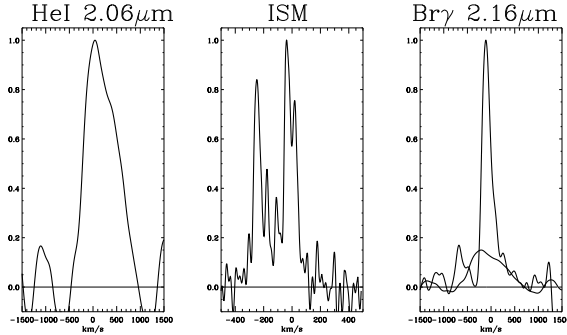


Fig. 7. He I $2.06\mu\text{m}$ and Br γ emission line profiles normalized to 1, at IRS 13E from the BEAR data, after cleaning of the stellar profiles from the interstellar emission (ISM). The multi-component local ISM emission, extracted from a ring around IRS 13E in the Br γ data, used for the correction of the Br γ profile, is shown in the middle panel. A broad profile of same width than the He I profile is adjusted on the Br γ profile showing the most probable contribution of IRS 13E2 to the observed Br γ profile.

emission”, supposed to be He II, is present at IRS 13E. However, this controversial detection was used by the authors as an argument to propose IRS 13E as a WN9 star. From the BEAR data cube covering all the central parsec there is no trace of this emission line. Note that in the $1.95 - 2.25\mu\text{m}$ spectrum of IRS 13E from Genzel *et al.* (1996) there is no obvious signature of the $2.189\mu\text{m}$ line.

From a K-band spectrum of the mini-cavity Lutz *et al.* (1993) attributed to [Fe III] several emission lines (2.145 , 2.218 , 2.242 , $2.348\mu\text{m}$). Images at $2.218\mu\text{m}$ show that this line is present all over the mini-cavity, with a particular enhancement at the position of IRS 13. From other NICMOS data in the F164N filter (Stolovy *et al.* 1999) the lower ionized Fe species, Fe II is detected in emission in the central ISM, particularly strong at the edge of the mini-cavity, but remarkably absent at the position of IRS 13E. As mentioned in this latter paper the ionization condition for [Fe III] requires 16.2eV while only 7.2eV are required for [Fe II]. Harder ionization radiation is likely originating from IRS 13E.

3.10. Spectral energy distribution and extinction law

The photometric measurements presented in Table 2 have been used to build the SED of the IRS 13 components, between 1 and $4\mu\text{m}$, and also of all the stars detected in the surrounding field. To achieve the final goal of finding the spectral type of these stars, a dereddening has to be applied over this range. The extinction law in the direction of the Galactic Center has been the object of several studies (Rieke 1999). The reddening is highly variable (Blum *et al.* 1996), which makes the correction to apply to a given object very delicate. We took the most recently published law, which is a merging of previous works (Moneti *et al.* 2001), and adjusted A_v , making the simplifying assump-

tion that the reddening toward IRS 13E and its close environment would be identical for all the sources. For this adjustment we were helped by two constraints: IRS 13E2 and 13E4 are emission line sources (Fig. 4), therefore hot sources with a blue SED, while IRS 13W is a cool star (Krabbe *et al.* 1995). Black-body curves were fitted to the data. A_v was adjusted in order to fulfill the two constraints. Higher values of A_v tend to make the sources bluer, lower values of A_v the sources redder. Temperatures higher than $25,000\text{K}$ had to be introduced for IRS 13E2 and 13E4, which correspond to the Rayleigh-Jeans regime in this spectral range. In that case, only a lower limit of T_{eff} can be derived. The slope of the SED becomes constant in a $\log[F(\lambda)]$ diagram. The adjustment of A_v makes possible to bring the SED parallel to the data points. Finally, a value of $A_v = 35$ was adopted. A mean value of $A_v = 30.5$ was determined by Rieke (1999) from a survey of the stars in the central parsec, which excluded objects like IRS 13 from the color-magnitude diagram because of the surrounding dust. We confirm locally a much higher A_v value.

However, it appeared that the fit of the dereddened data from Table 2 was not possible with a single temperature for the IRS 13 sources, but by the sum of two black-body curves. The sources show an infrared excess, likely the signature of thermal dust emission. The adjustments was made as a sum of two black-body curves, $Coef_1 \times BB(T_1) + Coef_2 \times BB(T_2)$. The high temperature T_1 is mainly determined by the data points between 1 and $2.5\mu\text{m}$ while T_2 is constrained by the 2 to $4\mu\text{m}$ points. The four parameters for each star are presented in Table 7. The NICMOS F110M and the L data were essential to fully constrain the SED of each source.

Table 7. Fitting parameters of the SED of the IRS 13E sources and IRS 13W. The spectral type of each source as discussed in Sect. 4 is summarized in the last column.

Star	$Coef_1$	T_1 K	$Coef_2$	T_2 K	Sp. Type
W	23.00	2600	1700	650	M5III
E1	0.900	≥ 25000	12000	550	O5I
E2	0.720	≥ 25000	40000	550	WC9
E4	0.140	≥ 25000	45	1550	O5IIIe
E3A	0.460	3800	33000	610	d. WR ^a
E3B	0.375	3800	29000	580	d. WR
E5	0.070	6000	9800	630	d. WR
E6	0.032	≥ 25000			O5V

a : dusty Wolf-Rayet star

4. Nature of the IRS 13 sources

From all the results presented above a classification of the stars detected in the IRS 13E complex can be proposed:

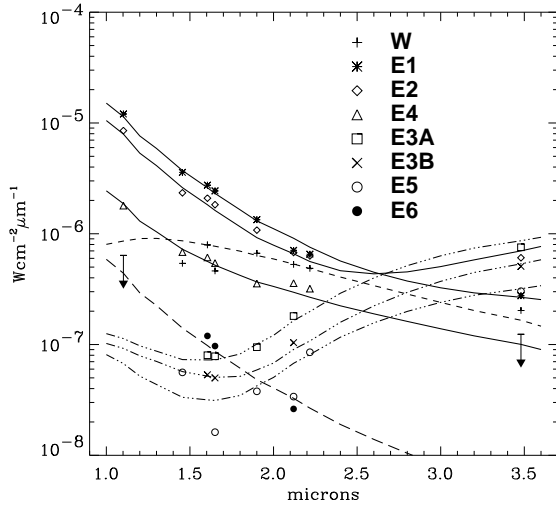


Fig. 8. Dereddened flux from Table 2 converted to $W \text{ cm}^{-2} \mu\text{m}^{-1}$ for $A_v = 35$. The top of the arrows represents the upper limit of the detectable flux in the $1.1 \mu\text{m}$ and the L-band filters. The various lines represent the best fitting between 1 and $4 \mu\text{m}$ of the data points from a two-component model with the parameters of Table 7.

4.1. IRS 13E1

This source is characterized by:

- no emission detected in $\text{Pa}\alpha$ (Fig. 4),
- an elongated envelope in H and Kp toward 13E2, which shows at the star position a FWHM of 180 mas (to compare to the 40 mas of the PSF) or 1435 AU (Fig. 2),
- a SED fitted by a $\geq 25,000 \text{ K}$ source and an infrared excess at 550 K (Table 7),
- a K_{mag} of 10.9 (Table 5). At the distance of the GC and with the adopted extinction, IRS 13E1 is too luminous to be a dwarf star. A O5V star of comparable T_{eff} will have a $K_{\text{mag}} \simeq 14$ (with $A_K \simeq 4$). IRS 13E1 is ~ 3 magnitudes brighter.

Hence, from all these elements IRS 13E1 must be a blue, supergiant star, but with no apparent emission line. The surrounding halo of scattered emission is indicative of a strong stellar wind, which also favors the identification of a massive, hot star. Consequently, IRS 13E1 might be close to a O5I spectral type. However, at the position of the source there is no evidence in the $\text{Pa}\alpha$ image of a negative level (Fig. 4), which would be the signature of the photospheric hydrogen line in absorption. Possibly, with the uncertainty on the adjustment of the continuum subtraction from the $1.87 \mu\text{m}$ filter, the integrated emission from the envelope in the image can be compensating the photospheric absorption. Only a near-infrared spectrum of IRS 13E1 taken alone could confirm this assumption.

4.2. IRS 13E2 and 13E4

IRS 13E2 and 13E4 are two emission line stars (Fig. 4). In the K band IRS 13E2 is brighter than IRS 13E4 by a factor $\simeq 2$ (Table 5). In the L band 13E4 is no longer detectable while 13E2 can be still measured. With this detection it turns out that all the spectra of IRS 13E obtained up to now (see references in Introduction) are in fact the combination of two emission line stars which are likely different.

A decisive element on the different type of the two emission stars is reported by Cl net *et al.* (2003). From spectro-imaging with a FP in the helium line behind the CFHT-AO system they indicate that IRS 13E2 is the only helium emitter. The radical difference of linewidth between the $\text{He I } 2.06 \mu\text{m}$ and $\text{Br}\gamma$ emission line profiles at IRS 13E (Fig. 7) brings another piece of information. A similar difference of linewidth of the $\text{He I } 2.06 \mu\text{m}$ lines is observed among the hot stars of the central cluster (Paumard *et al.* 2001), leading to the identification of two classes of massive stars. Applying this criterion to IRS 13E2 and 13E4, and taking into account the detection of $\text{He I } 2.06 \mu\text{m}$ only at IRS 13E2, it can be concluded that IRS 13E2 is a strong helium emitter, hence a late-type WC star (Figer *et al.* 1999). A $T_{\text{eff}} \geq 25,000 \text{ K}$ estimated for the source (Table 7) is consistent with this identification. IRS 13E4 with also a $T_{\text{eff}} \geq 25,000 \text{ K}$ (Table 7), but no helium emission, source of the narrower $\text{Br}\gamma$ profile, is more likely a less evolved star than IRS 13E2, because its initial mass was smaller than for 13E2. From its SED and its absolute brightness in K, fainter than IRS 13E1, IRS 13E4 can be reasonably proposed as a O5eIII star.

However, there is an apparent contradiction between this conclusion and the observed strength of the $\text{Pa}\alpha$ emission at IRS 13E2 which is expected to be weak since late-type WR stars have burnt most of their hydrogen, and have become helium-rich stars. In addition, if $\text{Pa}\alpha$ is strong anyway at IRS 13E2, in the BEAR data the $\text{Br}\gamma$ profile at IRS 13E should be as wide as the $\text{He I } 2.06 \mu\text{m}$ profile. That is not what is observed as shown on Fig. 7. To reconcile these two facts, it must be noticed that $\text{Pa}\alpha$ is far from a perfect indicator with narrow-band imaging technique, to distinguish between hydrogen-rich and helium-rich emitters since the $\text{Pa}\alpha$ line ($1.8751 \mu\text{m}$) is blended with a strong helium line, $\text{He I } (4-3)$ at $1.8697 \mu\text{m}$. There is another helium line within the bandpass of the continuum filter, at $1.9089 \mu\text{m}$, but which is weak and will contribute to subtract only a little of the helium emission. All these features are well seen in the CGS4 spectrum of the AF star around $\text{Pa}\alpha$, presented by Najarro *et al.* (1994), which is another helium star belonging to the class of the broad-line stars (Paumard *et al.* 2001). Hence, the intensity in the F187N-F190N image at the star position cannot be considered as a fully reliable measurement of the true $\text{Pa}\alpha$ emission in the stellar atmosphere. The bright spot at IRS 13E2 in Fig. 4 is likely due to the $\text{He I } 1.8697 \mu\text{m}$ line and with only a small contribution of the $\text{Pa}\alpha$ emission. That is consistent with the $\text{Br}\gamma$ profile shown on Fig. 7

which can be decomposed into a narrow line, whose origin must be IRS 13E4, and a fainter, broad component of same width than the HeI $2.06\mu\text{m}$ line, which should be the contribution of IRS 13E2 to the observed profile. The residual Br γ profile shows a P Cyg profile, typical of hot stars with an extended atmosphere created by strong outflows, consistent with the spectral type attributed to IRS E4.

It can be noticed that the two emission lines do not have exactly the same radial velocity, a positive velocity of $\simeq 30\text{ km s}^{-1}$ for IRS 13E2 and a negative velocity of $\simeq 30\text{ km s}^{-1}$ for IRS 13E4 while they have an identical proper motion (Table 6). At least, it can be precised for these two sources that they are animated of a motion of rotation in a plane perpendicular to the direction of the mean motion, around the barycenter, which from the relative position of the sources, should be almost coincident with IRS 13E3.

4.3. IRS 13E3 sources

IRS 13E3, almost at the center of the triangle formed by 13E1, 13E2 and 13E4, resolves into a double source in the deconvolved AO images in H and Kp (Fig. 2). Their projected separation is equal to $\simeq 600\text{ AU}$ (Table 3.2). The two sources are spectrally quite identical. They are extremely red objects as indicated by the photometric measurements in Table 5, and from their SED (Fig. 8). They are faint in the H band and prominent in the L band. We measure a K-L index of ~ 5 for the two components (Table 5). Several sources in the inner parsec, mainly located along the Northern Arm (IRS 1W, 2, 3, 5, 10W), are also very red objects, with a K-L index larger than 3, reported in Clénet *et al.* (2001). IRS 1W and IRS 21 have featureless spectra in the K band (Blum *et al.* 1996). IRS 21 has been studied in detail, from 2 to $25\mu\text{m}$ by Tanner *et al.* (2002). The SED of IRS 21 is fitted by a two-component model, the near-infrared scattered light from the central source peaking at $\simeq 3.8\mu\text{m}$ (760 K), and the mid-infrared re-emitted light from the dust shell at $\sim 250\text{ K}$. They conclude that IRS 21 is a dusty WR star, experiencing rapid mass loss, and by analogy the other luminous Northern Arm sources as well. The IRS 13E3 SEDs are also fitted by two components (Table 7), but with respectively 3800 K and 600 K. IRS 13E3A and E3B are likely sources of the same type as IRS 21 and the other Northern Arm sources. The higher temperature of the infrared component can come from the additional heating of the dust shell by the very close, massive, blue stars, IRS 13E1, 13E2 and 13E4. That is also consistent with IRS 13 being not a prominent source at $12.5\mu\text{m}$ from images in this band (Tanner *et al.* 2002).

4.4. IRS 13E5

One of the sources revealed by deconvolution of the AO images (Fig. 2) we propose to name IRS 13E5, is con-

firmed by Ott *et al.* (2003) from SHARP data (Table 3). From the dereddened photometry (Fig. 8) this source has a SED similar to IRS 13E3A and E3B, being roughly a factor 2 fainter than each of the IRS 13E3 components. Its SED is also fitted by two thermal components, with temperatures of the same order than for 13E3A and E3B (Table 7). From this similarity we propose that IRS 13E5 is another example of dusty WR star, possibly more embedded, behind IRS 13E3A and E3B.

4.5. IRS 13E6

IRS 13E6 is detected only in H and in the F160W filter, a broader H filter, and near the detection limit of the Kp band (Table 2). It is not detected by Ott *et al.* (2003) whose data come from K-band imaging on the NTT. With $T_{\text{eff}} \geq 25,000\text{ K}$ and $K_{\text{mag}} = 14.56$ (Table 5) 13E6 is a weak, hot star, 3.5 magnitudes fainter than IRS 13E1. It can be considered as close to a main sequence O5V star.

4.6. The diffuse halo

In Sect. 3.7 has been described another component, a diffuse halo around the star complex, clearly detectable in the continuum at $3.5\mu\text{m}$ (Fig. 6). At larger scale, over the central parsec, a diffuse emission is seen in the mid-infrared (Tanner *et al.* 2002) whose structure is following the intensity map of the ionized gas forming the Mini-spiral (Stolovy *et al.* 1999, Morris & Maillard 2000). This mid-infrared emission is assumed to be the thermal emission from dust, following the fast flowing motion of the gas (Paumard *et al.* 2003a), heated through the trapping of Ly α photons (Rieke *et al.* 1989). Hence, the similarity of shape of the diffuse emission in L and of the ionized gas in the vicinity of IRS 13E is natural. In the analysis of the local structure of the interstellar gas (Sect. 3.6) we have shown that the enhanced structure from the Mini-cavity was on the line of sight. Thus, we can infer that this background emission to IRS 13E in the L band is also due to the Mini-cavity, by the dust swept by the star wind responsible for the Mini-cavity, and then not directly related to the star cluster itself. However, the ionized gas emission is particularly enhanced at the same location, in Pa α , Br γ (Fig. 5, and in the lines of [Fe III] as mentioned in Sect. 3.9. These lines, in particular those from [Fe III] (Lutz *et al.* 1993) are signature of a strong ionizing UV flux. Part of it must have for origin the concentration of the three massive, hot stars, 13E1, 13E2 and 13E4. Consequently, a higher density of dust mixed with the gas illuminated by a stronger UV field creates this intense background in the continuum at $3.4\mu\text{m}$ and in the gas emission. On the other hand, the diffuse continuum seen at shorter wavelength, in H and Kp (Fig. 2), peaking at 13E1 and 13E2, the two brightest sources of the complex in these bands, and between the two stars, appears of different origin than the thermal continuum imaged in the L band. It is likely

dominated by the scattered stellar light from the two blue stars on the surrounding dust.

A particular question to ask, is this diffuse halo going to pass IRS 13E? The star cluster has a westward, mean proper motion (Table 6) of $\sim 280 \text{ km s}^{-1}$ and the edge of the Mini-cavity of 200 km s^{-1} (Zhao & Goss 1998). The positional offset between IRS 13E and the Mini-cavity centroid will remain almost constant.

4.7. IRS 13W

This star is associated with IRS 13 only for historical reasons. We kept it in all the study since its cool stellar type, attested by the presence of CO in its K-band spectrum (Krabbe *et al.* 1995), was a precious constraint on the determination of the local value of A_v . In the deconvolved Kp-band image 13W shows a size larger than the PSF which might be indicative of a dusty envelope, attested also by a significant infrared excess (Table 7). In the photometric survey of Ott *et al.* (1999) IRS 13W presents a high index of variability. Hence, we can conclude that IRS 13W with a T_{eff} of $\sim 2300 \text{ K}$ and these characteristics should be more likely of Mira-type. This should be confirmed by a better near-infrared spectrum than currently available, which should show the absorption of H_2O on each side of the K band. The discrepancy of some measurements with the black-body curve (short-dashed line on Fig. 8) might be resulting from photometry taken at different epochs. IRS 13W should be another example of long-period variable (LPV), as many examples have been detected in the $25' \times 25'$ field around the GC by Glass *et al.* (2001).

4.8. The nearby stars

Twelve additional stars, as presented in Table 2, are found in the small field around IRS 13E. Note they are only detected in the 1 - $2.3 \mu\text{m}$ range. They offer an opportunity of studying in detail a small sample of the central parsec stellar population. By fitting black-body curves as for the IRS 13E components (a single temperature component was required) we obtained the following results, under the assumption of the same A_v as for IRS 13. Nine stars are main sequence K and M stars, with T_{eff} from 2800 to 5000 K. Hence, they belong to the numerous old star population of the GC (Blum *et al.* 1996). The three remaining stars (# 7, 12, 18) are very hot stars, with $T_{eff} \geq 25,000 \text{ K}$ and K_{mag} respectively of 12.2, 13.3 and 14.5 (Table 5). As suggested for IRS 13E6, they can be main sequence O stars. Can they be more examples of WR stars, hot stars which are supposed to be weak in the K band, as having lost most of their initial mass? From the absence of noticeable emission lines in Pa α , the lack of infrared excess, the first hypothesis is more plausible. In any case, these sources which would complete the population of massive stars in the central parsec deserve a more detailed study.

5. Model of IRS 13E as a star cluster

IRS 13E appears as only composed of hot, massive stars. This concentration cannot be fortuitous. The high density of stars in the central parsec cannot explain IRS 13E, with at least 7 stars of this type within $0.5''$. Further deep high-spatial resolution imaging could eventually reveal more components. The common direction and comparable amplitude of the proper motions of the main components (see Sect. 3.4 and Table 6) is a decisive argument to indicate that 13E1, 13E2, 13E3A/B and 13E4 are physically bound. Regarding 13E5 for which no proper motion cannot be currently measurable, its spectral type, identical to 13E3A/B, led us to conclude that this source belongs to IRS 13E too. Only IRS 13E6 is questionable since no proper motion can confirm its relation to the other sources. It could be another star similar to # 7, 12 and 18 discussed above. However, as another hot star, of O-type, it could also belong to the IRS 13E complex. To conclude, the source historically called IRS 13E is a compact star cluster, which also means a young star cluster of a few 10^6 yr old, since several members are identified as having already reached the WR stage.

6. What is the source of the X-ray emission at IRS 13?

The origin of the X-ray emission at IRS 13 reported by Baganoff *et al.* (2003) for the position, by Coker *et al.* (2002) for the spectrum, by Munro *et al.* (2003) for complementary data on the energy distribution, must be re-examined in light of the current identification of the components of the IRS 13E cluster. According to Baganoff *et al.* the X emission source is located $0.56''$ northeast of IRS 13W. Using the same absolute coordinates for the X-ray source and for SgrA*, we do not perfectly agree with this statement. From our astrometry (Table 3) this position falls $0.71''$ exactly east of IRS 13W (Fig. 3). This small discrepancy is within the positional uncertainties and given the $\sim 0.5''$ resolution of Chandra, a discussion on the potential candidates for this discrete X-ray source can be based on the physical nature of the stellar components which might fall in the error box. We briefly examine several hypothesis which may need further analysis with more details on the X-ray source itself.

6.1. IRS 13E2

Coker *et al.* (2002) proposed that this star is the source of the X-ray emission and must be a post-LBV binary. The object falls in the error box (Fig. 3) and we propose that IRS 13E2 is indeed a late-type WR. The conclusion of Coker *et al.* is based on a fitted characteristic temperature from the X-ray spectrum of $kT \simeq 1.0 \text{ keV}$, consistent with the shocked winds of a WR + O system. The solution is tempting since binary Wolf-Rayet stars are known to be bright X-ray sources, brighter than LBV sources. Models of WR star X-ray spectra coming from colliding winds

have been made for WR + O binary systems like WR 140 (Zhekov & Skinner 2000), in which the two stars are quite close, agreeing well with observation. In the young star cluster R136 in 30 Dor, a cluster quite comparable to the Arches in the Milky Way, Portugies Zwart *et al.* (2003) detect a dozen X-ray sources that have bright WN Wolf-Rayet or spectral type O stars as optical counterparts, of which about half are WR + O binaries. The only way to prove the binarity of IRS 13E2 would be the detection of a periodic variability of the X-ray emission, or of the radial velocity in the infrared spectra, which supposes repeated observations over several days. However, it can also be noticed that there are currently 13 helium sources identified as WR stars in the central parsec (Paumard *et al.* 2003b), and none of them is reported as coincident with a X-ray source (Baganoff *et al.* 2003), except perhaps CXOGC J174539.4-290031 indicated as coincident within $0.52''$ with AF NW. The identification is also tentative. Ott *et al.* (1999) from their long-term photometric analysis have shown that IRS 16SW is indeed an eclipsing binary with a 9.7-day period. It might be the candidate for this type of X-ray source, and no X-ray source is reported there. In the same study IRS 13E2 does not present characteristics of rapid, periodic variability in the K band. That does not preclude IRS 13E2 to be a binary. However, some other origin of the emission must be considered.

6.2. The core of the IRS 13E cluster

If no other X-ray source is detected associated with the numerous WR stars identified in the central parsec, the rare proximity of several massive, hot stars with high mass loss and very fast winds, as we have shown that IRS 13E is composed, can make the case for the blending of the emission from all these colliding winds making in total a hard X-ray source. The deconvolution of the H and Kp-band images of IRS 13E (Fig. 2) shows a bridge of diffuse emission between 13E1 and 13E2. By comparison to the positions of the IRS 13E components on the VLA map at resolution of $0.06''$ of Zhao and Goss (1998) it appears that the two intense and compact He II regions they detect in the complex called He II 7-IRS13, at 7 and 13 mm just falls at half distance between 13E1 and 13E2. All these facts are signatures of an important wind interaction between the hot components of the IRS 13E cluster. The general shape of the X-ray spectrum between 2.6 and 6 keV published by Coker *et al.* 2002 and the clear emission line in this range, at ~ 3 keV, suggests that the full spectrum might look like the A1 source spectrum from the Arches cluster (Yusef-Zadeh *et al.* 2002). This source which is coincident with the core of the cluster shows the same narrow emission line at 3 keV, but plus two other atomic lines, at 2.5 and 3.8 keV, that the poor S/N ratio of Coker *et al.* spectrum compared to the A1 spectrum prevents to confirm. Unfortunately, the X-ray spectrum presented in Baganoff *et al.* is the integrated emission from the four point sources within a $10''$ radius of SgrA*. It includes the contribution

of the source potentially associated with IRS 13E, the one associated with AF NW plus two other sources, CXOGC J174539.7-290020 and CXOGC J174539.7-290022, which the two combined are brighter (number of counts s^{-1} in the 0.5 -7.0 keV band) by a factor 3 than the IRS 13E source. Atomic lines at the right position are possibly present but with a low contrast in this coaddition. Only a good S/N ratio X-ray spectrum of the IRS 13E source alone could confirm this hypothesis. In any case, IRS 13E as a compact, massive star cluster would be consistent with this origin for the X-ray emission at this position, providing also a better astrometry for the X-ray source. It could be consistent as being among the brightest, discrete X-ray sources, besides SgrA* itself, in the central parsec (Baganoff *et al.* 2003).

6.3. A source independent of IRS 13E

A systematic X-ray survey of the Galactic Center region at sub-arcsecond scale with Chandra by Munro *et al.* (2003) over a field of $17' \times 17'$ centered on SgrA* has revealed more than 2000 discrete X-ray sources. Stellar remnants, white dwarfs with magnetically accreting disks, binaries with neutron stars or solar-mass black holes are considered as responsible for a large fraction of these discrete sources. Such a source, too weak in the near infrared to be detected, could be present on the line of sight of IRS 13, since as measured by Munro *et al.* the distribution of the density of discrete sources peaks in the central parsecs. The binary explanation is based on a distinct emission feature centered at ~ 6.7 keV and otherwise a featureless spectrum. The spectrum presented by Coker *et al.* (2002) stops at 6 keV, probably because no energy was detected beyond. But, as already mentioned, it shows a narrow emission line at 3 keV. Wang *et al.* (2002) indicate that this line should be due to the contribution of massive stars. Hence, the X-ray source at IRS 13 might be more likely associated with the IRS 13E cluster.

7. The remaining core of a massive star cluster

The large number of massive stars in the central parsec, which are very rare elsewhere in the Galaxy, remains one of the major mysteries of this region. Since star formation would be difficult due to the strong tidal forces from the SgrA* black hole, Gerhard (2001) made the interesting hypothesis that the central parsec He I stars, the most prominent of the massive young stars, might be the remains of a dissolved, young cluster, which originally formed further away from SgrA*. He argued that the Arches and the Quintuplet clusters, located within ~ 30 pc projected distance of SgrA*, testify that star formation by cluster of massive stars has been occurring in the nuclear disk of the Galaxy. If one examines Table 7, IRS 13E appears as a kind of summary of all the spectral types of young stars observed in the central parsec from O to WR. This concentration is unique. In Paumard *et al.* (2001) we associated systematically to each helium star the AO image of the

local field in order to check whether the emission source was single or not. Only IRS 13E appeared multiple, which motivated the current study. With its exceptional concentration of massive stars, very close to SgrA*, is IRS 13E the remaining core of such a cluster which was disrupted by SgrA*?

7.1. The fate of a star cluster near SgrA*

Morris (1993) has argued that it would take longer than the lifetime of massive young stars to transport them inward within the central parsec if they formed at too large distance. The same argument is applied again by Figer *et al.* (2000), who claim that the SgrA* cluster could not have formed more than 0.1 pc from the center, and then, the initial clump should have an exceptional density $\geq 4 \cdot 10^{11} \text{ cm}^{-3}$. Gerhard (2001) discarded this argument by a revision of the conditions for a cluster formed at 30 pc to spiral into the center within the lifetime of its most massive stars. The main condition is that the initial mass of the parent cloud in which the cluster forms must be massive enough ($\simeq 2 \times 10^6 M_{\odot}$) to survive the evaporation in the strong tidal field of the nuclear bulge. He concludes that clusters significantly more massive than the Arches cluster and formed a little closer than 30 pc can reach the central parsec in due time. In order to test this statement Kim & Morris (2002) have made several simulations, for different masses ($10^5 M_{\odot}$ and $10^6 M_{\odot}$) and different initial orbit radii (2.5 to 30 pc), of the dynamical friction on a star cluster near SgrA*. They came to the conclusion that some simulations can be regarded as candidates for the origin of the central parsec cluster, but that “the required conditions are extreme”, with an initial mass of the cluster of $10^6 M_{\odot}$ or a very dense core $\geq 10^8 M_{\odot} \text{ pc}^{-3}$ (Kim *et al.* 2003). An initial mass of the cluster of $10^6 M_{\odot}$ supposes a very large number of initial particles, $> 10^4$ with stars of initial mass $\geq 10^2 M_{\odot}$ to reach rapidly the WR stage.

In fact, the two sub-groups detected among the He I stars (Paumard *et al.* 2001) seem to be indicative of two populations, one of initial masses $100 M_{\odot}$ to $\simeq 120 M_{\odot}$ objects which already evolved to the WR stage (E2, E3A, E3B, E5 from IRS 13E are examples) and another one of ~ 40 to $100 M_{\odot}$ whose sources have reached the LBV stage (the IRS 16 sources are examples). In any case, the number of particles in the initial cluster must be huge ($\geq 10^4$) to reach the required total mass. When compared to the relatively small number of detected helium stars, concentrated in the central parsec, ~ 19 from the last revision by Paumard *et al.* (2001), plus few more dusty WRs, this discrepancy seems an argument against this scenario.

However, another analytic work by McMillan & Portegies Zwart (2003) has reconsidered the fate of a star cluster near the central dark mass. They have tried to address more completely the problem by taking into account, in addition to the initial mass and the distance to the center, the original mass function of the cluster, the initial cluster radius and the stellar evolution through

mass loss during the inspiral time of the cluster. They conclude that star clusters born with masses $\simeq 10^5 M_{\odot}$ within 20 pc from the center, with a half-mass radii of ~ 0.2 pc can reach a final distance of 1 pc within 10 Myr. As a secondary conclusion the known star clusters, the Arches and the Quintuplet, from their mass and their distances, will not reach the vicinity of SgrA*. This latter work makes the origin of the central, massive star cluster by the dissolution of a compact cluster in the galactic tidal field more plausible, not requiring extreme mass conditions as in the simulation of Kim *et al.* (2003). This latter work makes the origin of the central, massive star cluster by the dissolution of a compact cluster in the galactic tidal field more plausible, not requiring extreme mass conditions as in the simulation of Kim *et al.* (2003).

7.2. Census of the hot stars in the central parsecs

A complete census of the hot stars in the central parsecs could help to better characterize the initial mass of this hypothetical cluster. The current count is likely complete for the brightest members of the young star population. However, as was already pointed out in the conclusion of Paumard *et al.* 2001, the count of WR stars is certainly incomplete because these stars are fainter in average by at least 2 mag (in K) than the IRS 16 stars. The faintest one which was identified has $K_{mag} \simeq 13$. The identification depends on the detection of broad lines ($\sim 1000 \text{ km s}^{-1}$) over a weak continuum which is difficult. With the upcoming spectro-imaging data behind AO systems on large telescopes, more of these stars can be detected. As an example, IRS 13E, which counted previously for a single WR star now counts for 4. In addition, several infrared sources which had eluded classification because they presented featureless spectra are now better explained by dusty WR (Tanner *et al.* 2002). There are at least 6 of these sources. The Pa α emission map, of which we used a small portion, is another potential source for detecting other emission line stars. A survey of all the Pa α point-like sources in the central parsecs includes the known He I stars, but there are additional weaker sources, indicative of other emission stars. With conservative detection criteria a total of 20 new emission stars are detected in the central parsec (Paumard *et al.* 2003b), in agreement with the independent study of Scoville *et al.* (2003). IRS 13E4 is an example of such a star.

Emission-line stars are not all the hot stars. Another example of massive star is provided by a star like IRS 13E1, with no emission line, which can be identified as such only by deep spectrophotometry in the near infrared. Then, the four stars, IRS 13E6, # 7, 12, 18, are representative of a group of main sequence, less massive, hot stars. What about the origin of the S-cluster in $\sim 1''$ of SgrA*? From the first spectroscopic observations (Genzel *et al.* 1996, Ghez *et al.* 1999, Figer *et al.* 2000, Gezari *et al.* 2002) the absolute K magnitudes and spectra suggest that they are late O - early B main sequence objects. All these

findings indicate that the distribution of young stars in the central parsec include many young stars from several solar masses to stars with initially more than $100 M_{\odot}$.

In conclusion, we propose that the IRS 13E cluster, by its unique location and its unique composition is the possible core of an earlier massive star cluster, formed about 10 millions years ago, within 20 pc of SgrA*, more massive than the Arches, which was the progenitor of the entire hot star population, from WR to O-type stars, observed today in the central parsecs of the Galaxy. So far, with the very high extinction, only the most massive (helium stars) and examples of intermediate and lower mass objects have been detected. A complete survey of all the young stars in the central parsecs, first attempted by Rieke *et al.* 1999 needs to be completed. This type of work has been already undertaken for the Arches. The mass function (MF) from VLT/NAOS-CONICA data (Stolte *et al.* 2003) includes more than 1300 objects going from 1.3 to $60 M_{\odot}$. It confirms an overabundance of massive stars ($\geq 20 M_{\odot}$), with an indication of massive stars segregation in the cluster center. Following the assumption of a single star formation event for the central, hot star cluster, the same work could make possible to derive the IMF of this massive cluster, its total number of particles and an estimation of its total mass. The measured velocities of the particles (proper motions and when possible radial velocities), the observed hot star segregation (Paumard *et al.* 2001), would be other elements for the full modeling of a star cluster sinking toward the Galactic Center as proposed by McMillan & Portegies Zwart (2003).

8. Conclusion

The presence of a compact star cluster of hot, massive stars, close to SgrA* at the position of IRS 13E is demonstrated. The spectral types of the various members range from O5 to WR, including dusty WRs. This object which is unique in this environment is proposed as the remnant of a primitive, massive star cluster, of $10^5 M_{\odot}$, as has been proposed by McMillan & Portegies Zwart (2003). The interaction of the strong winds from all the hot, massive stars in the remaining core is proposed as the origin of the discrete X-ray source possibly detected at this position.

To confirm and complete the above analysis on the spectral type of all the individual sources within IRS 13E, spectroscopy in the 1-5 μm range is required. Angular resolution as good as $0.1''$ for such a very compact field is required. Sensitive spectroscopy in the L and M bands should confirm the expected featureless spectrum of the IRS 13E3 and 13E5 objects. These studies will need near-infrared 3-D spectrometers behind an AO system on a 8-m telescope like SINFONI (Mengel *et al.* 2000 and AMBER behind VLTI (Petrov *et al.* 2000). Proper motions of the fainter members of the cluster will help to confirm that all the individual sources are kinematically bound together. More generally, as was illustrated in this paper, the full census of the hot star population in the central parsecs re-

mains to be completed. New deep data already obtained with NAOS/CONICA on the central parsec (Ott *et al.* 2003) should help. They need to be associated with photometric data from AO systems with high Strehl ratio down to $1 \mu\text{m}$, enlarging the type of data only possible with NICMOS on HST.

This study is also an illustration of the renewal of the stellar population census in the GC brought by X-ray data. Priority targets for deep, near-infrared, high spatial resolution imaging, must be other star-like X-ray sources detected by Chandra in the central parsec (Baganoff *et al.* 2003) like CXOGC J174540.9-290014, CXOGC J174539.7-290020 and CXOGC J174539.7-290022) which have no proposed optical counterparts.

Acknowledgements. We gratefully acknowledge helpful discussions with Robert Coker at the start of the project which stimulated the close examination of the high-resolution data available on IRS 13. We want to warmly thank Yann Clénet (Meudon Observatory) who accepted to make available to us his adaptive optics data in the L band. Thanks to the organizing committee led by Tom Geballe, the GC2002 Workshop in Kona was an ideal place to discuss and to improve the various issues raised in this paper. Special thanks are also due to Thomas Ott who accepted to send us the proper motions of the sources of the IRS 13 field, prior to publication.

References

- Allen, D.A., & Sanders, R.H. 1986, *Nature*, 319, 191
- Baganoff, F.K., Maeda, Y., Morris, M., Bautz, M.W., Brandt, W.N., Cui, W., Doty, J.P., Feigelson, E.D., Garmire, G.P., Pravdo, S.H., Ricker, G.R., & Townsley, L.K. 2003, *ApJ*, 591, 891
- Beuzit, J.L., Demailly, L., Gendron, E. *et al.* 1997, *ExA*, 7, 285
- Blum, R.D., DePoy, D.L., & Sellgren, K. 1995, *ApJ*, 441, 603
- Blum, R.D., Sellgren, K., & DePoy, D.L. 1996, *ApJ*, 470, 864
- Clénet, Y., Rouan, D., Gendron, E., Montri, J., Rigaut, F., Léna, P. & Lacombe, F. 2001, *â*, 376, 124
- Clénet, Y., Lacombe, F., Gendron, E., & Rouan, D. 2003, in *The Central 300 parsecs, Galactic Center Workshop*, held in Kona, Nov. 4-8, 2002, *AN*, 324 *in press*
- Coker, R.F., Pittard, M.J., & Kastner, J.H. 2002, *â*, 383, 568
- Diolaiti, E., Bendinelli, O., Bonaccini, D., Close, L., Currie, D. & Parmeggiani, G. 2000, *A&AS*, 147, 335
- Eckart, A., Genzel, R., Hofmann, R., Sams, B.J., & Tacconi-Garman, L.E. 1995, *ApJ*, 445, L23
- Figer, D.F., Kim, S.S., Morris, M., Serabyn, E., Rich, M.R., & McLean, I.S. 1999, *ApJ*, 525, 750
- Figer, D.F., Becklin, E.E., McLean, I.S., Gilbert, A.M., Graham, J.R., Larkin, J.E., Levenson, N.A., Teplitz, H.I., Wilcox, M.K., & Morris, M. 2000, *ApJ*, 533, L49
- Genzel, R., Thatte, N., Krabbe, A., Kroker, H., & Tacconi-Garman, L.E. 1996, *ApJ*, 472, 153
- Genzel, R., Eckart, A., Ott, T., & Eisenhauer, F. 1997, *MNRAS*, 291, 219
- Gezari, S., Ghez, A.M., Becklin, E.E., Larkin, J., McLean, I.S., Morris, M. 2002., *ApJ*, 576, 790
- Gerhard, O. 2001, *ApJ*, 546, L39
- Ghez, A.M., Morris, M. & Becklin, E.E. 1999, in *The Central Parsecs of the Galaxy*, ed. H. Falcke, A. Cotera, W.J. Duschl, F. Melia, & M.J. Rieke, *ASP Conf. Ser.*, 186, 18

- Glass, I.S., Matsumoto, S., Carter, B.S., & Sekiguchi, K. 2001, *MNRAS*, 321, 77
- Graves, J.E., Northcott, M.J., Roddier, F.J., Roddier, C.A., & Close, L.M. 1998, *SPIE*, 3353, 34
- Kim, S.S. & Morris, M. 2002, *ApJsubmitted*
- Kim, S.S., Morris, M., & Figer, D.F. 2003, in *The Central 300 parsecs, Galactic Center Workshop, held in Kona, Nov. 4-8, 2002*, AN, 324 *in press*
- Krabbe, A., Genzel, R., Eckart, A., Najarro, F., Lutz, D., Cameron, M., Kroker, H., Tacconi-Garman, L.E., Thatte, N., Weitzel, L., Drapatz, S., Geballe, T., Sternberg, A., & Kudritzki, R.P. 1995, *ApJ*, 447, L95
- Lai, O., Véran, J.P., Rigaut, F., Rouan, D., *et al.* 1997, in *Optical Telescopes of Today and Tomorrow*, ed. A.L. Ardeberg, *SPIE*, 2871, 859
- Libonate, S., Pipher, J.L., Forrest, W.J., & Ashby, M.L.N. 1995, *ApJ*, 439, 202
- Lutz, D., Krabbe, A., & Genzel, R. 1993, *ApJ*, 418, 244
- Magain, P., Courbin, F. & Sohy, S. 1998, *ApJ*, 494, 472
- Maillard, J.P., 2000, in *Imaging the Universe in 3 Dimensions*, ed. E. van Breughel & J. Bland-Hawthorn, *ASP Conf. Ser.*, 195, 185
- McMillan, S.L.W., & Portegies Zwart, S.F. 2003, *astro-ph/0304022*
- Moneti, A., Cernicharo, J., & Pardo, J.R. 2001, *ApJ*, 549, L203
- Morris, M. 1993, *ApJ*, 408, 496
- Morris, M., Maillard, J.P., 2000, in *Imaging the Universe in 3 Dimensions*, ed. E. van Breughel & J. Bland-Hawthorn, *ASP Conf. Ser.*, 195, 196
- Mengel, S., Eisenhauer, F., Tecza, M., Thatte, N.A., Roehle, C., Bickert, K., & Schreiber, J. 2000, in *Interferometry in Optical Astronomy*, ed. P.J. Lena & A. Quirrenbach, *Proc. SPIE*, 4005, 301
- Menten, K.M., Reid, M.J., Eckart, A., & Genzel, R. 1997, *ApJ*, 475, L111
- Muno, M.P., Baganoff, F.K., Bautz, M.W., Brandt, W.N., Broos, P.S., Feigelson, E.D., Garmire, G.P., Morris, M.R., Ricker, G.R., Townsley, L. K. 2003, *ApJ*, 589, 225
- Najarro, F., Hillier, D.J., Kudritzki, R.P. Krabbe, A., Genzel, R., Lutz, D., Drapatz, S., & Geballe, T.R. 1994, *A&A*, 285, 573
- Najarro, F., Krabbe, A., Genzel, R., Lutz, D., & Kudritzki, R.P. 1997, *A&A*, 325, 700
- Ott, T., Eckart, A., & Genzel, R. 1999, *ApJ*, 523, 248
- Ott, T., Genzel, R., Eckart, A., & Schödel, R. 2003, in *The Central 300 parsecs, Galactic Center Workshop, held in Kona, Nov. 4-8, 2002*, AN, 324 *in press*
- Ott, T., Schödel, R., Genzel, R., Eckart, A., Lacombe, F., Rouan, D., Hofmann, R., Lehnert, M., Alexander, T., Sternberg, A., & 18 coauthors, 2003, *The Messenger*, 111, 1
- Paumard, T., Maillard, J.P., Morris, M., & Rigaut, F. 2001, *A&A*, 366, 466
- Paumard, T., Maillard, J.P., & Morris, M. 2003a, *A&A submitted*
- Paumard, T., Maillard, J.P., & Stolovy, S. 2003b, in *The Central 300 parsecs, Galactic Center Workshop, held in Kona, Nov. 4-8, 2002*, AN, 324 *in press*
- Petrov, R.G., Malbet, F., Richichi, A., Hofmann, & 9 coauthors, 2000, in *Interferometry in Optical Astronomy*, ed. P.J. Lena & A. Quirrenbach, *SPIE*, 4006, 68
- Portegies Zwart, S.F., Pooley, D., & Lewin, W.H.G. 2002, *ApJ*, 574, 762
- Rieke, G.H., Rieke, M.J., & Paul, A.E. 1989, *ApJ*, 336, 752
- Rieke, M.J. 1999, in *The Central Parsecs of the Galaxy*, ed. H. Falcke, A. Cotera, W.J. Duschl, F. Melia, & M.J. Rieke, *ASP Conf. Ser.*, 186, 32
- Scoville, N.Z., Stolovy, S.R., Rieke, M., Christopher, M., & Yusef-Zadeh, F. 2003, in *The Central 300 parsecs, Galactic Center Workshop, held in Kona, Nov. 4-8, 2002*, AN, 324 *in press*, and *astro-ph/0305350*
- Simon, M., Chen, W.P., Forrest, W.J., Garnett, J.D., Longmore, A.J., Gauer, T., & Dixon, R.I. 1990, *ApJ*, 360, 95
- Stolovy, S.R., McCarthy, D.W., Melia, F., Rieke, G., Rieke, M.J., & Yusef-Zadeh, F. 1999, in *The Central Parsecs of the Galaxy*, ed. H. Falcke, A. Cotera, W.J. Duschl, F. Melia, M.J. Rieke, *ASP Conf. Ser.*, 186, 39
- Stolte, A., Brandner, W., Grebel, E.K, Figer, D.F., Eisenhauer, F., Lenzen, R., & Harayama, Y. 2003, *The Messenger*, 111, 9
- Tamblyn, P., Rieke, G.H., Close, L.M., Hanson, M.M., McCarthy, D.W. Jr, Rieke, M.J. 1996, *ApJ*, 456, 206
- Tanner, A., Ghez, A.M, Morris, M., Becklin, E.E., Cotera, A., Ressler, M., Werner, M., & Wizinovitch, P. 2002, *ApJ*, 575, 860
- Tanner, A., Ghez, A.M, Morris, M., & Becklin, E.E. 2003, in *The Central 300 parsecs, Galactic Center Workshop, held in Kona, Nov. 4-8, 2002*, AN, 324 *in press*
- Wang, Q.D., Gotthelf, E.V., & Lang, C.C. 2002, *Nature*, 415, 148
- Yusef-Zadeh, F., Law, C., Wardle, M., Wang, Q.D., Fruscione, A., Lang, C.C., & Cotera, A. 2002, *ApJ*, 570, 665
- Zhao, J.H., & Goss, W.M. 1998, *ApJ*, 499, L163
- Zhekov, S.A., & Skinner, S.L. 2000, *ApJ*, 538, 808

Annexe D

Article « *The Galactic Center source IRS 13 : a star cluster* »

**Contribution pour la conférence *Galactic Center workshop
2002*, relative au travail sur IRS 13E.**

The Galactic Center Source IRS 13E: a Star Cluster

Jean-Pierre Maillard¹, Thibaut Paumard¹, Susan Stolovy², and François Rigaut³

¹ Institut d'Astrophysique de Paris (CNRS), 98b Blvd Arago, 75014, Paris, FRANCE

² SIRTf Science Center, CalTech, MS 220-6, Pasadena, CA 91125, USA

³ Gemini North Headquarter, Hilo, HI 96720, USA

Received 15 November 2002, accepted 2 December 2002

Key words Galactic Center, star cluster, WR star, infrared, adaptive optics

PACS 04A25

High spatial resolution, near-infrared observations of the Galactic Center source, close to Sgr A^{*}, known historically as IRS13, are presented. These observations include ground-based adaptive optics images in the H, K^{*} and L bands, HST-NICMOS observations in filters between 1.1 and 2.2 μm , and spectro-imaging data in the He I 2.06 μm line and the Br γ line. Analysis of all these data has made possible to resolve the main component, IRS 13E, in a cluster of seven individual stars within a projected diameter of $\sim 0.5''$ (0.02 pc), and to build their SED. The main sources, 13E1, 13E2, 13E3 (a binary), and 13E4, are hot stars of different nature. 13E2 and 13E4 are emission line stars. The spectral type of the various members goes from O5I to WR, including dusty WRs like IRS 21 (Tanner *et al.* 2002). All these sources have a common westward proper motion. Two weaker sources, 13E5 and 13E6, are also detected within the compact cluster, with 13E5 proposed as another dusty WR and 13E6 as a O5V star. An extended halo seen around the cluster, part of the mini-spiral of dust is particularly enhanced in the L band. It is interpreted as a contribution of the scattered light from the inner cluster and the thermal emission from the dust. IRS 13E is proposed to be the remaining core of a massive, young star cluster which was disrupted in the vicinity of Sgr A^{*}, and hence, the possible source of the young stars in the central parsec, from the helium stars to the S stars.

1 Introduction

In the early mapping works of the central parsecs, a spot named IRS 13, bright at all near-infrared wavelengths, was reported, approximately located 3.6'' south-west of Sgr A^{*}. It was later resolved into two sources in the K band separated by $\sim 1.2''$, IRS 13E and IRS 13W (Simon *et al.* 1990). From spectroscopic studies in the same band, IRS 13W was identified as a cool star (Krabbe *et al.* 1995) and IRS 13E as an emission line source with strong He I 2.058, 2.112 μm , Br γ line and other Brackett lines up to Br12 (Genzel *et al.* 1996), typical of the helium stars present in the central parsec. The first adaptive optics (AO) map of IRS 13E in the K band obtained on the CFH Telescope was published by Paumard *et al.* (2001), showing that the source resolved into two equally bright components 13E1 and 13E2, plus a third weaker component called 13E3. Since the spectra of IRS 13E did not have the same spatial resolution the identification of the associated spectral type was becoming subject to caution. In the centimetric domain, Zhao and Goss (1998) found IRS 13 as the brightest radio continuum source after Sgr A^{*} at the Galactic Center. The detection of a discrete X-ray source from CHANDRA at the position of IRS 13 (Baganoff *et al.* 2001) was another element making IRS 13 a source of special interest. The high resolution images of the central parsec currently obtained at various wavelengths in the infrared are giving the possibility to study in detail this peculiar Galactic Center source. A complete description of the present work can be found in the companion paper of Maillard *et al.* (2003).

2 New data on IRS 13

Calibrated ground-based AO data from several telescopes and space-based NICMOS data in the near infrared, all containing IRS 13 in their field, plus some spectroscopic data, and the proper motions of the sources of the IRS 13 field, have all been combined.

2.1 High-angular resolution data

The AO data come from two different systems, Gemini North (Graves *et al.* 1998) for the H and the Kp ($2.12 \mu\text{m}$, FWHM $0.41 \mu\text{m}$) bands, and ESO 3.6-m telescope (Clénet *et al.* 2001) for the L band. Medium (M) and wide-band (W) filters, respectively centered at 1.1, 1.45, 1.60, $2.22 \mu\text{m}$ (coded F110M, F145M, F160W and F222M) and two close narrow-band (N) filters (F187N centered on the $1.87 \mu\text{m}$ Pa α line and F190N) were used in observing the stars at the inner parsec of the Galactic Center with the NICMOS cameras on board HST.

A small portion of $\simeq 2.5'' \times 2.5''$, roughly centered on IRS 13E, of the image from each filter was analyzed. All these high-resolution, multi-band images have provided the spectrophotometric information on the IRS 13 sources and its environment, from 1 to $4 \mu\text{m}$. The Gemini AO data were calibrated by linear interpolation based on one bright, hot star of the field under study, from the calibrated NICMOS data, between the F160W and F190N photometry for the H band, F190N and F222M for the Kp band. The star detection and photometry was made with the *StarFinder* procedure (Diolaiti *et al.* 2000) for all the images. Specially for the AO images a deconvolution code called MCS (Magain *et al.* 1998) was applied. For the H and the Kp images the width of the synthetic PSF was equal to $0.040''$ and to $0.192''$ for the L-band image, i.e. a gain in resolution respectively of a factor 4.5 in H, 4.3 in Kp and 1.5 in L.

2.2 Spectroscopic data

The only high-spatial resolution images giving spectroscopic information are contained in the NICMOS narrow-band images from the F187N filter. By subtraction of F190N, a narrow-band filter in the nearby continuum, from F187N, a map of the $1.87 \mu\text{m}$ Pa α emission was obtained (Stolovy *et al.* 1999). This map shows the distribution of the ionized gas and stellar spots from Pa α emission in the atmosphere of the hot stars. The Br γ and $2.06 \mu\text{m}$ He I line profile at IRS 13E from BEAR spectro-imagery, an imaging FTS (Maillard 2000), were used as complementary information to help precise the spectral type of the underlying stars. The IRS 13 complex is located in a region of intense interstellar emission. The data cube was particularly useful to correct the two emission line profiles from the interstellar emission, leaving fully resolved stellar profiles respectively at 21.3 and 52 km s^{-1} resolution.

2.3 Proper motions

The proper motions of the IRS 13 sources and the sources contained in the surrounding $2.5'' \times 2.5''$ were obtained from Ott *et al.* (2003) who conducted an analysis of ten years of SHARP data (Eckart *et al.* 1995), providing more than 1000 proper motions in the central parsec.

3 Results

From the deconvolution analysis of the $2.5'' \times 2.5''$ field including IRS 13, 20 individual sources were identified. IRS 13E is decomposed in seven sources, respectively names 13E1, 13E2, 13E3A and B, 13E4, 13E5 and 13E6. The name 13E3A and B is proposed for the two components of the source 13E3 which appears double only after deconvolution, in the H and Kp bands. The positions of all the sources and their proper motions, estimated for most of them, are given in Fig. 1. Their observed photometry in the H, K and L bands is presented in Table 1. In the F187N - F190N image only 13E2 and 13E4 are remaining, indicative that these two sources are emission stars.

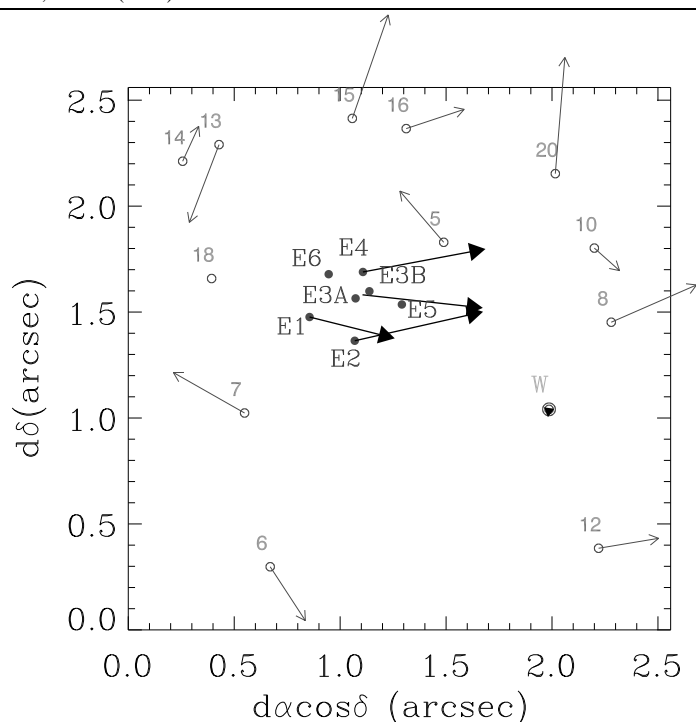


Fig. 1 The IRS 13 field with the star identification. The vector associated with most of the stars represents the amplitude in velocity and the direction of proper motion measured from SHARP data by Ott *et al.* (2003). For E3A and E3B only the barycenter proper motion is determined. The origin of the field corresponds to $-2.19'W$ and $-3.00'S$ with respect to Sgr A*.

From the flux measurements made in 8 bands, between 1.1 and $3.5 \mu\text{m}$, it was possible to obtain a dereddened spectrophotometry of the IRS 13 sources. That supposes to adopt a A_v value and a law of dereddening. From a mean value of 31.1 mag A_v is known to strongly vary with extinction within the central parsecs (Scoville *et al.* 2003). The local value was derived from two constraints: IRS 13W known as a cool oxygen star, and IRS 13E2 and 13E4 as hot stars from Pa α imaging. A value of $A_v = 35$ was adopted and was assumed to be valid over the small field around IRS 13. A_v could be pretty well constrained assuming that IRS 13E2 is a WR star with $T_{eff} > 25,000 \text{ K}$. The IRS 13E2 spectral type is based on the Pa α imaging, but also on Fabry-Pérot spectro-imaging behind the CFHT-AO system where IRS 13E2 is detected as the only source of the broad $2.06 \mu\text{m}$ He I emission line (Clénet *et al.* 2003). With the spectral range under study, from about 1 to $4 \mu\text{m}$, beyond a temperature of $25,000 \text{ K}$ we are in the Rayleigh-Jeans regime, and the shape of the SED becomes constant in a $\log[F(\lambda)]$ versus λ diagram. A_v can be adjusted to bring the data points parallel to the SED. However, the fit of the dereddened data has to be made as the sum of two black-body curves since most of the sources have an infrared excess, signature of thermal dust emission. The adjustments is made with four parameters for each IRS 13 star, by $Coeff_1 \times BB(T_1) + Coef_2 \times BB(T_2)$. The T_1 temperature being the high-temperature component, is mainly determined by the data points between 1 and $2.5 \mu\text{m}$, and T_2 by the 2 to $4 \mu\text{m}$ points. If for the fitting T_1 becomes $\geq 25,000 \text{ K}$ the temperature is set fix. The four final parameters are presented in Table 2. The dereddened points and the fits are shown on Fig. 2. Several stars are very hot stars, i.e. with

a $T_{eff} \geq 25,000$ K. The NICMOS F110M and the L data are essential to give the maximum of constraints to the SED of each source.

4 Nature of the IRS 13E sources

From the main results reported in the previous section an identification of the spectral type of the seven components of IRS 13E can be derived.

Table 1 H, K and L photometry of the IRS 13E cluster and the nearby field stars

ID	<i>H</i>	<i>K</i>	<i>L</i>	<i>H</i> – <i>K</i>	<i>K</i> – <i>L</i>
W	14.51	11.22	8.92	3.29	2.29
E1	12.71	10.90	8.59	1.81	2.31
E2	13.02	10.95	7.73	2.07	3.21
E4	14.34	11.64		2.70	
5	14.28	11.82		2.47	
6	14.68	12.05		2.63	
7	14.38	12.10		2.28	
8	14.82	12.14		2.68	
E3A	16.44	12.38	7.50	4.06	4.89
10	15.51	12.71		2.80	
E3B	16.93	12.98	7.92	3.95	5.06
12	15.89	13.19		2.69	
13	15.91	13.26		2.65	
14	15.91	13.33		2.58	
15	16.61	14.12		2.49	
16	16.62	14.13		2.49	
E5	18.15	14.20	8.48	3.95	5.71
18	16.77	14.43		2.34	
E6	16.20	14.48		1.73	
20	17.26	14.70		2.56	

Table 2 Fitting parameters of the SED of the IRS 13E sources and IRS 13W. The spectral type of each source as discussed in Sect. 5 is summarized in the last column.

Star	<i>Coef</i> ₁	<i>T</i> ₁ K	<i>Coef</i> ₂	<i>T</i> ₂ K	Sp. Type
W	23.00	2600	1700	650	M5III
E1	0.500	\geq 25000	12000	550	O5I
E2	0.450	\geq 25000	40000	550	WC9
E4	0.070	\geq 25000	45	1550	O5IIIe
E3A	0.460	3800	33000	610	d. WR ^a
E3B	0.375	3800	29000	580	d. WR
E5	0.070	6000	9800	630	d. WR
E6	0.008	\geq 25000			O5V

a : dusty Wolf-Rayet star

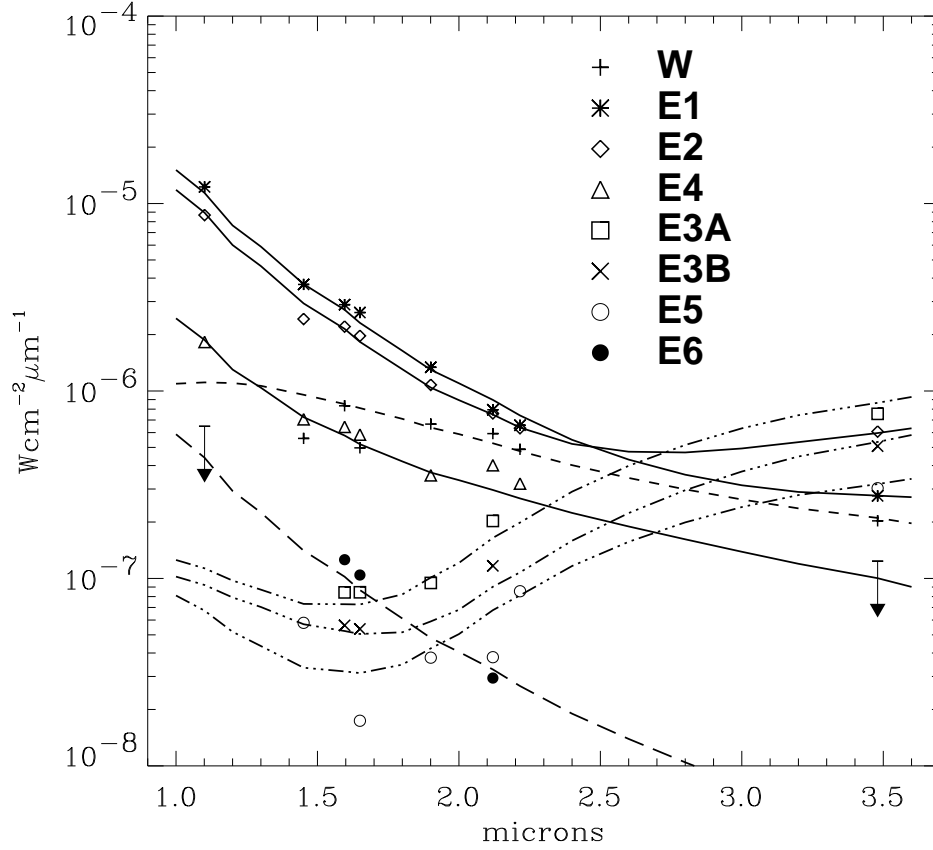


Fig. 2 Dereddened flux in $W \text{ cm}^{-2} \mu\text{m}^{-1}$ for $A_v = 35$. The top of the arrows represents the upper limit of the detectable flux in the $1.1 \mu\text{m}$ and the L-band filters. The various lines represent the best fitting between 1 and $4 \mu\text{m}$ of the data points from a two-component model with the parameters of Table 2.

4.1 13E1, 13E2 and 13E4

The source 13E1 is a bright, blue star, but with no detected emission at $\text{Pa}\alpha$. From its luminosity and its T_{eff} IRS 13E1 is proposed to be close to a O5I main sequence star. 13E2 and 13E4 are two emission line stars, 13E2 being brighter in $\text{Pa}\alpha$ by a factor 2. From the BEAR data, the $2.06 \mu\text{m}$ He I line is a broad line ($\sim 900 \text{ km s}^{-1}$ FWHM) while the $\text{Br}\gamma$ line is narrow ($\sim 215 \text{ km s}^{-1}$ FWHM). 13E2 is reported as the only He I emitter (Clénet *et al.* 2003). As a broad-line, helium-rich star, 13E2 is proposed as a Wolf-Rayet type star, from the criterion on the linewidth developed in Paumard *et al.* (2001). By analogy with similar stars in the central parsec the source should be more precisely a WC9 star. 13E4 is a blue star which shows a narrow emission line in $\text{Pa}\alpha$ but no helium emission line. Therefore, this star is much less evolved than 13E2. It can be proposed as a O5IIIe, since it is weaker than E1 and has hydrogen lines in emission.

4.2 13E3A, 13E3B and 13E5

On Fig. 2 these three stars (dash-dotted lines) have a similar SED. They are adjusted by a strong, cool component at $\simeq 600$ K ($Coef_2$ is high) and a weak, hotter component of a few thousands K. This adjustment can be compared to the fitting of the SED of IRS 21 (Tanner *et al.* 2002) fitted by a two-component model, the near-infrared scattered light from the central source peaking at $\simeq 3.8 \mu\text{m}$ (760 K), and the mid-infrared re-emitted light from a dust shell at ~ 250 K. Tanner *et al.* (2003) conclude that this source is a dusty WR star, experiencing rapid mass loss, and the other red, featureless spectrum sources along the Northern Arm IRS 1W, 2, 3, 5, and 10W, as well. By analogy, we conclude that the three red sources within the IRS 13E complex, also located in the dusty part of the mini-spiral are dusty WR stars.

4.3 13E6

The source IRS 13E6 is another blue star, much weaker than 13E1, 13E2 and 13E4, with $K_{mag} = 14.5$ (Table 1). The image in the L band is not deep enough to detect it at this wavelength to confirm that this star is also embedded in the same concentration of dust than the other IRS 13E sources. From its color and magnitude IRS 13E6 can be considered as close to a O5V type star. Without further indication, only from the fact that all the other stars in IRS 13E are hot stars, we assume that IRS 13E6 belongs also to the same complex.

5 Model of IRS 13E as the remaining core of a massive star cluster

IRS 13E appears as only composed of hot, massive stars, with at least 7 stars within $0.5''$. The common direction and comparable amplitude of the proper motions of the main components is a decisive argument to indicate that 13E1, 13E2, 13E3A/B and 13E4 are physically bounded. The source previously called IRS 13E is likely a compact star cluster. Furthermore, its composition means a young star cluster of a few 10^6 yr old, since several members are identified as having already reached the WR stage.

The presence of such a compact cluster with a limited number of members raises the question of its origin. First, it can be noticed that each component has many other examples of stars of the same spectral type in the central parsecs. However, the large abundance of massive stars, which are very rare elsewhere in the Galaxy, remains one of the major mysteries of this region of the Milky Way. Since star formation would be difficult due to the strong tidal forces from the Sgr A* black hole, Gerhard (2001) made the interesting hypothesis that the central parsec He I stars, the most prominent of the massive young stars, might be the remains of a dissolved young cluster, disrupted in the vicinity of the central black-hole. Kim *et al.* (2003) tested this idea for different cluster masses and different initial orbit radii. They came to the conclusion that some simulations can be regarded as possible candidates for the origin of the central parsec cluster. With its exceptional concentration of massive stars, very close to Sgr A*, all bounded together, we propose that IRS 13E might be the remaining core of such a massive cluster which was disrupted by Sgr A*. The analysis of the 12 other stars identified in the IRS 13 field (Fig. 1) conducted as for the IRS 13E cluster sources, made possible to separate the sources in two categories, 9 red stars (T_{eff} from 2800 to 5000 K) and 3 blue stars ($T_{eff} \geq 25,000$ K). The red stars are members of the most numerous population of the central parsecs, which is an old population of K, M and AGB stars, to which belongs also IRS 13W. The blue stars should be members of the most recent stellar population. On the other hand, the blue stars are comparable in magnitude and color to the stars of the S-cluster (Gezari *et al.* (2002) detected around Sgr A*. The IRS 13E cluster itself contains also one of such lower mass blue stars (Table 2). Hence, the hot stars, including the S and the helium stars, could come from the same initial massive cluster, and complete its IMF. However, more simulations are needed to validate this hypothesis.

Another aspect of IRS 13 is the detection of a discrete X-ray emission within $1''$ positional accuracy (Baganoff *et al.* 2001). IRS 13E as a star cluster might be the X-ray source, by the colliding winds of all the close, hot, mass-losing stars. An example of such a source can be provided by the detection of a

discrete X-ray source at the position of the core of the Arches cluster (Yusef-Zadeh *et al.* 2002). A better astrometry of the X-ray source at IRS 13 could help confirm this assumption, consistent with IRS 13E as the remaining core of a massive star cluster.

References

- Baganoff, F.K., Maeda, Y., Morris, M., Bautz, M.W., Brandt, W.N., Cui, W., Doty, J.P., Feigelson, E.D., Garmire, G.P., Pravdo, S.H., Ricker, G.R., & Townsley, L.K. 2001, *ApJ*, *astro-ph/01002151*
- Cl'enet, Y., Rouan, D., Gendron, E., Montri, J., Rigaut, F., L'ena, P. & Lacombe, F. 2001, *A&A*, 376, 124
- Cl'enet, Y., Lacombe, F., Gendron, E., & Rouan, D. 2003, *these proceedings*
- Diolaiti, E., Bendinelli, O., Bonaccini, D., Close, L., Currie, D. & Parmeggiani, G. 2000, *A&AS*, 147, 335
- Eckart, A., Genzel, R., Hofmann, R., Sams, B.J., & Tacconi-Garman, L.E. 1995, *ApJ*, 445, L23
- Genzel, R., Thatte, N., Krabbe, A., Kroker, H., & Tacconi-Garman, L.E. 1996, *ApJ*, 472, 153
- Gezari, S., Ghez, A.M., Becklin, E.E., Larkin, J., McLean, I.S., Morris, M. 2002., *ApJ*, 576, 790
- Gerhard, O. 2001, *ApJ*, 546, L39
- Graves, J.E., Northcott, M.J., Roddier, F.J., Roddier, C.A., & Close, L.M. 1998, *SPIE*, 3353, 34
- Krabbe, A., Genzel, R., Eckart, A., Najarro, F., Lutz, D., Cameron, M., Kroker, H., Tacconi-Garman, L.E., Thatte, N., Weitzel, L., Drapatz, S., Geballe, T., Sternberg, A., & Kudritzki, R.P. 1995, *ApJ*, 447, L95
- Kim, S.S., Morris, M., & Figer, D.F. 2003, *these proceedings*
- Maillard, J.P., 2000, in *Imaging the Universe in 3 Dimensions*, ed. E. van Breughel & J. Bland-Hawthorn, *ASP Conf. Ser.*, 195, 185
- Maillard, J.P., Paumard, T., Stolovy, S., & Rigaut, F. 2003, *A&A*, *submitted*
- Magain, P., Courbin, F. & Sohy, S. 1998, *ApJ*, 494, 472
- Ott, T., Genzel, R., Eckart, A., & Schödel, R. 2003, *these proceedings*
- Paumard, T., Maillard, J.P., Morris, M., & Rigaut, F. 2001, *A&A*, 366,466
- Simon, M., Chen, W.P., Forrest, W.J., Garnett, J.D., Longmore, A.J., Gauer, T., & Dixon, R.I. 1990, *ApJ*, 360, 95
- Scoville, N.Z., Stolovy, S.R., Rieke, M., Christopher, M., & Yusef-Zadeh, F. 2003, *these proceedings*
- Stolovy, S.R., McCarthy, D.W., Melia, F., Rieke, G., Rieke, M.J., & Yusef-Zadeh, F. 1999, in *The Central Parsecs of the Galaxy*, ed. H. Falcke, A. Cotera, W.J. Duschl, F. Melia, M.J. Rieke, *ASP Conf. Ser.*, 186, 39
- Tanner, A., Ghez, A.M, Morris, M., Becklin, E.E., Cotera, A., Ressler, M., Werner, M., & Wizinovitch, P. 2002, *ApJ*, 575, 860
- Tanner, A., Ghez, A.M, Morris, M., & Becklin, E.E. 2003, *these proceedings*
- Yusef-Zadeh, F., Law, C., Wardle, M., Wang, Q.D., Fruscione, A., Lang, C.C., & Cotera, A. 2002, *ApJ*, 570, 665
- Zhao, J.H., & Goss, W.M. 1998, *ApJ*, 499, L163

Annexe E

Article « Kinematic and structural analysis of the Minispiral in the Galactic Center from BEAR spectro-imagery »

Kinematic and structural analysis of the Minispiral in the Galactic Center from BEAR spectro-imagery[★]

T. Paumard¹, J.P. Maillard^{★★1}, and M. Morris²

¹ Institut d'Astrophysique de Paris (CNRS), 98b Blvd Arago, 75014 Paris, France

² University of California, Los Angeles, Div. of Astronomy, Dept of Physics and Astronomy, Los Angeles, CA 90095-1562, USA

Received ;date; / Accepted ;date;

Abstract. Integral field spectroscopy of the inner region of the Galactic Center, over a field of roughly $40'' \times 40''$ was obtained at $2.06 \mu\text{m}$ (He I) and $2.16 \mu\text{m}$ (Brackett- γ) using BEAR, an imaging Fourier Transform Spectrometer, at spectral resolutions respectively of 52.9 km s^{-1} and 21.3 km s^{-1} , and a spatial resolution of $\approx 0.5''$. The analysis of the data was focused on the kinematics of the gas flows, traditionally called the ‘Minispiral’, concentrated in the neighborhood of the central black hole, Sgr A*. From the decomposition into several velocity components (up to four) of the line profile extracted at each point of the field, velocity features were identified. Nine distinguishable structures are described: the standard Northern Arm, Eastern Arm, Bar, Western Arc, and five additional, coherently-moving patches of gas. From this analysis, the Northern Arm appears not limited, as usually thought, to the bright, narrow North-South lane seen on intensity images, but it instead consists of a weak, continuous, triangular-shaped surface, drawn out into a narrow stream in the vicinity of Sgr A* where it shows a strong velocity gradient, and a bright western rim. The Eastern Arm is split into three components. An Eastern Cavity proposed on radio maps is not confirmed, but a new ISM feature is detected just east of its position, the *Eastern Bridge*, that seems to be a new flow. We also report absorption of ISM structures by others, providing information on their relative position along the line of sight. A system of Keplerian orbits can be fitted to most of the Northern Arm, and the bright rim of this feature can be interpreted in terms of line-of-sight orbit crowding as being formed by the warping of the flowing surface at the western edge facing Sgr A*. These results lead to a new picture of the gas structures in Sgr A West, in which large-scale gas flows and isolated gas patches coexist in the gravitational field of the central Black Hole. The question of the origin of the ionized gas is addressed and a discussion of the lifetime of these features is presented.

Key words. infrared – spectro-imaging – FTS – Galaxy: Center – Sgr A West – ionized gas

1. Introduction

Within the inner 2 pc of the Galactic Center (GC) lies the Sgr A West region, dominated by ionized gas which, because of high obscuration along the line of sight, has been detected only at infrared and radio wavelengths. Infrared fine-structure line emission of [Ne III] at $12.8 \mu\text{m}$ has been used to map the gas distribution a number of times, with successively higher spatial sampling and spatial and spectral resolutions, up to $0.6'' \times 1.0''$ sampling, $\approx 30 \text{ km s}^{-1}$ and $2''$ resolution in the most recent paper (Lacy et al. 1991). In parallel, observations with the Very Large Array (VLA) telescope provided a 6-cm map of the ionized gas in the radio continuum at $1''$ resolution (Lo & Claussen 1983). Later, Roberts & Goss (1993) observed the Sgr A West

complex in the radio recombination H92 α line at 3.6 mm (8.3 GHz), also at a resolution of $1''$. Much higher spatial resolution was reached with the VLA at 13 mm, with a beam size of $0.15'' \times 0.10''$, in the course of a project to measure proper motions of the bright, compact blobs of ionized gas (Zhao & Goss 1998). Also, with the NICMOS cameras on board HST, the Pa α line was observed at a spatial resolution of $0.18''$ (Scoville et al. 2003, these data will be used in this paper for comparison purposes).

Bry at $2.166 \mu\text{m}$ has also been used to trace the ionized gas. The first detection consisted of a grid of spectra around IRS 16 (Geballe et al. 1991) which could not give an overview of the emission morphology. The availability of near-infrared arrays has resulted in many images of the Galactic Center. However, the ionized gas can only be detected by spectro-imaging or by narrow-band imaging on a strong emission line. Broad-band images, for example in the K band, are dominated by the stellar content. A first attempt of spectro-imagery in Bry was made by Wright et al. (1989) with a Fabry-Perot system scanned over $\approx 1000 \text{ km s}^{-1}$, at a modest spectral resolution of 90 km s^{-1} on

Send offprint requests to: J.P. Maillard, e-mail: maillard@iap.fr.

[★] Data available online at CDS (<http://cdsweb.u-strasbg.fr/>), see Sect. 5.5.

^{★★} Visiting Astronomer, Canada-France-Hawaii Telescope, operated by the National Research Council of Canada, le Centre National de la Recherche Scientifique de France and the University of Hawaii.

a $38'' \times 36''$ field. The data cube obtained in the same line with BEAR, an Imaging Fourier Transform Spectrometer on the Canada-France-Hawaii telescope represents a significant effort to cover most of the central ionized region with a much better spectral resolution (FWHM 21.3 km s^{-1}), at seeing-limited resolution. A preliminary analysis was presented by Morris & Maillard (2000). Data from the same instrument were obtained on the $2.06 \mu\text{m}$ He I line, leading to the first identification of interstellar Galactic center gas in this line (Paumard et al. 2001, hereafter Paper I). Data were also obtained with NIRSPEC on Keck II, by scanning the field with the $24''$ slit used in a north-south orientation to obtain a spectral cube covering $1.98 \mu\text{m}$ to $2.28 \mu\text{m}$ at resolution of $\approx 21.5 \text{ km s}^{-1}$ (Figer et al. 2000).

All these data show that the ionized gas in the inner few parsecs of the Galactic Center is organized, in projection, into a spiral-like morphology having several apparent ‘‘arms’’. This has led to the widespread appellation, ‘‘Minispiral’’ for this entire pattern. The brightest features are named ‘‘Northern Arm’’, ‘‘Eastern Arm’’, ‘‘Bar’’, and ‘‘Western Arc’’, as if imitating the morphology of a very small spiral galaxy. These terms seem to imply that the ionized filamentary structures constituting Sgr A West either form spiral patterns, or are portions of spiral arms. This view was motivated by the gas dynamical study carried out by Lacy et al. (1991), who interpreted the [Ne II] data in terms of a one-armed linear spiral in a Keplerian disk. The kinematics derived from all these data were also very useful in constraining the enclosed mass.

The various features of Sgr A West give a spiral appearance primarily because of the way they are superposed on each other. However, a new analysis of Lacy’s data was conducted by Vollmer & Duschl (2000) to re-examine the kinematic structure of the ionized gas. Using a three-dimensional representation they confirm the standard features, but with a more complex structure, including two features for the Eastern Arm: a vertical finger of high density and a large ribbon extending to the east of Sgr A*, and two distinctly different components in the Bar. Data in different lines, at better spectral and spatial resolution, warrant an independent kinematic analysis. The ionized gas is one component among the constituents that coexist within the central deep well of gravitational potential created by the black hole candidate (Sgr A*) of a mass equivalent to several million solar masses, with the compact cluster of young stars, the surrounding population of evolved stars and the ring of molecular gas. All these constituents orbit around the central dark mass. However, a consensus concerning its mass does not seem to have been emerged yet: assuming a distance of 8 kpc (Genzel et al. 2000), Ott et al. (2003) give a mass of $2.9 \pm 0.2 \times 10^6 M_{\odot}$, whereas Ghez et al. (2003) give $4 \pm \times 10^6 M_{\odot}$. Developing a detailed picture of these components will improve our understanding of the interaction of all these components in the Galactic Center. The current analysis completes the work made from similar data on the central cluster of young, helium stars presented in Paper I and updated in Paumard et al. (2003).

In the present paper, the gas content in the inner region of the GC is presented and analyzed from high spectral resolution data cubes on the Br γ and the He I $2.06\text{-}\mu\text{m}$ line, obtained with BEAR. The He I data are from a new data cube (larger

field, improved spectral resolution) compared to the data used in Paper I. A multi-component line fitting procedure applied to the emission-line profiles in each point of the field is described in Sect. 3. It was used first on the Br γ cube and then on the He I cube. From this decomposition in Br γ , the identification of defined gas structures comprising the whole Sgr A West ionized region is presented in Sect. 4. A comparison between the decompositions in Br γ and He I is presented in Sect. 4.3. Attempts to adjust Keplerian orbits to the flowing gas are presented in Sect. 5, which contains in Sect. 5.5 a discussion of the implication of these identifications for the formation and the lifetime of the inner ionized gas.

2. Observations and preparatory data reduction

The 3-D data analyzed in the paper were obtained during two runs with the BEAR Imaging FTS (Maillard 1995, 2000) at the f/35 infrared focus of the 3.6-m CFH Telescope. In this mode, a 256×256 HgCdTe facility camera is associated with the FTS, in which several narrow-band filters are selectable. Two of them were used, one which contains the Br γ line (4616.55 cm^{-1} , bandpass $4585 - 4658 \text{ cm}^{-1}$) and the other one centered on the He I line at 4859.08 cm^{-1} (bandpass $4806 - 4906 \text{ cm}^{-1}$). The field of view of the instrument is circular, with a diameter of $24''$. The Br γ data were acquired in July 25, 26, 1997 (UT) by observing two overlapping fields in order to cover most of a field of $40' \times 28''$, oriented in the East-West direction, centered on the position of Sgr A* (Fig. 1). The raw data consist of cubes of 512 planes with an integration time of 7 s per image. From the maximum path difference which was reached, the corresponding limit of resolution (FWHM) in velocity is equal to 21.3 km s^{-1} .

On the following night a single field centered on Sgr A* was recorded with the $2.058 \mu\text{m}$ He I filter. The analysis of the later high resolution data was reported in Paper I, which brought new results on the central cluster of massive, hot stars, and led to the detection of the Minispiral in helium. However, the field was not large enough for a significant areal coverage of the Minispiral. New observations through the same filter were therefore obtained on June 9, 10, 11, 2000 in order to get three overlapping circular fields covering, when merged, most of a total field of $36' \times 36''$, also centered on Sgr A*. The estimated width of the interstellar $2.058\text{-}\mu\text{m}$ line in Paper I called for an improved spectral resolution. A value of $\approx 50 \text{ km s}^{-1}$ (exactly FWHM 52.9 km s^{-1}) was chosen instead of 74 km s^{-1} in the previous data, not as high as for Br γ , since the line is weaker. The raw data consist of cubes of 401 planes with an integration of 20 s per image, double the time for the previous data, to improve the detection depth.

The processing of the BEAR data was presented in Paper I; the main steps are standard cube reduction, atmospheric OH correction and correction of filter transmission and telluric absorption — particularly important for the $2.06\text{-}\mu\text{m}$ data. The OH correction was more difficult for the Br γ data and for the new He I data because of the higher spectral resolution and the better signal-to-noise ratio, making the OH lines stronger and the sidelobes of the profile more extended. The next step is the generation of the *line cubes*, spectral cubes in which the con-

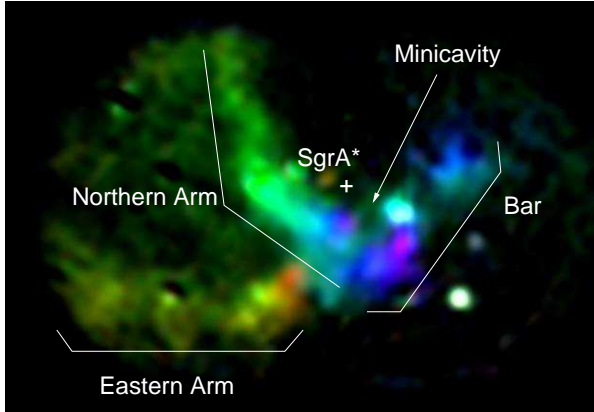


Fig. 1. Three color image of the two mosaicked fields of Sgr A West observed with BEAR in Br γ , between -350 (purple) and $+350$ km s $^{-1}$ (red). The standard bright features, Northern and Eastern Arms, Bar, and the Minicavity, are indicated. Also, a few emission line stars show up as bright points in the image.

tinuum level in each point of the field is fitted and subtracted, in order to keep only the emission lines. The separation of stars and gas was not applied to the Br γ cube since the interstellar medium (ISM) dominates the Br γ emission. It had to be applied to the He I data, as explained in Paper I. The merging of the line cubes from different data acquisitions required a new procedure to generate the final line cube of the full field. As an illustration, Fig. 1 was obtained from the Br γ merged cube with *cubeview for Yorick*, a port to the Yorick interpreted language of the facility program specially developed under IDL to examine the BEAR data cubes (Maillard 2000).

The Br γ line cube is dominated by the emission from the interstellar medium (ISM), but a thorough inspection with *cubeview* shows that some stars exhibit the Br γ line in emission (Fig. 1). On the contrary, in the He I line cube the stellar emission from the hot stars predominates (Paper I), but the ISM emission is clearly detected too, with a better contrast, thanks to the higher spectral resolution.

The central parsec was observed with NICMOS cameras onboard HST, during a few runs between Aug. 1997 and Aug. 1998, in 6 near-IR filters, including 2 narrow-band filters, F187N centered on $1.87 \mu\text{m Pa}\alpha$, and F190N, the nearby continuum. By subtracting the F190N filter from the other one, Pa α emission was obtained on a field of $19' \times 19'$ centered on Sgr A* (Stolovy 1999, Scoville et al. 2003) at a spatial resolution of $0.18''$, and a wider field of $\approx 120''$ at a lower resolution of $\approx 0.4''$. We use an image covering the central $40'' \times 40''$ field from these data for the purpose of comparison, in Fig. 12.

3. Structure identifications

At each point of the field the Br γ emission profile generally appears complex. The basic assumption which is made is that each observed profile results from the combination of several velocity components, that is, that along any given line of sight several flows are superposed. The first goal of the present paper

is to separate these various flows and to describe them independently from each other. For this purpose, the development of a multi-component line fitting procedure able to work on 3D data appeared to be absolutely required. From a coarse examination of the datacube with *cubeview*, fitting with a maximum of four distinct velocity components along each line of sight seemed adequate.

A comparison of the velocity components from one line of sight to the next should usually reveal coherent velocity structures by continuity. In the end, it might be possible to conclude whether these structures are isolated, or form continuous flows. Thus, the process is split into two main parts: first the line profile decomposition at all the points of the field, and second, the structure identification. However, these two steps must be conducted iteratively in order to take full advantage of the 2D information in the cube. This work is based on original software developed by Miville-Deschênes (personal communication), which we have largely extended.

3.1. Line profile decomposition

3.1.1. Line profile

A single velocity component of the emission lines from the ISM has been assumed to be Gaussian, given as a function of v by :

$$I(v) = I_0 \exp\left(-\frac{(v-v_0)^2}{2\Sigma^2}\right)$$

where I_0 is the amplitude of the Gaussian expressed in $\text{erg} \cdot \text{s}^{-1} \cdot \text{cm} \cdot \text{pixel}^{-1}$ (1 pixel = 0.125 arcsec^2), v_0 is the radial velocity of the component, and Σ the width of the line, due to thermal agitation, turbulence and any velocity gradient along the line of sight. The total flux per pixel of the line is then:

$$\phi = \sqrt{2\pi} \frac{\Sigma I_0 \sigma_0}{c}$$

where c is the velocity of light and σ_0 the rest wavenumber of the studied line. The full width at half maximum (FWHM) of the line is given by:

$$\text{FWHM} = 2\Sigma \sqrt{2 \ln 2}$$

The detected spectrum is convolved by the instrumental line shape (ILS) of the FTS, which is by definition a sinc function defined by:

$$\psi(v) = \frac{\sin \pi \delta_m \frac{v\sigma_0}{c}}{\pi \delta_m \frac{v\sigma_0}{c}}$$

where δ_m is the maximum path difference between the two arms of the interferometer, that determines the limit of resolution $d\sigma$ of the data with $d\sigma = 0.6/\delta_m$ (FWHM).

The measured line profile is thus the convolution product $S = I * \psi$, function of three free parameters I_0 , Σ and v_0 . Each single spectrum of the field has been fitted to a set of four such lines, thus implying twelve free parameters.

3.1.2. Procedure

The fitting routines use MPFIT¹, a general purpose fitting engine written in IDL. It has been preferred to the standard IDL fitting procedure because of its greater robustness and because of its versatile interface that allows one to set complex constraints on the variables. The whole procedure is divided into several steps, detailed below.

Preparation: As for any fitting routine, a reasonable initial guess must be provided for each point of the field. For such a problem, where we intend to fit complex line profiles at low signal-to-noise, the method cannot be fully automatic. The method consists of determining an initial guess only for a few points, and letting the software determine initial guesses for the other points from these, as we will see in the next paragraph.

Good initial guess are chosen for a few starting points in the field, selected by the user for their high signal-to-noise associated line profiles and unambiguous decomposition. The user decides the optimum number of starting points and their locations. However, they should be chosen so that every structure in the field is represented, and the most complex regions are better fitted if they are close to a starting point. In our case, five starting points were used.

Step 1: From the starting points, a first procedure attempts to fit a four-component line shape function to each spectrum. For each new spectrum, the initial guess is determined from the results found for the neighboring points. The spectra are studied sequentially in parallel spiral-mode scanings around each starting point. Except for the initial guess, the fitting of a spectrum is independent of all the others.

Step 2: The velocity structures are then built. For the brightest point of the field, the neighbors are examined, and searched for a component such that the velocity gradient between the point of interest and this neighbor is less than a certain amount, which is set by the user at runtime. The procedure is iterative, and once a few neighbors have been selected into a structure, their neighbors are in turn examined for possible selection. The procedure stops when every component of every point of the field has been assigned to exactly one spatial structure. This procedure allows only one component of a given point to be selected into a given structure. A structure that overlaps itself spatially, thus causing two velocity components on the same line of sight, cannot be directly detected as such: the program splits it into two structures.

Step 3: This procedure requires that the detected structures be manually inspected. The user has then the possibility to add some more common sense heuristics into the structure identification, a little difficult to implement but easy to apply manually. Several problems can occur:

- during step 1, the fitting procedure might fit only one component where two blended components are indeed more appropriate,
- during step 2, if two overlapping structures intersect each other in the α - δ -velocity space, the procedure can

Table 1. Common names of the narrow (N) and broad (B) line stars drawn on Fig 3 (see Paumard et al. 2003, and references therein).

ID	Name	ID	Name	ID	Name
N1	IRS 16NE	B1	ID 180	B7	AF
N2	IRS 16C	B2	IRS 7E2	B8	AFNW
N3	IRS 16SW	B3	IRS 9W	B9	HeIN3
N4	IRS 16NW	B4	IRS 15SW	B10	BSD WC9
N5	IRS 33SE	B5	IRS 13E2	B11	IRS 29N
N7	IRS 34W	B6	IRS 7W	B12	IRS 15NE
				B13	IRS 16SE2

falsely cross-connect them, i.e. reconstruct two structures, each one being made of parts of both physical structures (Fig. 2).

Step 4: Then, these manually corrected results are used to perform a second fit at each point of the field; at this point, 2D information is entirely included in the initial guess provided to the fitting procedure.

Iteration: Steps 2, 3 and 4 must be iterated a number of times, until a stable set of plausible structures is reached. ‘‘Plausible structures’’ means only that the structures are more extended than the spatial resolution, and brighter than the detection limit of the data.

4. Results

4.1. General description of the results

The analysis described above leads to a vision of the Minispiral more complex than usually thought, one which is consistent with, but more detailed than the description proposed by Vollmer & Duschl (2000). After a careful examination we identify 9 components of various sizes, labeled (a) to (i). The radial velocity maps of the structures are presented in Appendix A, and their flux maps in Appendix B. Two types of velocity map appear, some with a significant overall velocity gradient, others without any appreciable, large-scale velocity gradient. The deviation from mean motion, defined as the local difference between the velocity measured at one point and the mean value for the neighboring points, and divided by the uncertainty, ranges from roughly one tenth to ten for all the features, which means that every velocity structure shows significant (over 3σ) local features.

The areal size of the structures (Table 2), expressed in terms of solid angle covered on the sky, ranges from 17 arcsec² to 300 arcsec² for the part of the Northern Arm that is visible in the BEAR field of view. The surface area of each structure must be considered as a lower limit because BEAR may not detect the weakest parts nor parts where blending with a brighter structure in the spectral domain prevents detection, and because the field of view does not cover the entire Minispiral.

4.2. Morphology of the ionized gas in Sgr A West

A brief description follows for each identified velocity structure whose velocity maps are given in Figs A.1 to A.9. Table 2 gives the surface coverage on the sky (within the BEAR field

¹ <http://cow.physics.wisc.edu/~craigm/idl/fitting.html>

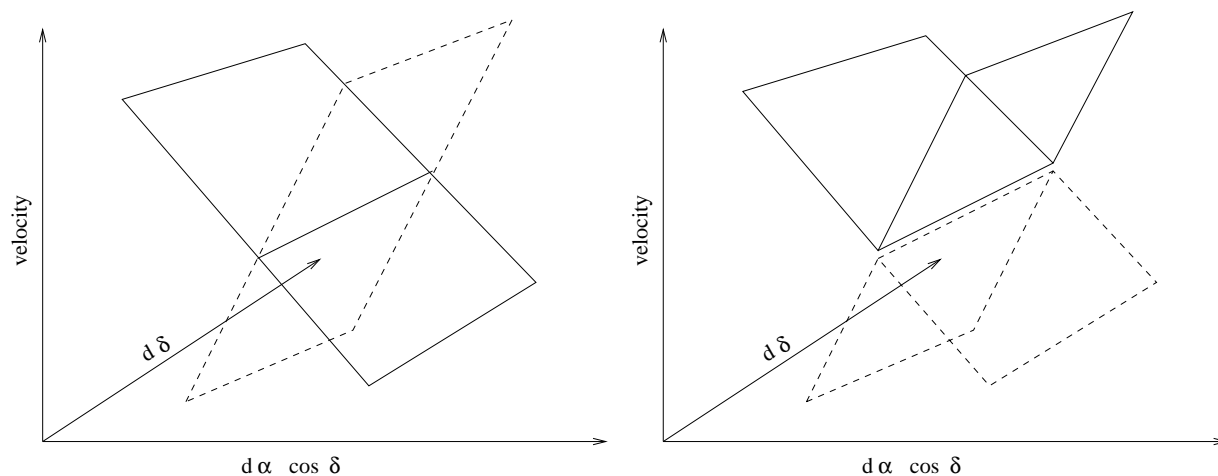


Fig. 2. Cross-connection problem. Left: two physical structures (solid and dashed polygons) intersect each other in the α - δ -velocity space. Right: the structures reconstructed by the software can be erroneous.

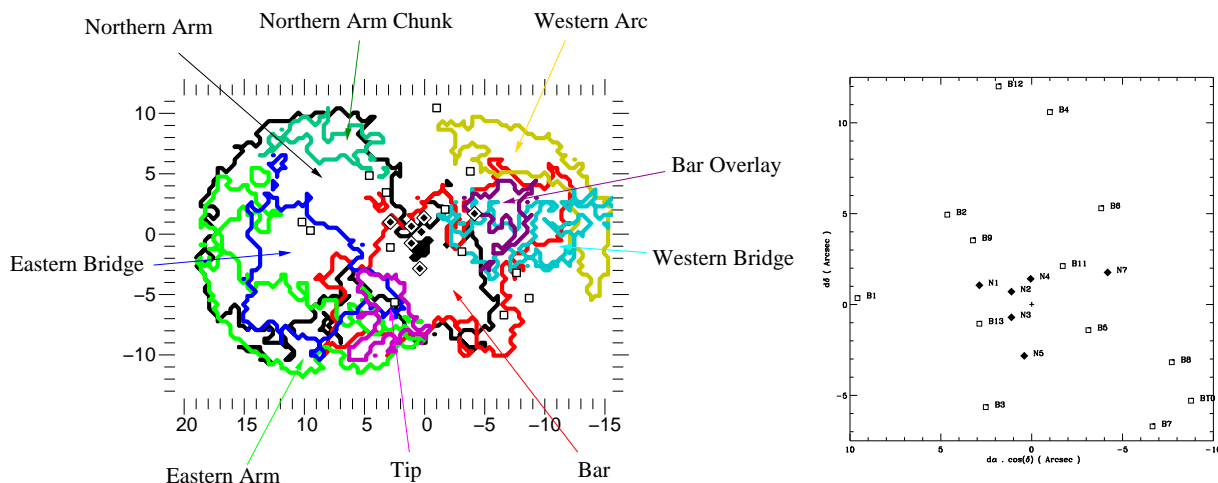


Fig. 3. Left: outline of every structure. The region filled in black corresponds to the points where two lines associated with the Northern Arm are detected (see text). Filled diamonds (resp. empty squares) represent narrow (resp. broad) line helium stars. Right: IDs of the helium stars (adapted from Paumard et al. 2003). See Table 1 for common names identification.

of view), and the maximum and minimum velocity within the given structure.

a) *Northern Arm*: Contrary to its standard description, the Northern Arm is not seen here as a bright N-S lane, but as an extended, triangular surface. One edge of this triangle is the bright rim generally noticed, but it extends all the way over to the Eastern Arm. The third edge of the triangle is the edge of the field, so viewing this feature on a larger field may yield a somewhat different description. As it reaches the Minicavity, the Northern Arm is split into two layers in the spectral direction. Both layers are clearly detected only for a few adjacent pixels (14), that correspond to the small finger-looking feature north-east of the Minicavity. The main layer contains all the Minicavity, while the second layer seems to be deflected northward of the Minicavity, and forms the small finger between the two helium stars

IRS 16SW (N3) and IRS 33SE (N5, Fig. 3). It extends further away on $\approx 5''$ to the north-west, and contains the point-like feature just above the aperture of the Minicavity. On the few pixels where both features are detected, the secondary layer is $50\text{--}80\text{ km s}^{-1}$ more blueshifted than the main one. On the velocity maps, both layers are drawn, indicating the velocity of the secondary one for the few points where both were detected. The flux map gives the sum of the two layers. The direction of the Northern Arm motion (from north to south) has been established by Yusef-Zadeh et al. (1998). The kinematics of the Northern Arm will be thoroughly studied in Sect. 5.

b) *Bar*: The Bar is the most complex region, where at least three components are superimposed. The most important feature is very extended – from the Ribbon of the Eastern Arm (c) to the Western Arc (e) – is very straight, and shows a smooth overall velocity gradient. Vollmer & Duschl

Table 2. Feature identifications, with surface areas (pixels and square arcseconds), and minimum and maximum radial velocities (km s^{-1}).

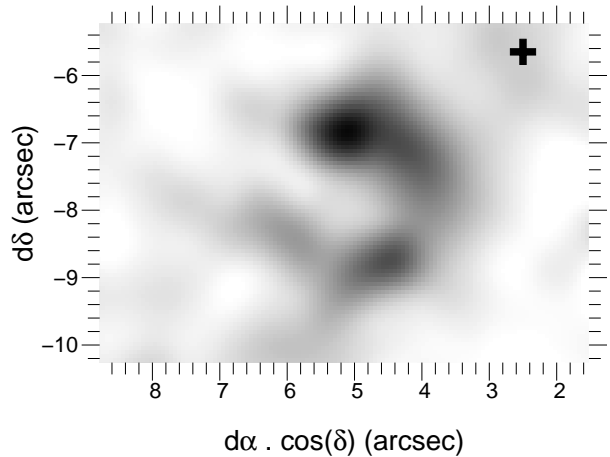
ID	Feature name	S (pix)	S (arcsec ²)	Vmin	Vmax
a	Northern Arm	2414	300.8	-286.9	188.9
b	Bar	1389	173.1	-211	196.9
c	Ribbon	833	103.8	132.9	242.9
d	Eastern Bridge	670	83.5	34.9	182.9
e	Western Arc	471	58.7	-37.1	74.9
f	Western Bridge	327	40.7	-121.1	100.9
g	Tip	207	25.8	222.9	339.0
h	Northern Arm Chunk	185	23.1	14.9	74.9
i	Bar Overlay	136	16.9	-267.0	-7.1

(2000) mention two complementary components of the Bar, which they call Bar 1 and Bar 2, though their description is not sufficient to determine precisely the positions of these two suggested components. We see two additional features, which we propose to call the *Western Bridge* (f) and *Bar Overlay* (i). Parts of the Bar are also superimposed on almost every other structure, including the Ribbon of the Eastern Arm (c), the Tip (g), the Eastern Bridge (d) and the Northern Arm (a).

- c) *Ribbon*: As already described by Vollmer & Duschl (2000), the Eastern Arm region is split into two parts: a *Ribbon* and a *Tip* (g). The velocity gradient of the Ribbon is directed along the minor axis of the structure, not along its major axis as expected for a fbw.
- d) *Eastern Bridge*: A structure of medium size extends from the Ribbon (c) to the bright rim of the Northern Arm. It does not show any large-scale velocity gradient, and its shape does not show any principal axis that would indicate a fbw. It is superimposed on the faint regions of the Northern Arm, and partly superimposed on the Ribbon, the Bar and the Tip. Its southern side is parallel to, as well as superimposed upon, the Ribbon; the two structures are probably related, although their relative velocities differ by more than 50 km s^{-1} . The name we propose is based on the fact that it lies between the two Arms of the Minispiral, both in the spatial and spectral dimensions, being hard to distinguish in the spectral dimension from the Ribbon on its southern side and from the Northern Arm on its northern side. It is also inspired by the fact that the most luminous part of it in our field is a small vertical bar, seemingly connecting the bright parts of the Northern and Eastern Arms. However, the Pa α map (Fig. 12) shows that this bar may extend outside our field-of-view into an elongated feature parallel to the Ribbon. The lack of an overall gradient in the velocity map suggests that this feature is not much affected by shear.
- e) *Western Arc*: The Western Arc lies just at the edge of the field, so we have access only to its innermost part. It is seen as a rather simple feature, with large scale velocity gradient. It is superimposed on the Western Bridge on a few pixels. The velocity field that we measure is basically in good agreement with that of Lacy et al. (1991).
- f) *Western Bridge*: The Western Bridge is a tenuous, elongated feature oriented east-west and extending from the Bar to

the Western Arc. This structure, as well as the Bar and the Bar Overlay (i) upon which it is superimposed, contains in projection the helium star IRS 34W (N7, Fig. 3).

- g) *Tip*: The Tip is, in projection, a very concentrated and relatively small object with the most redward velocity in the region ($\approx 300 \text{ km s}^{-1}$). The Tip has already been noticed by Vollmer & Duschl (2000) only on a morphological basis, as a finger-looking feature of the Eastern Arm in their three dimensional data. Here, we see that the Ribbon and the Tip are two distinct features, superimposed on the line of sight, thus we do not adopt the representation-dependent denomination ‘Finger’. At the elbow between the Ribbon and the Tip, in the IRS 9W region, is a bubble-like feature, or a *Microcavity* (radius $\approx 1''$), with a rather bright rim (Fig. 4), which appears at a specific velocity (230 km s^{-1}).

**Fig. 4.** Microcavity feature in the region of IRS 9W, represented by the black cross. Axes are offsets from Sgr A*. Integrated velocity range: 220–240 km s^{-1} .

- h) *Northern Arm Chunk*: A small tenuous structure is seen superimposed on the Northern Arm, a few arcseconds north of IRS 7. It lies at the edge of our field, so it could extend further out; however the Pa α image shows a small, horizontal bar at its location, crossing the bright rim of the Northern Arm, that does not seem to be much extended.

i) *Bar Overlay*: The Bar Overlay looks like a small cloud that is superimposed upon the western region of the Bar and that shows a velocity gradient similar to the one of the main Bar at the same location, with an offset of $\approx -40 \text{ km s}^{-1}$. It may indicate that these two features are closely related. They could, for example, be the two faces of a single neutral cloud, ionized by two distinct UV sources.

In our nomenclature, no feature is named Eastern Arm. This is because the region is far too complex, and calling one of the feature by this historical name would lead to confusion, thus we reserve this name to the entire region, which indeed comprises the Ribbon, the Tip, and the Eastern Bridge. As already discussed, the Tip and the Ribbon seem to be two parts of an entity, separated by the Microcavity. The Eastern Bridge seems related to this entity, it may belong to it, or be interacting with it.

4.3. Comparison with He I data

The same work of decomposition into velocity structures has been performed on the He I data. It was more difficult than for the Bry data since the spectral resolution and signal-to-noise ratio are lower. The fact that the He I data are dominated by the emission from the helium stars also contributes to the greater complexity of this task. Thus we skipped the first step of the decomposition process, and provided directly a complete set of initial guesses based on the Bry results, since at first sight the distribution of ionized gas is globally the same in He I. This method prevents the He I analysis from being fully independent, although steps 2, 3 and 4 were performed eight times, until the procedure converged satisfactorily.

The Minispiral is detected, as are all of the individual structures, except the Northern Arm Chunk. However, as will be detailed below, several differences in the appearance of these structures are noticeable. In order to quantify these differences, we have built $[\text{He I}]/[\text{Bry}]$ line ratio maps for each structure, normalized to the areal mean for this ratio over the union of all the structures. The $[\text{He I}]/[\text{Bry}]$ line ratio varies considerably across the field, so that, for instance the Northern Arm bright rim and the Minicavity do not show the same shape in He I and Bry (Fig. 5). These differences will be detailed later. Table 3 shows the mean normalized $[\text{He I}]/[\text{Bry}]$ line ratio for the different structures. It appears that this ratio is lower than the mean value for the main, well known features the Northern Arm, The Ribbon, the Bar and the Western Arc, and higher for the smaller features. However, the values are computed only for the features detected in both Bry and He I, so they do not take into account the faintest, least excited regions of each feature. Below are summarized the most noticeable differences between the He I and Bry images of the Minispiral structures.

a) Though the Northern Arm remains the most prominent feature of the Minispiral, the mean value of its normalized $[\text{He I}]/[\text{Bry}]$ line ratio (Minicavity excluded) is one of the lowest, with a value of ≈ 0.74 , being only higher than the value measured for the small part of the Western Arc that we detect. Considering that the faintest parts of the

Table 3. $[\text{He I}]/[\text{Bry}]$ for the different structures, relative to the mean value $\langle [\text{He I}]/[\text{Bry}] \rangle$. The Minicavity is separated from the Northern Arm, as it warrants special attention.

ID	Feature name	$[\text{He I}]/[\text{Bry}]^a$
a	Northern Arm ^b	0.74
	Minicavity	0.85
b	Bar	0.99
c	Ribbon	0.78
d	Eastern Bridge	1.09
e	Western Arc	0.52
f	Western Bridge	1.73
g	Tip	2.64
h	Northern Arm Chunk	–
i	Bar Overlay	1.81

^a normalized to its mean value

^b except Minicavity

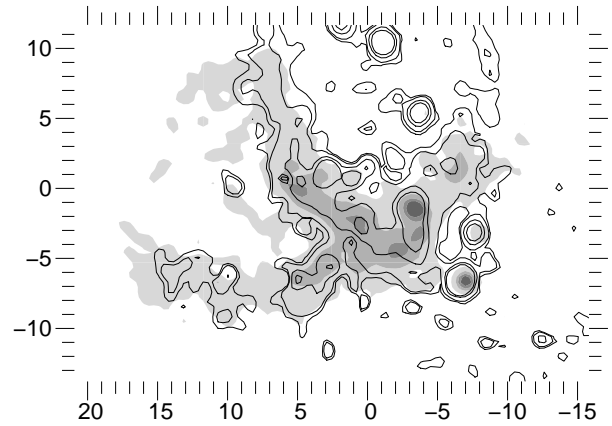


Fig. 5. Comparison between integrated flux in Bry (grey scale) and He I (empty contours). Axes are offsets from Sgr A* in arcsec.

Northern Arm are not detected in He I, this value may be even smaller. The line ratio is higher on the western side of the bright rim, and this rim has in He I the shape of a part of a circle surrounding the IRS 16 cluster. This circle continues further to the northwest, forming a rather faint horn at the location where, in Bry, the rim bends abruptly ($5''$ to the north and $5''$ to the east of Sgr A*, spot C on Fig. 12). The open ring of ionized gas surrounding the Minicavity is on average brighter in He I than the rest of the Northern Arm relatively to the intensity distribution in Bry. Its innermost border is even brighter. Its western edge, where IRS 13 and IRS 2 lie, is very bright, and looks like a vertical bar going from IRS 13 almost to the declination of the AF star, making the Minicavity look angular.

b) The Bar is the main feature with the highest $[\text{He I}]/[\text{Bry}]$ ratio, with a normalized value of 0.99. However, we do not detect helium towards the full extent of its Bry counterpart.

d) The Eastern Bridge (Fig. 6) is clearly identified, but it presents a shape much different from the one observed in Bry. It is brighter on its southern side, and the northern parts are not detected by the procedure. The southern

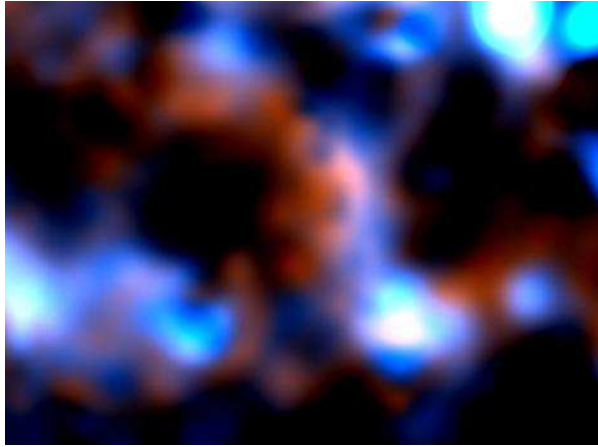


Fig. 6. Composite image of the Eastern Bridge, from images integrated from 50 to 100 km s⁻¹ in the Br γ (red) and He I (blue) cubes.

parts extend horizontally, following the edge of the Eastern Arm Ribbon upon which it is superimposed, with a velocity offset between the Eastern Bridge and the Ribbon of about -50 km s⁻¹ (measured in Br γ , but the agreement in good between the two lines), which again suggests that the two features are related. The bow-shaped bright rim of the structure, which is almost vertical and give its name to the Eastern Bridge, is offset by about 1'' towards west in He I relatively to Br γ .

- e) A small part of the Western Arc is detected within our field; its [He I]/[Br γ] value is the smallest, but only a few points are detected both in He I and Br γ .
- g) Due to the lower spectral resolution of the He I data (52.9 km s⁻¹, vs. 21.3 km s⁻¹ in Br γ), the Tip is not separated from the Ribbon by our procedure in this band. However, it is clearly seen. It is the brightest feature relative to its Br γ counterpart, with a normalized line ratio of ≈ 2.64 . The line ratio is also noticeably brighter on its southwestern edge than on its northeastern edge, which is not detected in He I by the decomposition procedure. The Microcavity is also observed in He I.

4.4. Absorption by the structures

One of the most difficult questions concerning the ionized features is to find out their relative positions, i.e. when two structures are overlapping, which one is closer to the observer. On two occasions, the flux maps (Appendix B) can be used to find this information.

The flux map of the Northern Arm shows a region of low intensity, which north-western boundary is a well defined line, approximately north-east/south-west. This limit between a region of low intensity and a region of high intensity is most obvious south of IRS 1 and west of the Minicavity. This line follows very closely the outline of the Eastern Arm. This gives us two pieces of information:

- the Northern Arm is behind the Eastern Bridge on the line of sight;

- the Eastern Bridge contains a substantial amount of dust, responsible of the absorption of about 50% of the Br γ flux of the Northern Arm.

The flux map of the Bar is less smooth than that of the Northern Arm, making such effects more difficult to see. However, on this map, the characteristic shape of the Minicavity is clearly identified in absorption. Again, that tells us that the Bar is behind the Northern Arm on the line of sight.

5. Keplerian orbit fitting

The velocity maps show a view of the features very different from the usual flux maps which, by themselves, can be misleading. For instance the morphology of the Northern Arm with its typical bright rim may lead one to think of this rim as the true path for most of the material. On the other hand, the velocity map shows no peculiar feature at the location of the rim. This is particularly intriguing for the location where it appears to bend abruptly, just a few arcseconds north of IRS 1 and east of IRS 7 (spot C on Fig. 12). Thus we are led to the idea that the kinematics of the Northern Arm should be studied independently of its intensity distribution.

5.1. Fitting one orbit on a velocity map

As a first attempt at using the information contained in the new tools that are the velocity maps, we tried to analyse the Northern Arm as a Keplerian system. For a first, simple approach, we created a dedicated IDL graphical package called `GuiMapOverlay` (Fig. 7). With this tool, the user can easily adjust one Keplerian orbit over a velocity map, the location and mass of the central object being those of Sgr A* (position of Sgr A* relative to IRS 7 from Menten et al. 1997, position of IRS 7 relative to the other stars of the field from Ott et al. 1999 and a distance of 8 kpc). The central mass is still a matter of debate. We have used a value of $3 \times 10^6 M_{\odot}$ (Genzel et al. 2000, Ott et al. 2003 give a value of $2.9 \times 10^6 M_{\odot}$) for most of our models. We will discuss the impact of changing this mass later. A Keplerian orbit in 3D is defined by five orbital parameters: the eccentricity, two angles defining the orientation of the orbital plane, the periape (distance of closest approach to the center of motion), and a third angle defining the position of the periape.

Once the user is almost satisfied with the orbital parameters found by trial and error, an automatic fitting procedure can be called. It is possible to fix parameters, and the orbit can be forced to go through a selected constraint point by tying the periape to the other parameters. After a few experiments with this tool, we are led to some general conclusions:

- good agreement can be found between observed and calculated velocities, except in the region of the Minicavity;
- this model alone is not sufficient to decide whether the orbits are bound or not, or whether the data are compatible with elliptical, parabolic, or hyperbolic motion.

The second of these points is not satisfactory, as one of the most interesting questions is to decide whether the gas is bound.

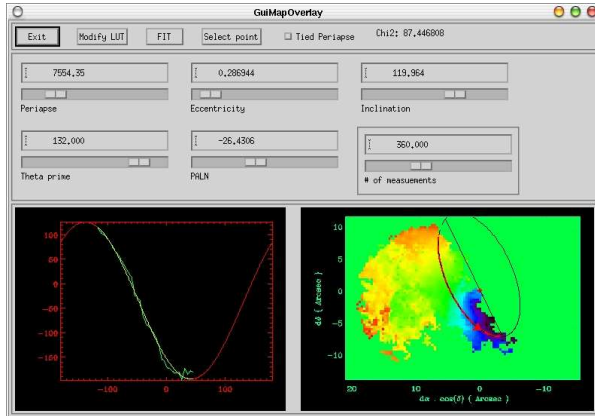


Fig. 7. GuiMapOverlay: given a set of orbital parameters, this tool draws the path of the corresponding Keplerian orbit on a velocity map, extracts the observed velocities along this path, and plots both the observed and computed velocity curves. The $\langle \chi^2 \rangle$ is also computed and shown.

Nevertheless, the first point convinced us to carry on Keplerian modeling. So, we attempted to model the Northern Arm with several orbits instead of only one.

5.2. Fitting a bundle of orbits on a velocity map

To fit several orbits at a time on a velocity map, the different orbits must be forced to be actually different. That can be done by forcing each one to pass through a different constraint point, as explained in the one orbit case. Obviously, the constraint points themselves must be chosen on different physical orbits. We have chosen to take the constraint points aligned across the gas lane, evenly spaced in projection on a line that passes through Sgr A*. We have tried two different such constraint lines (Fig. A.1), and found consistent results. The result described here uses 50 constraint points, evenly spaced on the solid line of Fig. A.1. Each constraint point is given an index, increasing from the point nearest Sgr A* outwards, that is used to refer to a given orbit.

To ensure a smooth model – we are interested only in the global motion – the four functions that map each constraint point to one of the parameters have been chosen to be described as spline functions, uniquely defined by their value at a number of control points, chosen among the constraint points. The number of points used to define the spline function can be freely chosen to set the spatial resolution of the model. After several attempts, we have chosen to fix this number to four in our final model. Thus, having four functions (one for each of the orbital parameters), each of them being defined by four values, the model depends on sixteen parameters.

We designed a fitting procedure to adjust this model based on the observed velocity map by minimizing the reduced $\langle \chi^2 \rangle$. Thus, it becomes possible to either fix some parameters, or to force them to have the same value for each orbit. This way, for example, it is possible to check whether the observed velocity map is consistent with coplanar orbits or with uniform eccen-

tricity. To avoid studying only local minima in the parameter space, it is also important to use several initial guesses.

5.3. Homothetic hypothesis

We designed a tool quite similar to GuiMapOverlay to easily study whether the data are consistent with a homothetic² set of orbits, which is the simplest model.

With the hypothesis of a homothetic set of orbits, the eccentricity still cannot be well constrained. Bound orbits seem to be preferred, but the agreement is as good with circular orbits and very eccentric orbits, close to parabolic. The residual map always has the same shape: the observed velocities are always smaller than the computed ones along the inner edge of the bundle of orbits, and higher along the outer edge. The global agreement is always poor, with $\langle \chi^2 \rangle^{1/2} \approx 70$.

5.4. General case

A few of these homothetic models have been chosen as initial guesses for other adjustments, with released constraints. It is first interesting to check the coplanar hypothesis, in which only the two parameters that define the orbital plane are kept uniform, and the uniform eccentricity hypothesis. The agreement is much better when making either the eccentricity or the orbital plane free. In the following, both parameters are free.

Even with the most general situation, the parameters are still not constrained enough to decide whether the orbits are all bound or not, to extrapolate the model outside the field of view, nor even to derive reliably the direction of proper motion. However the models share a few characteristics that we judge to be robust because of their repeatability:

1. the orbital planes are close to that of the CND;
2. the orbits are not quite coplanar; the two angles that define the orbital plane vary over a $\approx 10^\circ$ range;
3. the eccentricity varies from one orbit to another, being close to parabolic or above for the innermost orbits, and closer to circular (below ≈ 0.5) for the outermost.

5.5. 3D morphology and time-scale of the Northern Arm

We present here our best model, i.e., the one with the lowest $\langle \chi^2 \rangle^{1/2}$ among the realistic models that cover most of the Northern Arm. The laws used for this model are shown in Fig. 8. The agreement between the radial velocity map of this model and the observed velocity map is good: $\langle \chi^2 \rangle^{1/2} = 26$. The method is unbiased, and the mean error in the radial velocity from this model is 10 km s^{-1} , as estimated from Fig. 9. A 3D velocity map of the Northern Arm from this model is available online in FITS format at CDS (<http://cdsweb.u-strasbg.fr/>). It consists of one map for each 3D component of the velocity in km s^{-1} (Fig. 10), and

² Two orbits are said to be ‘homothetic’ when they are identical except for their scale, i.e. when they share the same orbital parameters, except the periaapse distance.

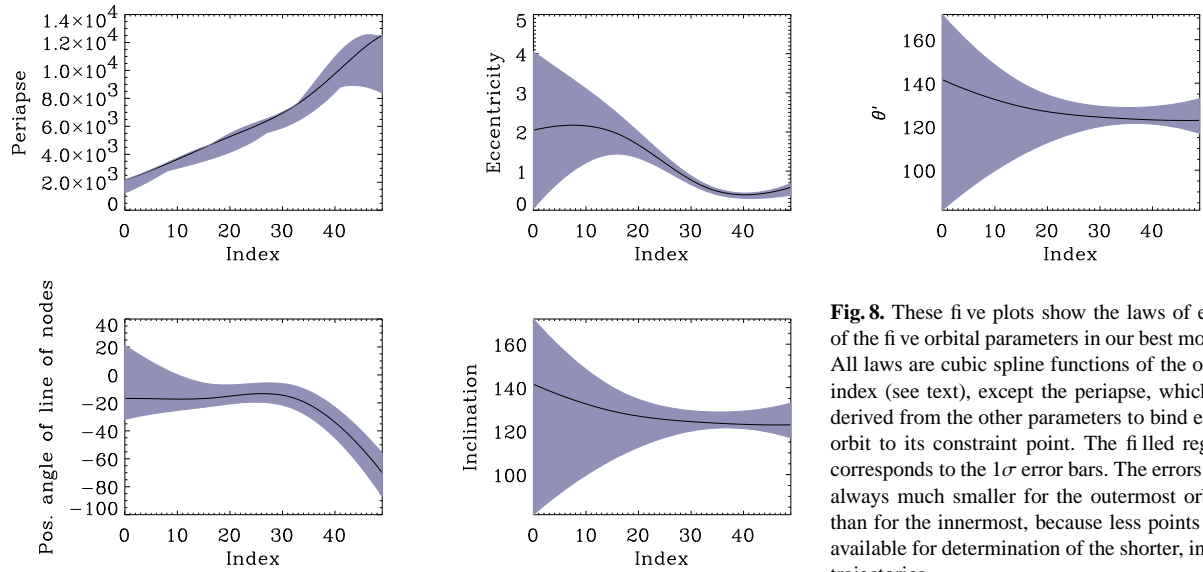


Fig. 8. These five plots show the laws of each of the five orbital parameters in our best model. All laws are cubic spline functions of the orbit index (see text), except the periapse, which is derived from the other parameters to bind each orbit to its constraint point. The filled region corresponds to the 1σ error bars. The errors are always much smaller for the outermost orbits than for the innermost, because less points are available for determination of the shorter, inner trajectories.

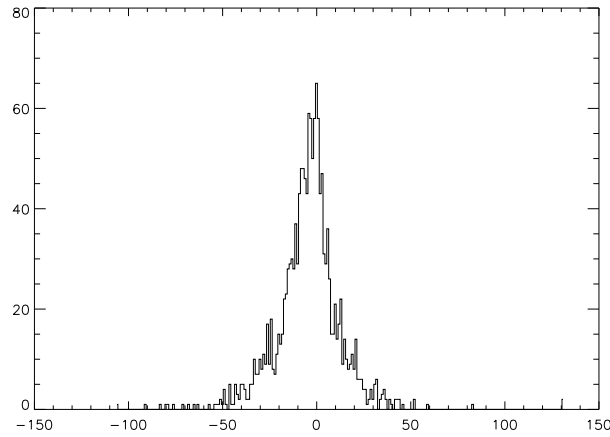


Fig. 9. Histogram of the radial velocity difference between our model and measurement; it is close to a Gaussian distribution centered on zero with $\sigma = 10 \text{ km s}^{-1}$. That means that the method is unbiased, and that the mean error is 10 km s^{-1} .

one map giving the distance to the observer for each point of the field (offset from center of mass in equivalent arcseconds, Fig. 11).

The variations of the orbital parameters induce a particular 3D shape for the Northern Arm (Fig. 12): for all the non-coplanar models, the Northern Arm looks like a warped surface, and this warping induces a crowding of orbits that closely follows the bright rim of the structure. That suggests that the Northern Arm is either a warped planar structure, or the ionized surface of a neutral cloud. The bright rim itself is not only due to the stronger UV field and a real local enhancement of the density, but also to an enhancement of the column-density due to the warping. An interesting point is that, in some models, *no* orbit follows the bright rim, which emphasizes that it is

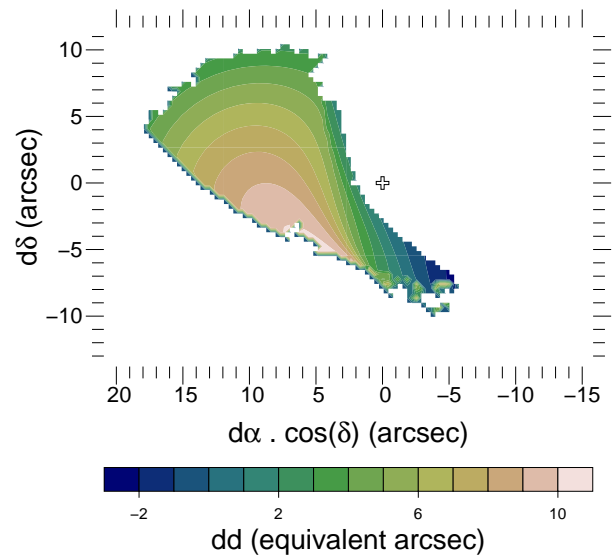


Fig. 11. Elevation map for the detected part of the Northern Arm from our model, given in equivalent arcseconds for homogeneity. dd stands for differential of the distance, positive dd means further away from the observer than the center of mass, Sgr A*, at $d\alpha = 0$, $d\delta = 0$, $dd = 0$.

really important to consider the dynamics independently from the morphology of the Northern Arm. Another characteristic present in all the models is that the period of the orbits ranges from a few 10^4 years to a few 10^5 years, which implies that the Northern Arm would have a completely different shape in a few 10^4 years, and cannot be much older than that time-scale.

Since the agreement in radial velocity is now rather good, it makes sense to look at the deviations from global motion by

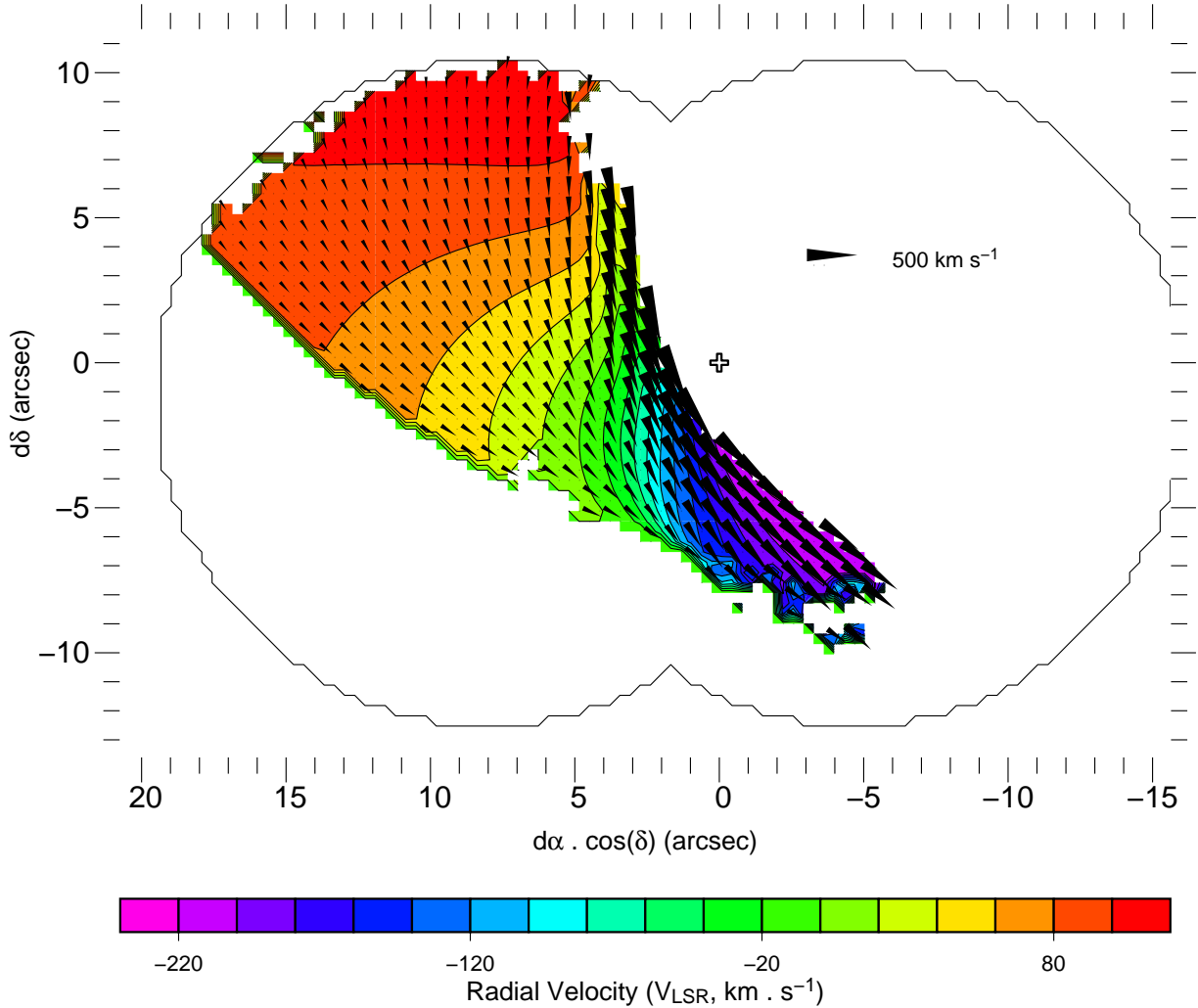


Fig. 10. 3D velocity map for the Northern Arm from our model. The arrows show the derived tangential velocities.

looking at the extended features on the residual velocity map (Fig. 12):

- A) the fbw shows a rather significant deviation in the region just southwest of the embedded star, IRS 1W; this perturbation could be due to the interaction with this star's wind;
- B) the region of this model closest to the Minicavity is perturbed;
- C) another deviation is seen at the precise location where the bright rim bends abruptly, just east of IRS 7E2;
- D) finally, an elongated feature is seen on the fainter rim coming from IRS 1W towards the northeast.

This best model uses a central mass of $3 \times 10^6 M_{\odot}$. It has been used as the initial guess for a final adjustment using $4 \times 10^6 M_{\odot}$ (Ghez et al. 2003). With this value of the central mass, every remark made above is still valid. The $\langle \chi^2 \rangle$ is not changed significantly, so that this work cannot help measuring this mass. The most noticeable difference is that the error bar for the innermost orbit is two times smaller, and is not compat-

ible with elliptical (bound) motion anymore. Thus, the exact value of this parameter is very important to confirm whether or not some of the Northern Arm material is on unbound orbits.

5.6. The Minicavity

The Minicavity is seen as low intensity level in the Northern Arm flux map. However, material of this structure is detected on the line of sight of this region. Even at that location, mostly devoided of ionized gas, the velocity map of the host structure is essentially that of a fbw. However, though it is not obvious on the velocity map of the Northern Arm, a perturbation of the motion is detected there. Our Keplerian model does not pass through the Minicavity, but just south of it. However, this model does not include the outermost regions of the Northern Arm. These regions are those with the most circular motion, that is essentially east-west within our field. So the material from these outermost regions may well pass closer to the Minicavity, or even through its projected location.

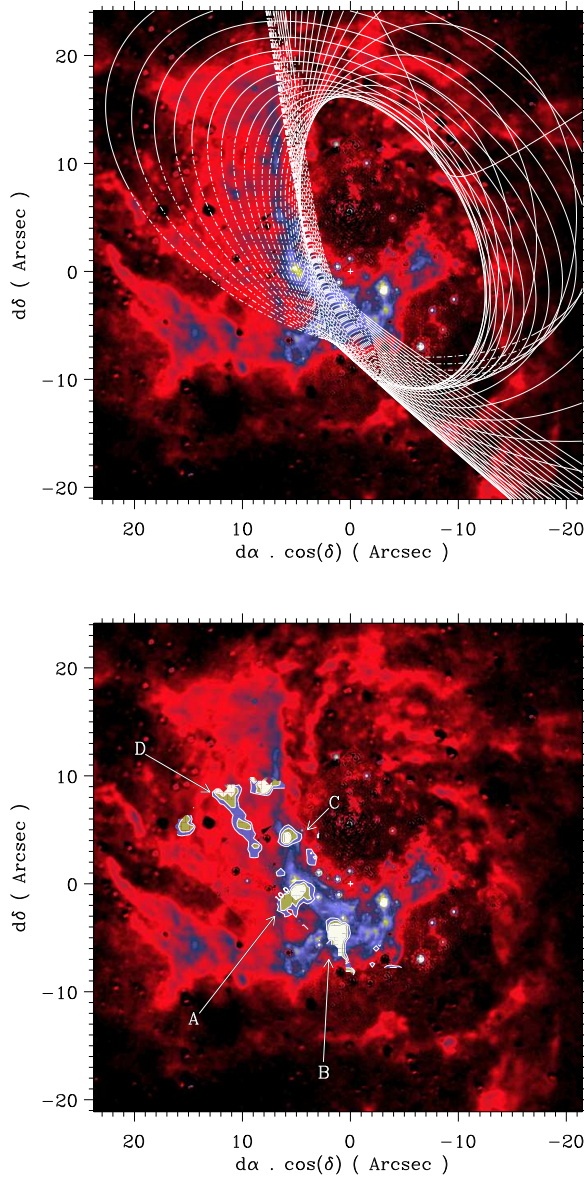


Fig. 12. On this Pa α map (Scoville et al. 2003), one of the Keplerian models is overplotted (top panel). This one is quite consistent with the Northern Arm and the Western Arc being related structures. On the bottom panel, the most significant deviations from Keplerian motion discussed in the text are labeled A to D, and indicated as filled contour.

However, even though the velocity map inside is essentially that of a fbw rather than that of an expanding bubble, the velocity field is highly perturbed, and a good fit with Keplerian motion must not be expected for this region.

The well-known shape of the Minicavity comprises a bright spot coincident with IRS 13E on the northern end of its western edge. This bright spot is not seen in the flux map of the Northern Arm, Which contains the Minicavity. It is first due to

emission from IRS 13E, clearly detected both in He I (Paumard et al. 2001), but also in Bry (Maillard et al. 2003). However, the flux map of the Bar peaks sharply on the same line of sight. This seems to show that the compact star cluster IRS 13E excites locally material in the Bar, and must be either embedded in it, or very close to it. However, coincidence between the bright spot at this location and the end of the western edge of the Minicavity seems to be a projection effect, and nothing physical.

The last fact worth noting concerning the Minicavity is the small finger-looking feature at the north of its eastern side. As already discussed Sect. 4.2, two velocity components are detected at this feature. Both connect continuously with the Northern Arm in velocity. From their velocity, it seems that this finger is deflected by the Minicavity towards the north and towards the observer.

6. Discussion

The geometry of the Northern Arm has been studied from its velocity map, leading to the conclusion that it may not be a planar structure, but rather a three-dimensional structure. Fig. 12a is quite compatible with the Northern Arm indeed being the ionized surface of a neutral cloud (as suggested by Jackson et al. 1993; Telesco et al. 1996). This figure also suggests that the Northern Arm and the Western Arc may be two parts of the same physical structure. The velocity derived from the model agrees with the measured velocity of the Western Arc with $\approx 50 \text{ km s}^{-1}$ (which is reasonable since its an extrapolation) and has the right gradient. However, this coincidence is lost when a central mass of $4 \times 10^6 M_{\odot}$ is used. However, the adjustment is not made over the entire Northern Arm, since our field of view is limited. The same study on a complete map of the Northern Arm would probably reveal whether it is bound, and whether the Northern Arm and Western Arc are one same physical feature. The tangential velocity field of the Northern Arm (Fig. 10) is interestingly similar the magnetic field derived by Aitken et al. (1998). We agree with them that this seems to imply that even if the Northern Arm is part of a cloud stretched by the tidal forces from Sgr A*, its dynamics is sufficiently Keplerian for the magnetic field lines to get aligned with the velocity.

We have shown that at least two structures are thick, dusty clouds, because their absorption factor is of the order of several 10% at $2 \mu\text{m}$: the Eastern Bridge and the edges of the Minicavity in the Northern Arm. From the wider field in Pa α , we can assume that the Eastern Bridge is an elongated cloud, of which we detect only the western front, that seems to be forward front if its motion is mostly east-west. The lack of shear inferred from its velocity map can be explained by the fact that if it is really the forward front of the cloud, then the velocity field must be perpendicular to its surface.

The presence of three isolated ionized gas structures (the Western Bridge, the Northern Arm Chunk and the Bar Overlay) in addition to the standard large fbws and to the Eastern Bridge, that seems to be another fbw, has been demonstrated. Some of these structures may be isolated gas patches, but it is also possible that some of them are regions of the neutral clouds

which ionized fronts form the Minispiral, locally excited. For instance, the Bar Overlay, which velocity map is very similar to that of the Bar, may be a region belonging to the same neutral cloud as the Bar, locally excited by IRS 14W. The $[\text{He I}]/[\text{Br}\gamma]$ line ratio is significantly higher for these tenuous features than for the standard Northern Arm, Eastern Arm and Bar. This ratio is variable across each structure. These variations must be explained. They can basically have two reasons: first, they can be the trace of local enrichment of the gas in helium, and second, they can be due to local enhancements of the excitation, either because of a stronger UV field, or because of shocks.

As has already been mentioned in Paumard et al. (2001), there are about 20 high mass loss stars in the region. A typical mass loss rate for stars of these spectral types is of the order of $\approx 10^{-4} M_{\odot} \text{ yr}^{-1}$ (Najarro et al. 1994). This material must reside in the central parsec for a duration similar to the time-scale of the Northern Arm: $\approx 10^4$ yr. From these considerations, the total mass of interstellar gas in the central parsec coming from the mass loss of these stars must be around a few tens of solar masses. In the other hand, if the ionized structures are really the ionized front of neutral clouds, these clouds could have a mass similar of that of the clouds that form the Circumnuclear Disk: $\approx 10^3 M_{\odot}$ each (Christopher & Scoville 2003). Thus, it is unlikely that interstellar gas of stellar origin contributes significantly to the enrichment of these clouds.

However, there is a clear correlation between the projected proximity of gas to the helium stars and the $[\text{He I}]/[\text{Br}\gamma]$ line ratio:

- two of the gas patches detected in both lines having a high $[\text{He I}]/[\text{Br}\gamma]$ ratio are coincident with the helium star IRS 34W;
- the Bar, which is the main feature with the highest line ratio, is close to the IRS 16 helium star cluster, and contains the IRS 13E star cluster, which is made of several high-mass-loss-rate stars (Maillard et al. 2003);
- the Tip, the feature with the highest $[\text{He I}]/[\text{Br}\gamma]$ ratio, seems to be interacting with a star wind through the Microcavity and is on the same line of sight as the helium star IRS 9W;
- the differences in the shape of the Northern Arm between the two spectral lines seem to clearly come from the geometry of the UV field around the IRS 16 cluster.

The discrepancies that are most difficult to explain are the high brightness in He I, in contrast to their relative faintness in Br γ at the south-western parts of both the Microcavity and the Tip. However, this part of the Microcavity is rather close in projection to the AF star, which flux, if this proximity is not only in projection, could favor He I emission. Finally, our results remain consistent with a well mixed interstellar material, distributed in a non-uniform UV field, which exact value at a given point depends on the 3D localization of nearby hot stars.

In addition to that, a Microcavity has been discovered at the elbow between the Eastern Arm Ribbon and Tip. It is probably a new example of interaction between stellar wind or polar jet and an ISM cloud, similar to the Microcavity. The deviation from Keplerian motion detected in the Northern Arm's velocity map close to IRS 1W is also interesting, as it is probably

due to the interaction of the flow and the wind of this WR star (Tanner et al. 2003). These interactions show that the dynamics of the flows must be influenced by the stars, as Yusef-Zadeh & Wardle (1993) suggested for the wind of the IRS 16 cluster, and the associated energy dissipation must be taken into account to finally figure out the accretion rate.

7. Conclusion

The different points discussed above show that the stellar and interstellar contents of the Galactic Center must be studied together to better understand them. The 2D maps of the $[\text{He I}]/[\text{Br}\gamma]$ line ratio are in themselves interesting, but we cannot fully understand them without the complete knowledge of the 3D distribution of the interstellar material, as the line strengths are related not only to the relative abundances of the different elements, but also to the ionizing UV field, which in turn depends on the distance to the ionizing sources, mainly the IRS 16 cluster, and on complex shadowing effects from the multiple ISM components.

The knowledge of the radial velocity field of the Northern Arm has allowed us to propose a kinematic model, which provides a three dimensional map of this feature. Having such maps for all of the ISM features would give us the opportunity to directly understand the shadowing effects, and to estimate the UV field that hits these ISM features. In addition to this 3D map of the Northern Arm, we begin to gain access to the relative positions of features along the line of sight: the Eastern Bridge is closer to the observer than the Northern Arm, and the Bar is behind the Microcavity. It would then become possible to estimate the helium abundance in the different structures from their relative line ratios. This in turn would give a clue to the origin of these structures.

This work has been performed on a field covering most of the inner parts of the Minispiral. However, repeating the same analysis on a wider field, containing the Minispiral to its full extent, would allow to directly check whether the Northern Arm and the Western Arc are related features. Moreover, obtaining the velocity maps of a wider field would allow one to better constrain the parameters of the Keplerian fit to the Northern Arm, and may then reveal deviations to the Keplerian model, due to momentum loss. This would be a very interesting clue to the accretion process. This scientific program requires a wide-field spectro-imager with spectral and spatial resolutions comparable with those of BEAR.

Acknowledgements. We are grateful to Miville-Deschênes³ from the *Institut d'Astrophysique Spatiale* (Orsay – France) for giving us the original version of the IDL spectral decomposition package and helping us in the early stages of customizing and expanding it.

References

Aitken, D. K., Smith, C. H., Moore, T. J. T., & Roche, P. F. 1998, *MNRAS*, 299, 743

³ Currently at the Canadian Institute for Theoretical Astrophysics (Toronto – Canada).

- Christopher, M. H. & Scoville, N. Z. 2003, in *Active Galactic Nuclei: from Central Engine to Host Galaxy*, meeting held in Meudon, France, July 23-27, 2002, Eds.: S. Collin, F. Combes and I. Shlosman. ASP (Astronomical Society of the Pacific), Conference Series, Vol. 290, p. 389., 389
- Figer, D. F., McLean, I. S., Becklin, E. E., et al. 2000, in *Proc. SPIE Vol. 4005*, p. 104-112, *Discoveries and Research Prospects from 8- to 10-Meter-Class Telescopes*, Jacqueline Bergeron; Ed., 104-112
- Geballe, T. R., Krisciunas, K., Bailey, J. A., & Wade, R. 1991, *ApJ*, 370, L73
- Genzel, R., Pichon, C., Eckart, A., Gerhard, O. E., & Ott, T. 2000, *MNRAS*, 317, 348
- Ghez, A., Salim, S., Hornstein, S., et al. 2003, *ApJ*, soumis, astro-ph/0306130
- Jackson, J. M., Geis, N., Genzel, R., et al. 1993, *ApJ*, 402, 173
- Lacy, J. H., Achtermann, J. M., & Serabyn, E. 1991, *ApJ*, 380, L71
- Lo, K. Y. & Claussen, M. J. 1983, *Nature*, 306, 647
- Maillard, J. P. 1995, in *ASP Conf. Ser. 71: IAU Colloq. 149: Tridimensional Optical Spectroscopic Methods in Astrophysics*, 316
- Maillard, J. P. 2000, in *ASP Conf. Ser. 195: Imaging the Universe in Three Dimensions*, 185
- Maillard, J. P., Paumard, T., Stolovy, S. R., & Rigaut, F. 2003, *A&A*, submitted
- Menten, K. M., Reid, M. J., Eckart, A., & Genzel, R. 1997, *ApJ*, 475, L111
- Morris, M. & Maillard, J. P. 2000, in *ASP Conf. Ser. 195: Imaging the Universe in Three Dimensions*, 196
- Najarro, F., Hillier, D. J., Kudritzki, R. P., et al. 1994, *A&A*, 285, 573
- Ott, T., Eckart, A., & Genzel, R. 1999, *ApJ*, 523, 248
- Ott, T., Schödel, R., Genzel, R., et al. 2003, *The Messenger*, 111, 1
- Paumard, T., Maillard, J. P., Morris, M., & Rigaut, F. 2001, *A&A*, 366, 466
- Paumard, T., Maillard, J. P., & Stolovy, S. R. 2003, in *The Central 300 parsecs*, Galactic Center Workshop, held in Kona, Nov. 4-8, 2002
- Roberts, D. A. & Goss, W. M. 1993, *ApJS*, 86, 133
- Scoville, N. Z., Stolovy, S. R., Rieke, M., Christopher, M., & Yusef-Zadeh, F. 2003, *ApJ*, submitted (astro-ph/0305350)
- Tanner, A., Ghez, A., Morris, M., & Becklin, E. 2003, in *The Central 300 parsecs*, Galactic Center Workshop, held in Kona, Nov. 4-8, 2002
- Telesco, C. M., Davidson, J. A., & Werner, M. W. 1996, *ApJ*, 456, 541
- Vollmer, B. & Duschl, W. J. 2000, *New Astronomy*, 4, 581
- Wright, G. S., McLean, I. S., & Bland, J. 1989, in *Infrared Spectroscopy in Astronomy*, 425-428
- Yusef-Zadeh, F., Roberts, D. A., & Biretta, J. 1998, *ApJ*, 499, L159
- Yusef-Zadeh, F. & Wardle, M. 1993, *ApJ*, 405, 584
- Zhao, J. & Goss, W. M. 1998, *ApJ*, 499, L163

Appendix A: Velocity maps

We present the radial velocity maps for each identified velocity structure. Axes show offsets from Sgr A* (represented as a cross), in arcseconds. To improve contrast, the color scale is not the same for each map. The binocular-shaped black line shows approximately the field boundaries.

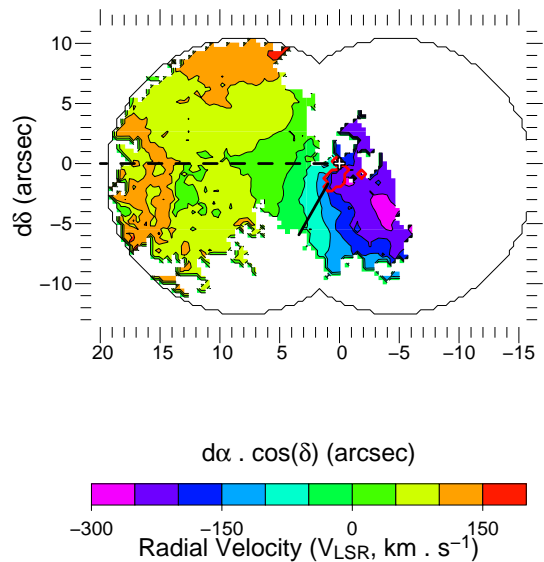


Fig. A.1. (a) Northern Arm Velocity map. The black solid line represents the constraint line (see Sect. 5.2) used for our best model. The dashed one represents another constraint line, that gave consistent results. The red contour outlines the region where two lines are detected. For these points, the bluer velocity, corresponding to the “secondary layer” (see text), is used. The velocity of the “main layer” for these points goes from ≈ -90 (north-east) to -180 km s^{-1} (south-west).

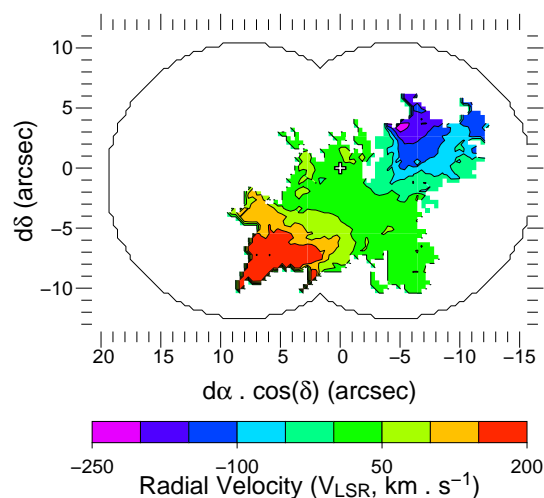


Fig. A.2. (b) Bar Velocity map

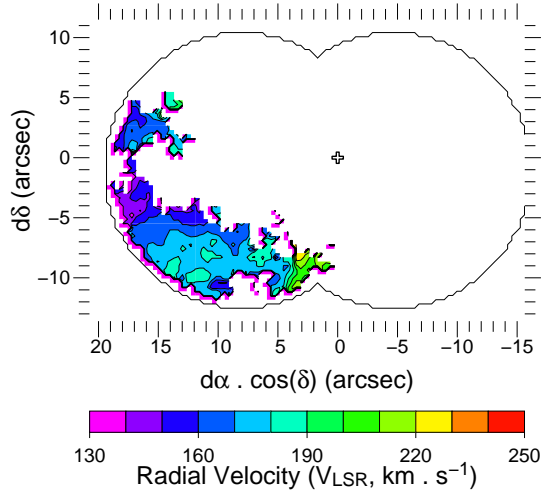


Fig. A.3. (c) Ribbon Velocity map

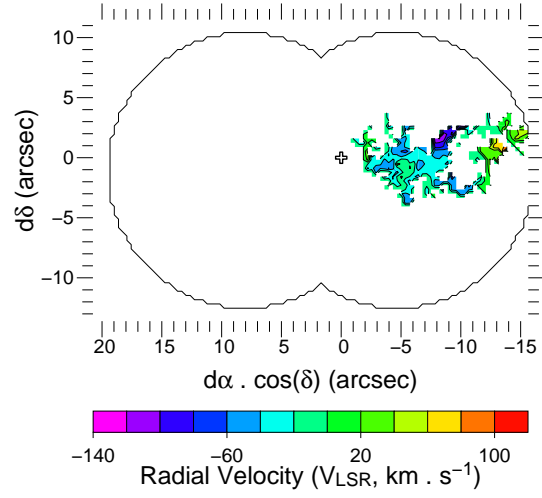


Fig. A.6. (f) Western Bridge Velocity map

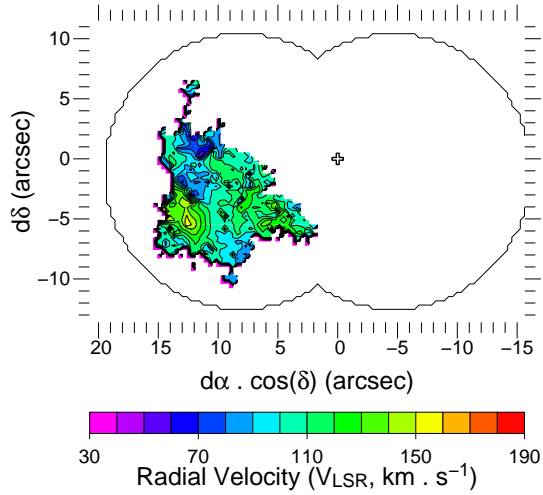


Fig. A.4. (d) Eastern Bridge Velocity map

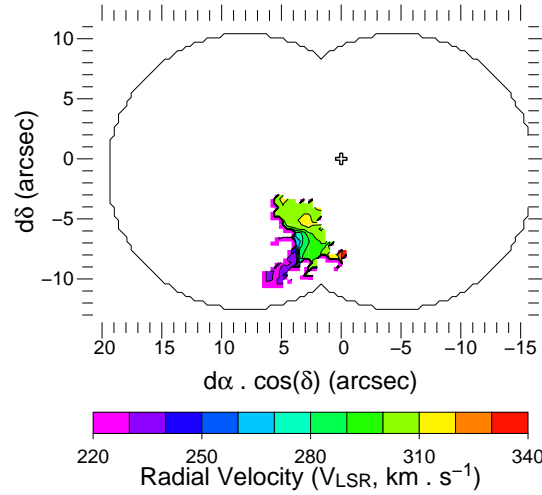


Fig. A.7. (g) Tip Velocity map

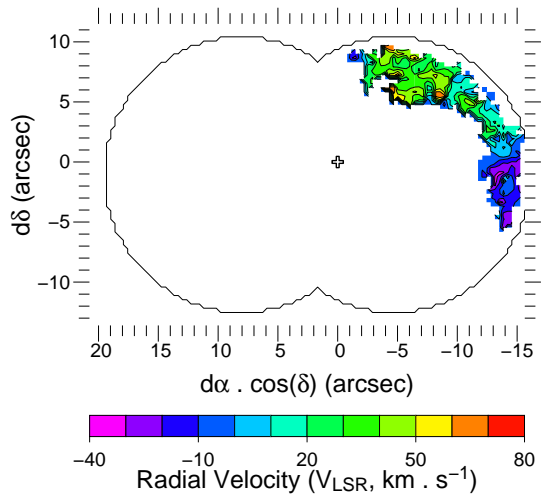


Fig. A.5. (e) Western Arc Velocity map

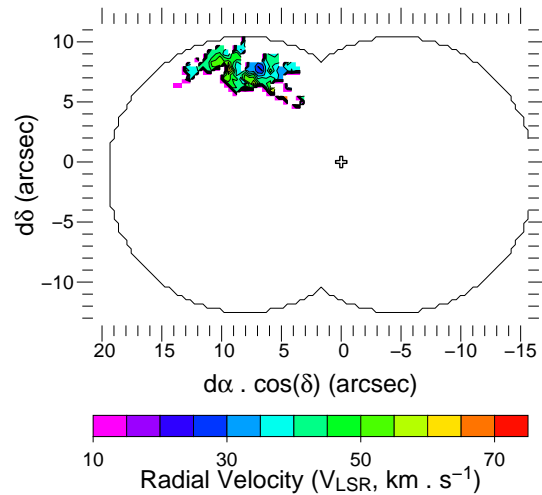


Fig. A.8. (h) Northern Arm Chunk Velocity map

16

T. Paumard et al.: Kinematic and structural analysis of the Minispiral

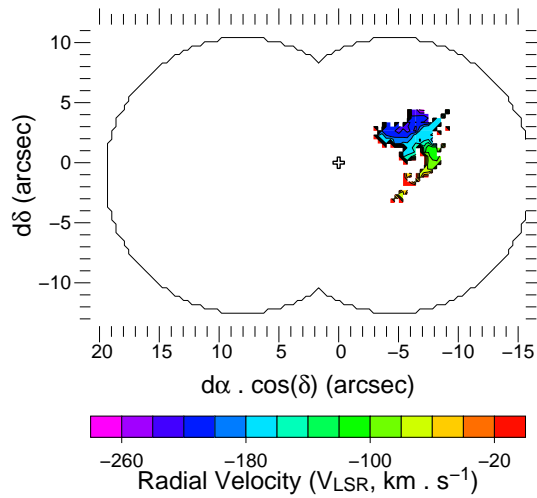


Fig. A.9. (i) Bar Overlay Velocity map

Appendix B: Flux maps

Flux map (peak intensity \times width of the line) for each structure. Black outlines give the full extent of the detected structure, and field boundaries. Axes are offsets from Sgr A*, which position is marked by a cross.

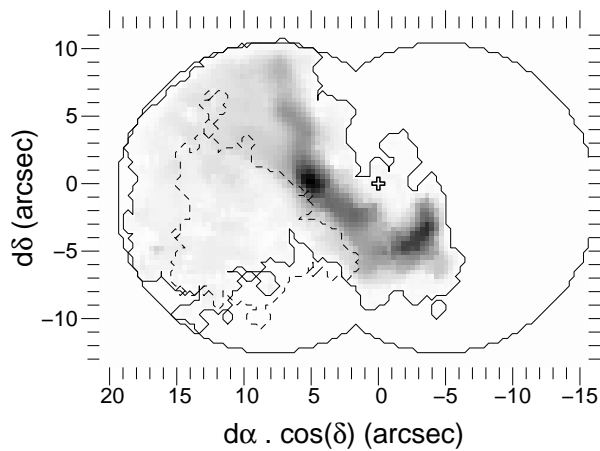


Fig. B.1. (a) Northern Arm flux map. The outline of the Eastern Bridge is given (dashed line), showing that this structure is superimposed on a weak region of the Northern Arm (Sect. 4.4).

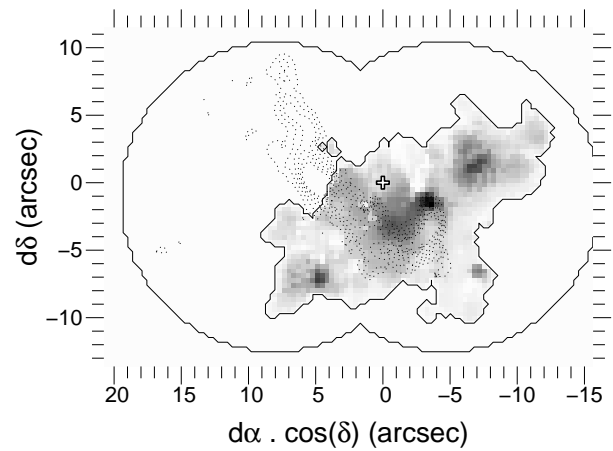


Fig. B.2. (b) Bar flux map. A few contours of the flux map of the Northern Arm are given (dotted lines), showing that the Minicavity corresponds to a low level region of the Bar (Sect. 4.4).

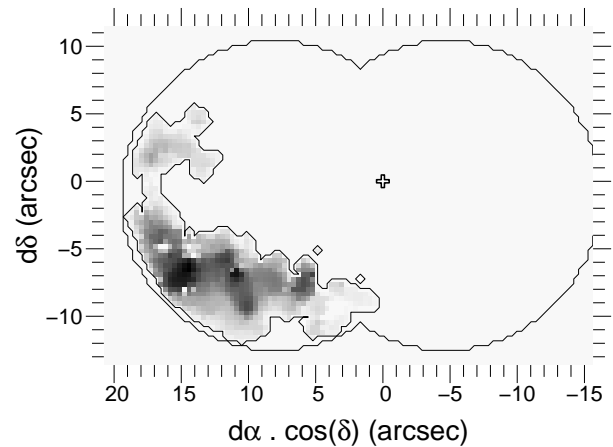


Fig. B.3. (c) Ribbon flux map

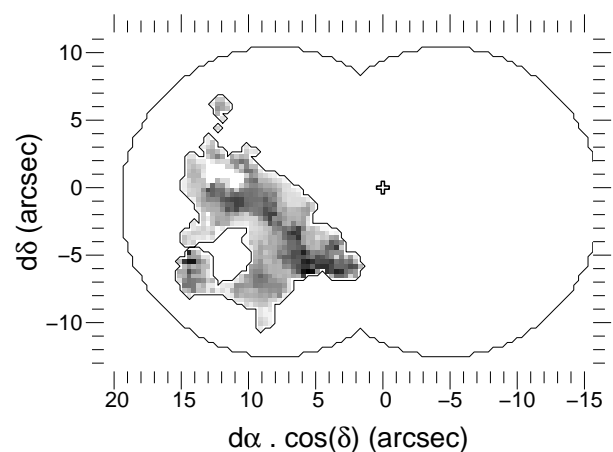


Fig. B.4. (d) Eastern Bridge flux map

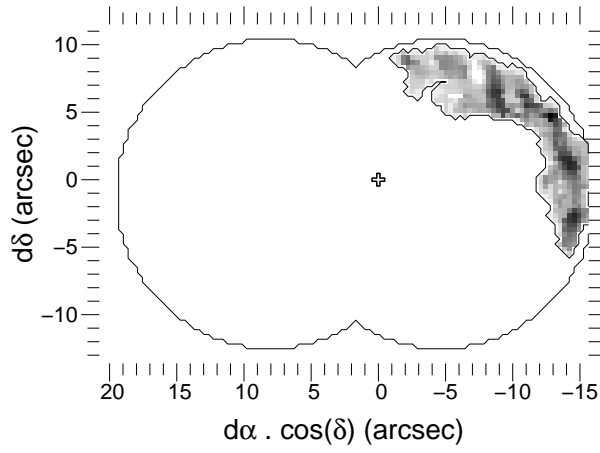


Fig. B.5. (e) Western Arc flux map

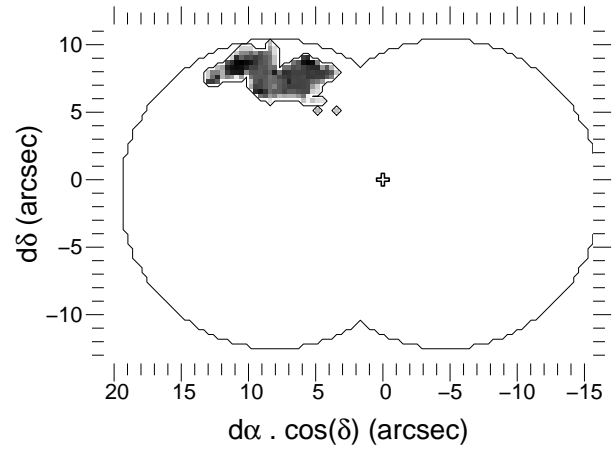


Fig. B.8. (h) Northern Arm Chunk flux map

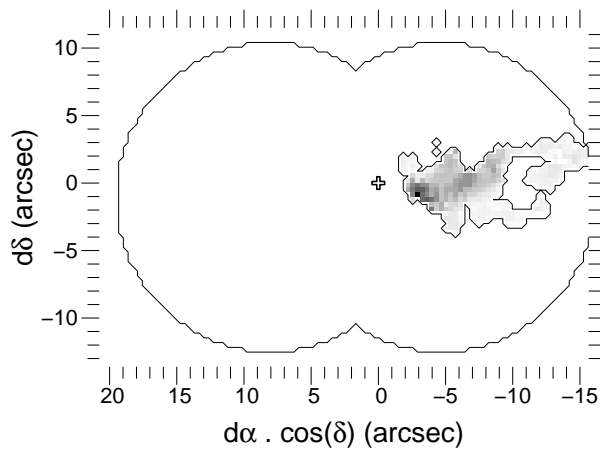


Fig. B.6. (f) Western Bridge flux map

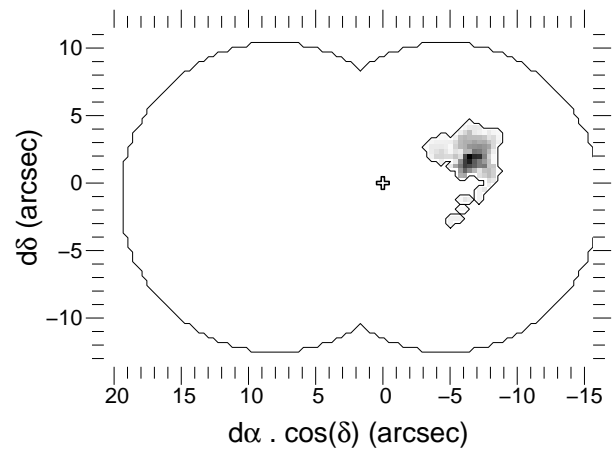


Fig. B.9. (i) Bar Overlay flux map

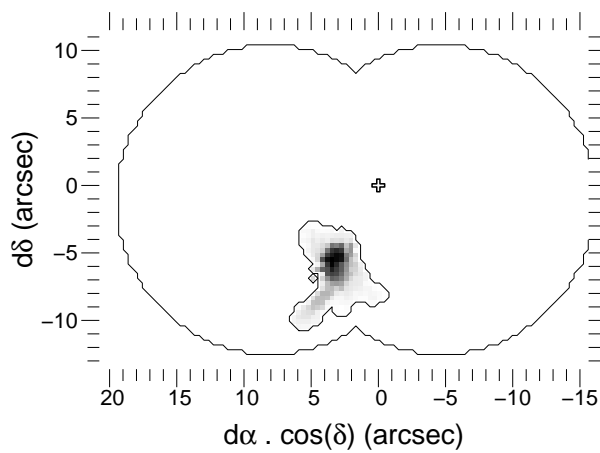


Fig. B.7. (g) Tip flux map

Annexe F

Article « *Structural analysis of the Minispiral from high-resolution Br γ data* »

Contribution pour la conférence *Galactic Center workshop 2002*, relative au travail sur la Minispirale.

Structural analysis of the Minispiral from high-resolution Br γ data

Thibaut Paumard¹, Jean-Pierre Maillard¹, and Mark Morris²

¹ Institut d'astrophysique de Paris (CNRS), 98b Bd. Arago, 75014 Paris, France

² University of California, Los Angeles, Div. of Astronomy, Dept. of Physics and Astronomy, Los Angeles, CA 90095-1562, USA

Received 15 November 2002, revised 30 November 2002, accepted 2 December 2002

Published online 3 December 2002

Key words dynamics, ionized gas, Sgr A West, Galaxy: Center, infrared, spectro-imaging, FTS

PACS 04A25

Integral field spectroscopy of a roughly $40' \times 40'$ region about the Galactic Center was obtained at $2.16 \mu\text{m}$ (Br γ) using BEAR, an imaging Fourier Transform Spectrometer, at a spectral resolution of 21.3 km s^{-1} , and a spatial resolution of $\simeq 0.5''$. The analysis of the data was focused on the kinematics of the gas flows concentrated in the neighborhood of SgrA*, traditionally called the 'Minispiral'. From the decomposition into several velocity components (up to four) of the line profile extracted at each point of the field, velocity features were identified. Nine distinguishable structures are described: the standard Northern Arm, Eastern Arm, Bar, Western Arc, as well as five additional moving patches of gas. From this analysis, the Northern Arm appears not limited, as usually thought, to the bright north-south lane seen on intensity images, but consists instead of a continuous, weakly-emitting, triangular-shaped surface having a bright western rim, and narrowed at its forward apex in the vicinity of SgrA* where a strong velocity gradient is observed. The gravitational field of the central Black Hole can account for both the strong acceleration in this region and the tidal compression of the forward tip of the Northern Arm. Keplerian orbits can be fitted to the velocity field of the bright lane, which can be interpreted as formed by the bending of the western edge of the flowing surface. These results raise questions regarding the formation of the Sgr A West gas structures.

1 Introduction

Within the inner 2 pc of the Galactic Center (GC) lies the Sgr A West region, dominated by ionized gas which has been detected in the infrared and at radio wavelengths because of high obscuration along the line of sight. The gas distribution has been observed in infrared and radio emission lines, as well as in radio continuum (Lacy *et al.* 1991, Lo & Claussen 1983, Roberts & Goss 1993, Zhao & Goss 1988), and proper motion of the bright blobs have been derived (Zhao & Goss 1988). All these data show that the ionized gas in the inner few parsecs of Galactic Center is organized into a spiral-like feature (Fig. 1) with a number of 'arms', which led to the name 'Minispiral' for the entire pattern. The various features give a spiral appearance primarily because of the way they are superposed on each other. However, a new analysis of Lacy's data was conducted by Vollmer & Duschl (2000) to re-examine the kinematic structure of the ionized gas. Using a three-dimensional representation, they confirm the standard features, but with a more complex structure, including two features for the Eastern Arm, a vertical finger of high density, a large ribbon extending to the east of SgrA*, and two distinctly different components in the Bar. Data in different lines, acquired with better spectral and spatial resolution, warrant an independent kinematic analysis.

In the present paper, the gas content in the inner region of the GC is presented and analyzed from high spectral resolution (21.3 km s^{-1}) data cubes on the Br γ line, obtained with BEAR, an imaging FTS

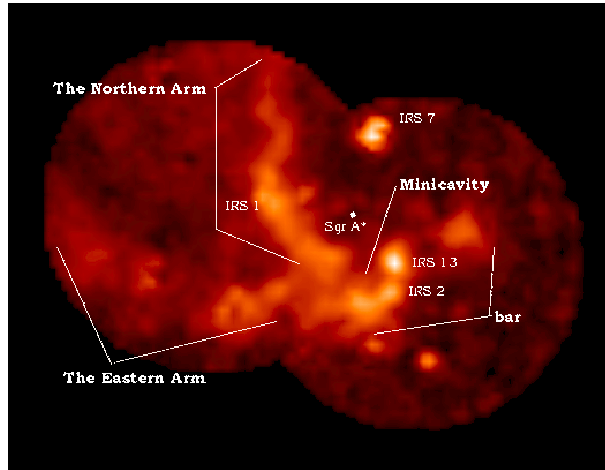


Fig. 1 Br γ intensity integrated between -400 and $+400$ km s^{-1} toward the two mosaicked fields of Sgr A West observed with BEAR. The standard bright features, Northern and Eastern Arms, Bar, and the mini-cavity, are indicated. Also, a few emission line stars show up as bright points in the image. (Morris & Maillard 2000)

(Maillard 1995, 2000) at the $f/35$ infrared focus of the 3.6-m CFH Telescope; the same work on He I data is ongoing. A preliminary analysis of these data have been presented in Morris & Maillard (2000). In Paumard *et al.* (2001, hereafter Paper I), where the helium stars were studied, the He I ISM emission was identified and described for the first time. The Br γ data cover a field of view of $40 \times 28''$ at a seeing-limited resolution of $\simeq 0.6''$. The HST-NICMOS Pa α data (Scoville *et al.* 2003), used in Paumard *et al.* (2003), are used here for high-resolution morphological considerations.

A multi-component line fitting procedure applied to the emission-line profiles in each point of the field is described in Sect. 2. From this decomposition, the identification of defined gas structures constituting the whole Sgr A West ionized region is presented in Sect. 3. Attempts to adjust Keplerian orbits to the flowing gas are presented. This is followed in Sect. 4 by a discussion of the implication of these identifications on the formation and the lifetime of the inner ionized gas.

2 Structure identification

In each point of the field (Fig. 1) the Br γ emission profile appears complex, clearly showing that along each line of sight, several ISM clouds or flows are present. So the study of these ISM features required the development of a multi-component line fitting procedure able to work on 3D data. From a coarse examination of the datacube the fitting by a maximum of four components seemed adequate. Miville-Deschêne (private communication) provided us with such software, that we adapted and developed. By comparison of the velocity components from one line of sight to the next, and by assuming continuity, it is possible to perform a reconstruction of the large-scale velocity structures. In the end, it might be possible to conclude whether these structures are independent, or continuous spiraling flows. Thus, the process is split into two main parts: first, the line profile decomposition of all the points of the field, and then the structure identification. The natural line shape of a single velocity component of the emission line from the ISM has been assumed to be Gaussian, defined by three parameters (central velocity, amplitude, and line width). The fitting procedure then adjusts four independent Gaussian lines, convolved with the instrumental PSF – which is a sine cardinal – to each spectrum. Hence the fitting function depends upon twelve independent parameters for each point of the field. The consecutive steps are the following:

Preparation: These twelve parameters are first manually determined for a few starting points, evenly distributed over the field, chosen to be representative of the most obvious features, and located on spots where four components are clearly present.

Step 1: From the starting points, a first procedure attempts to fit a four-component line shape function to each spectrum. For each new spectrum, the initial guess is determined from the results found for the neighboring points. The spectra are studied sequentially in parallel spiral-mode scanings around each starting point. Except for the initial guess, the fitting of a spectrum is independent of all the others.

Step 2: For the brightest point of the field, the neighbors are examined, and searched for a component such that the velocity gradient between the point of interest and this neighbor is less than a certain amount, which is set by the user at runtime. The procedure is iterative, and once a few neighbors have been selected into a structure, their neighbors are in turn examined for possible selection. The procedure stops when every component of every point of the field has been assigned to exactly one spatial structure. This procedure allows only one component of a given point to be selected into a given structure. Structures so warped that they overlap themselves spatially, thus causing two velocity components on the same line of sight, cannot be directly detected as such: they artificially split into several structures.

Step 3: This procedure requires that the detected structures be manually inspected. The user has then the possibility to add some more common sense heuristics in the structure identification, a little difficult to implement but easy to apply manually. Several problems can occur:

- during step 1, the fitting procedure might fit only one component where two blended components are indeed more appropriate,
- during step 2, the procedure can falsely cross-connect two structures, i.e. reconstruct two structures, each one being made of one part of one physical structure, and one part of the other one.

Step 4: Then, these manually corrected results are used to perform a second fit on each point of the field; at this point, 2D information is entirely included in the initial guess provided to the fitting procedure.

Iteration: Steps 2, 3 and 4 must be iterated a number of times, until a stable set of plausible structures is reached. ‘Plausible structures’ means only that the structures are more extended than the spatial resolution, and brighter than the detection limit of the instrument.

3 Results

3.1 General description of the results

The analysis described above leads to a vision of the Minispiral more complex than usually thought, one which is consistent with, but more detailed than the vision proposed by Vollmer & Duschl (2000). After a careful examination we identify 9 components of various sizes (Fig. 2). Two types of velocity map appear, some with an overall velocity gradient, others without any large-scale velocity gradient. The deviation from mean motion, defined as the local difference between the velocity measured at one point and the mean value for the neighboring points, and divided by the uncertainty, ranges from roughly one tenth to ten for all the features, which means that every velocity structure shows significant (over 3σ) local features.

The areal size of the structures (Table 1), expressed in terms of solid angle covered on the sky, ranges from 17 arcsec^2 to 300 arcsec^2 for the part of the Northern Arm that is visible in the BEAR field of view. The surface area of each structure must be considered as a lower limit because BEAR may not detect the weakest parts nor parts where blending with a brighter structure in the spectral domain is possible, and because the field of view does not cover the entire Minispiral.

3.2 Morphology of the ionized gas in Sgr A West

A brief description follows for each identified velocity structure, whose velocity maps are given in Fig. 2. Table 1 gives the surface coverage on the sky (within the BEAR field of view), and the maximum and minimum velocity within the given structure.

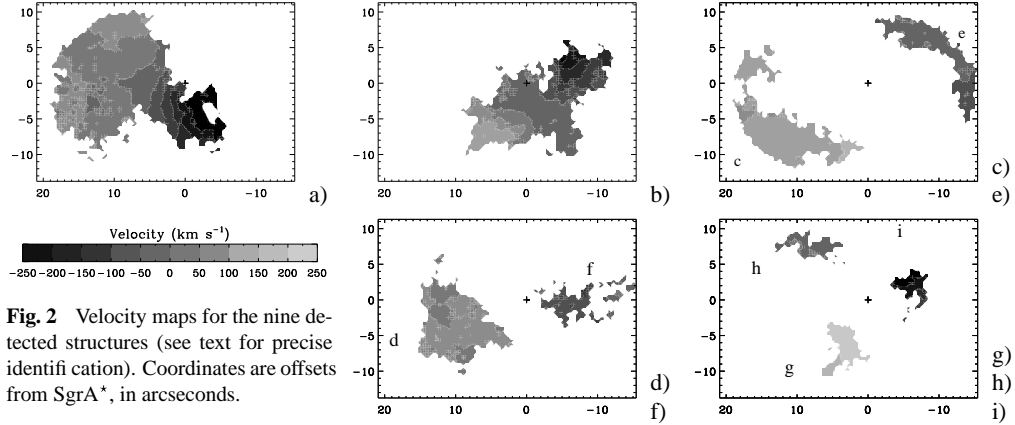


Fig. 2 Velocity maps for the nine detected structures (see text for precise identification). Coordinates are offsets from SgrA*, in arcseconds.

ID	Feature name	S (pix)	S (arcsec ²)	Vmin	Vmax
a	Northern Arm	2414	300.8	-286.9	188.9
b	Bar	1389	173.1	-211	196.9
c	Eastern Arm	833	103.8	132.9	242.9
d	Eastern Bridge	670	83.5	34.9	182.9
e	Western Arc	471	58.7	-37.1	74.9
f	Western Bridge	327	40.7	-121.1	100.9
g	Tip	207	25.8	222.9	339.0
h	Northern Arm Chunk	185	23.1	14.9	74.9
i	Bar Overlay	136	16.9	-267.0	-7.1

Table 1 Feature identifications, with surface areas (pixels and square arcseconds), and minimum and maximum radial velocities (km s⁻¹).

- a) *Northern Arm*: Contrary to its standard description, the Northern Arm is not seen here as a bright N-S lane, but as an extended, triangular surface. One edge of this triangle is the bright rim generally noticed, but it extends over to the Eastern Arm. The third edge of the triangle is the edge of the field, so viewing this feature on a larger field may yield a slightly different description. Its kinematics will be thoroughly described in the next section.
- b) *Bar*: The Bar is the most complex region, where at least three components are superimposed. The most important feature is very extended, from the Eastern Arm (c) to the Western Arc (e), very straight and shows a smooth overall velocity gradient. Vollmer & Duschl (2000) mention two complementary components of the Bar, which they call Bar 1 and Bar 2, though their description is not sufficient to determine precisely the positions of these two components. We see two additional features, which we propose to call *Western Bridge* (f) and *Bar Overlay* (i). Parts of the Bar are also superimposed on almost every other structure, including the Eastern Arm (c), the Tip (g), the Eastern Bridge (d) and the Northern Arm (a).
- c) *Eastern Arm*: The region is split into two parts: the Arm itself and a *Tip* (g). The velocity gradient of the Arm is directed along the minor axis of the structure, not along its major axis as expected for a bar.
- d) *Eastern Bridge*: A structure of medium size extends from the Eastern Arm to the bright rim of the Northern Arm. It does not show any large-scale velocity gradient, and its shape does not show any principal axis that would indicate a bar. It is superimposed on the faint regions of the Northern Arm, and partly superimposed on the Eastern Arm, the Bar and the Tip. The Pa α map (Fig.5) shows that this feature may extend outside our field-of-view into an elongated feature parallel to the Eastern Arm.

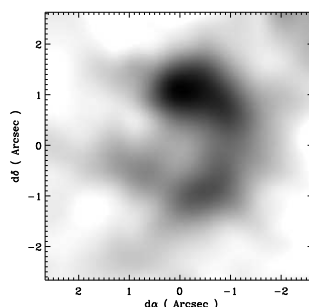


Fig. 3 Microcavity feature in the region of IRS 9W, which would be approximately located in the upper right corner. The center of this field is located $5.4''$ east and $8.1''$ south of SgrA*.

- e) *Western Arc*: The Western Arc lays just at the edge of the field, so we have access only to its innermost part. It is seen as a rather simple feature, with large scale velocity gradient.
- f) *Western Bridge*: The Western Bridge is a tenuous, elongated feature oriented east-west and extending from the Bar to the Western Arc.
- g) *Tip*: The Tip is, in projection, a very concentrated and relatively small object with the most redward velocity in the region ($\simeq 300 \text{ km s}^{-1}$). The Tip has already been noticed by Vollmer & Duschl (2000) only on a morphological basis, as a finger-like feature of the Eastern Arm in their three dimensional data. Here, we see that the Eastern Arm and the Tip are two distinct features, superimposed on the line of sight, thus we do not adopt the representation-dependent denomination ‘Finger’. At the elbow between the Eastern Arm and the Tip, in the IRS 9W region, is a bubble-like feature, or a *Microcavity* (radius $\simeq 1''$), with a rather bright rim (Fig. 3), which appears at a specific velocity (250 km s^{-1}).
- h) *Northern Arm Chunk*: A small tenuous structure is seen superimposed on the Northern Arm, a few arcseconds north of IRS 7. It lays at the edge of our field, so it could extend further out; however the Pa α image shows a small, horizontal bar at his location, crossing the bright rim of the Northern Arm, and that does not seem to be much extended.
- i) *Bar Overlay*: The Bar Overlay looks like a small cloud that is superimposed upon the western region of the Bar and that shows a velocity gradient similar to the one of the main Bar at the same location, with an offset of $\simeq -40 \text{ km s}^{-1}$. It may indicate that these two features are closely related. They could, for example, be the two faces of a single cloud.

3.3 Keplerian orbit fitting

The velocity maps show a view of the features very different from the usual flux maps which, by themselves, can be misleading. For instance the morphology of the Northern Arm with its typical bright rim may lead one to think of it as the true path for most of the material. On the other hand, the velocity map shows no peculiar feature at the location of the rim. This is particularly intriguing for the location where it bends abruptly, just a few arcsecond north of IRS 1 and east of IRS 7 (Fig. 1). Thus we are led to the idea that the kinematics of the Northern Arm should be studied independently of its intensity distribution.

As a first attempt at exploiting the information contained in the new tools that are the velocity maps, we tried to analyse the Northern Arm as a Keplerian system. For a first, simple approach, we created a dedicated IDL graphical package called `GuiMapOverlay` (Fig. 4). With this tool, the user can easily adjust one Keplerian orbit over a velocity map. A Keplerian orbit in 3D is defined by five orbital parameters: the eccentricity, two angles defining the orientation of the orbital plane, the periape (distance of closest approach to the center of motion), and a third angle defining the position of the periape.

Once the user is almost satisfied with the orbital parameters he has found by trial and error, an automatic fitting procedure can be called. It is possible to fix parameters (at least two must remain free), and the orbit can be forced to go through a selected constraint point by tying the periape to the other parameters. After a few experiments with this tool, we are led to some general conclusions:

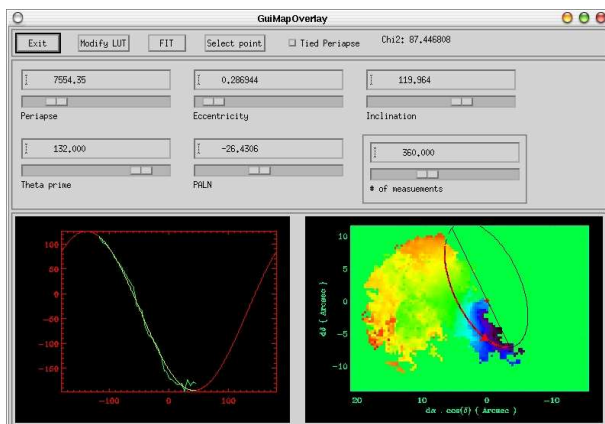


Fig. 4 GuiMapOverlay: given a set of orbital parameters, this tool draws the path of the corresponding Keplerian orbit on a velocity map, extracts the observed velocities along this path, and plots both the observed and computed velocity curves. The $\langle \chi^2 \rangle$ is also computed and shown.

- a good agreement can be found between observed and calculated velocities, except in the region of the Minicavity;
- this model alone is not sufficient to decide whether the orbits are bound or not, or whether the data are compatible with elliptic, parabolic, or hyperbolic motion.

The second point mentioned above is not satisfactory, as one of the most interesting questions is to decide whether the gas is bound. Nevertheless, the first remark encouraged us to persevere in the direction of Keplerian modeling, so we attempted to model the Northern Arm with several orbits instead of only one. Each orbit is bound to pass through a different point, by tying its periapse to the other four parameters, and all these constraint points are aligned across the gas lane, close to the line of zero radial velocity, thus ensuring that they are indeed on separate trajectories. To ensure a smooth model – we are interested only in the global motion – the four functions that map each constraint point to one of the parameters, have been chosen to be described as spline functions, defined by their value at four points. Thus, having four functions (one for each of the orbital parameters), each of them being defined by four values, the model is dependent on sixteen parameters.

We designed a fitting procedure to adjust this model based on the observed velocity map by minimizing the reduced $\langle \chi^2 \rangle$. In order to study a certain hypothesis, it is possible to either fix some parameters, or to force them to have the same value for each orbit. This way, for example, it is possible to really check whether the observed velocity map is consistent with coplanar orbits or with uniform eccentricity. To avoid studying only local minima in the parameter space, it is also important to use several different initial guesses. A tool quite similar to GuiMapOverlay has been designed to easily study whether the data are consistent with an homothetic¹ set of orbits, which is the simpler model.

3.3.1 Results

With the homothetic set of orbits hypothesis, the eccentricity still cannot be well constrained. Bound orbits seem to be preferred, but the agreement is as good with circular orbits and very elliptic orbits, close to parabolic. The residuals map has always the same shape: the observed velocities are always smaller than the computed ones along the inner edge of the bundle of orbits, and higher along the outer edge. The agreement is always poor, with $\langle \chi^2 \rangle^{1/2} \simeq 70$. A few of these homothetic models have been chosen as initial guesses for other adjustments, with released constraints. It is first interesting to check the coplanar hypothesis, by keeping uniform only the two parameters that define the orbital plane, and the uniform

¹ Two orbits are said to be ‘homothetic’ when they are identical except for their scale, i.e. when they share the same orbital parameters, except the periapse.

eccentricity hypothesis. The agreement is much better when making either the eccentricity or the orbital plane free, but it is still better making both free.

Even with the most general situation, the parameters are still not constrained enough to decide whether the orbits are all bound or not, to extrapolate the model outside the field of view, nor even to derive reliably the direction of proper motion. However the models share a few characteristics that we judge to be robust because of their repeatability:

1. the orbital planes are close to that of the CND;
2. the orbits are not quite coplanar; the two angles that define the orbital plane vary over a $\simeq 10^\circ$ range;
3. the eccentricity varies from one orbit to another, being close to parabolic or above for the innermost orbits, and closer to circular (below $\simeq 0.5$) for the outermost.

The variations of the orbital parameters induce a particular shape for the Northern Arm (Fig. 5): for all the non-coplanar models, the Northern Arm looks like a warped surface, and this warp induces a crowding of orbits that closely follows the bright rim of the structure. That suggests that the Northern Arm is either a warped disk, or the ionized surface of a neutral cloud. The bright rim itself is not due only to the stronger UV field and a real local enhancement of the density, but also to an enhancement of the column-density due to the warp. An interesting point is that, in some models, *no* orbit follows the bright rim, which emphasizes that it is really important to consider the dynamics independently from the morphology of the Northern Arm. Another characteristic present in all the models is that the period of the orbits ranges from a few 10^4 years to a few 10^5 years, which implies that the Northern Arm would have a completely different shape in a few 10^4 years, and cannot be much older than that timescale.

Since the agreement in radial velocity is now rather good, it makes sense to look at the deviations from global motion by looking at the extended features on the residual velocity map (Fig. 5):

- A) the fbw shows a rather significant deviation in the region just southwest of the embedded star, IRS 1W; this perturbation could be due to the interaction with this star's wind;
- B) the region of this model closest to the Minicavity is perturbed;
- C) another deviation is seen at the precise location where the bright rim bends a lot, just east of IRS 7E2;
- D) finally, an elongated feature is seen on the fainter rim coming from IRS 1W towards the northeast.

4 Discussion

The presence of at least three isolated gas patches (the Western Bridge, the Northern Arm Chunk and the Bar Overlay, but also possibly the Eastern Bridge, which may or may not extend outside the field) in addition to the standard large fbws has been demonstrated. In addition to that, the Microcavity at the elbow between the Eastern Arm and the Tip is a new example of an interaction between an ISM feature and a stellar wind, similar to the Minicavity, as is the deviation from Keplerian motion detected close to IRS 1W.

In this context, it makes sense to ask what is the influence of the large number of mass losing stars present in the central parsec? These massive, hot stars of the central cluster, named "helium stars" from their strong $2.06 \mu\text{m}$ He I emission line, presumably LBV-type and WR stars, being particularly concentrated in two clusters, IRS 16 (Krabbe *et al.* 1991) and IRS 13E (Maillard *et al.* 2003), must be a major source of helium in their environment. Therefore the following question arises: what happens to this helium enriched material? Could it form or enrich the gas patches that we see? Comparing the helium and hydrogen distribution in the central parsecs, and their abundance in the different structures and in the CND is guaranteed to help us better understand the origin of the different ISM structures.

The geometry of the Northern Arm has been studied from its velocity map, leading to the conclusion that it may not be a planar structure, but rather a three-dimensional structure. Fig. 5a is quite compatible with the Northern Arm indeed being the ionized surface of a neutral cloud, which could come from the CND, in accordance with the standard formation scenario.

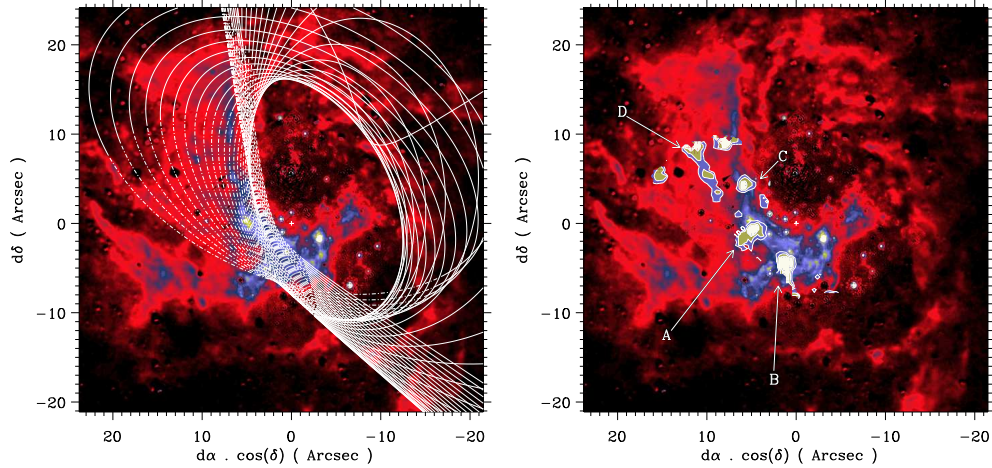


Fig. 5 On this Pa α map (Scoville *et al.* 2002), one of the Keplerian models is overplotted (left panel). This one is quite consistent with the Northern Arm and the Western Arc being related structures. On the right panel, the most significant deviations from Keplerian motion discussed in the text are labeled A to D, and indicated as filled contour.

References

- Krabbe, A., Genzel, R., Drapatz, S., & Rotaciuc, V. 1991, *ApJ*, 382, L19
 Lacy, J.H., Achtermann, J.M., & Serabyn, E. 1991, *ApJ*, 380, L71
 Lo, K.Y., & Clausen, M.J. 1983, *Nature*, 306, 647
 Maillard, J.P. 1995, In: *Tridimensional Optical Spectroscopic Methods in Astrophysics*, IAU Col. 149, G. Comte & M. Marcelin (eds), ASP Conf. Series, 71, 316
 Maillard, J.P. 2000, in *Imaging the Universe in Three Dimensions*, E. van Breughel & J. Bland-Hawthorn (eds), ASP Conf. Serie 195, 185
 Maillard, J.P., Paumard, T., Stolovy, S.R., & Rigaut, F. 2003, *these proceedings*
 Morris, M. & Maillard, J.P., 2000, in *Imaging the Universe in Three Dimensions*, E. van Breughel & J. Bland-Hawthorn (eds), ASP Conf. Serie 195, 196
 Paumard, T., Maillard, J.P., Morris, M., & Rigaut, F. 2001, *A&A*, 366, 466 (Paper I)
 Paumard, T., Maillard, J.P., Stolovy, S.R., & Rigaut, F. 2003, *these proceedings*
 Roberts, D.A. & Goss, W. M. 1993, *ApJS*, 86, 133
 Scoville, N.Z., Stolovy, S.R., Rieke, M., Christopher, M., & Yusef-Zadeh, F., 2002, submitted to *ApJ*
 Vollmer, B., & Duschl, W.J. 2000, *New Astronomy*, 4, 581
 Yusef-Zadeh, F., Roberts, D.A., & Biretta, J. 1998, *ApJ*, 499, L159
 Yusef-Zadeh, F., Stolovy, S. R., Burton, M. Wardle, M., & Ashley, M. C. B. 2001, *ApJ*, 560, 749
 Zhao, J.H. & Goss, W.M. 1988, *ApJ*, 499, L163

Annexe G

Article « *The star-forming region S106 revealed by BEAR spectro-imagery* »

